Surface Plasmon Hybridization in Novel Plasmonic Phenomena

Submitted in partial fulfillment of the requirements for the degree of

Doctor of Philosophy

in

Mechanical Engineering.

Francisco Ramirez

B.S., Mechanical Engineering, Universidad de Santiago de Chile, Chile

M.S., Mechanical Engineering, Universidad de Santiago de Chile, Chile

Carnegie Institute of Technology

Carnegie Mellon University

Pittsburgh, PA 15213

May 2017

Abstract

Surface Plasmon Hybridization in Novel Plasmonic Phenomena

by

Francisco Ramirez

Chair: Alan McGaughey

We explore the effects of surface plasmon hybridization in graphene nanostructures and silver nanoparticles as applied to novel plasmonic phenomena. The analysis is based on the theory of surface plasmon hybridization under the boundary charges method. This method, which is based in the electrostatic approximation, has been largely used to predict the resonant frequencies in strongly coupled nanoparticle clusters. Here, we extend this formalism to analyze novel plasmonic phenomena such as the blueshift of modes in graphene plasmonics, near-field radiation, thermal transport and plasmon-induced hot carrier generation in silver nanoparticles. Furthermore, we develop analytical solutions for graphene nanodisks and metallic spheres that allow for fast and accurate modeling. The analytic models provide the basis to derive a large number of results, including prediction of hybrid eigenmodes and bandstructures, far-field response, and near-field response under thermally induced fluctuations.

We predict that the strong near-field coupling in graphene nanodisk stacks can induce a blueshift in the resonant frequencies up to the near-infrared part of the spectrum. We find that the strong near-field coupling between disks can also lead to large values of radiative thermal conductance when thermally induced fluctuations are included. In this regard, an enhancement over the blackbody limit of up to two and four orders of magnitude was observed for co-planar and co-axial disk configurations. The strong coupling between co-planar disks was also explored for the development of plasmonic waveguides by considering long co-planar disk arrays. It was observed that the array posseses great potential for plasmonic waveguiding, with a strong degree of confinement for disks smaller than 200 nm. Thermal activation of the guided modes showed a thermal conductivity of up to 4.5 W/m-

K and thermal diffusivity of up to 1.4×10^{-3} m^2/s. The large values of thermal diffusivity suggest the potential of graphene disk waveguides for thermotronic interconnects.

The plasmon-induced hot carrier generation in silver nanosphere dimers was also studied. The modeling considered analytical solution for metallic nanospheres, from which the electrostatic potential of each sphere was obtained. Using these results, the hot carrier generation was explored under the basis of the Fermi golden rule. The results show a large number of hot carriers at the low frequency modes. This values exceed the number of generated hot carriers on a single sphere. The energy distribution of photogenerated electrons and holes showed a large energy gap that can be explored in photocatalysis and photovoltaic energy conversion.

Acknowledgements

First and foremost, I would like to thank my wife for her constant support and advice during this long and rough path. Neither of us really knew what was waiting for us when we decided to embark in this adventure. Back then, there was just a blurred picture of what a PhD study would meant, together with a clear idea of the many things she would leave behind for coming with me. Being the international student's wife in this country is not easy. They loose the right to work and, in exchange, receive the judgment of people that only see a housewife that stays at home and cooks. She didn't just showed people what she was capable of, but also stayed strong by my side, cheering me up with love and care, and guiding me with her amazing vision. I don't think any of this would be possible without her.

I would also like to thank my advisor, Professor Alan McGaughey, not only for accepting me in his group, but also for being such a great mentor. I learned that to succeed in the PhD, you have to feel proud and confident about the work you do. His advice and support were enough to bring those feelings back. Together with Professor Jonathan Malen, they make an amazing team promoting a nice working environment which balances team work and high quality research. I thank the opportunity of being part in such a nice community.

In relation to my thesis, I would like to thank Professor Jonathan Malen, Professor James Bain and Professor Maysam Chamanzar for agreeing to serve on my committee, and for their comments and recommendation in this work.

Special thanks to my dear friends Wee-liat Ong, Carlos Mazariegos, Minyoung Jeong, Dipanjan Saha, Anuva Kulkarni, Ramesh Shrestha, Sein Park, Cheng Shao and Iling Cheng. They were my family in Pittsburgh, always there to share the good and bad moments with nice food, beers and a cup of tea. I also want to thank my labmates Kevin Parish, Sushant Kumar, Xun Li, Nathan Nakamura, Phil Smith, Laisuo Su, Leiming Hu

and Bowen Yu. They formed a warm work community, who was always available to help, even in things not directly related with the university.

This thesis research was supported by Comisión Nacional de Investigación Científica y Tecnológica (CONICYT), Becas de Doctorado en el Extranjero BECAS CHILE.

Contents

List of Figures

List of Tables

Introduction

1.1 Motivation

From the construction of mirrors and microscopes to the design of efficient photovoltaic devices, light control has always been in the mind of scientists from a great number of disciplines. The reason is simple: light is everywhere, it is the fastest media of energy transport, and its interaction with matter is fundamental for phenomena including energy conversion [1], imaging [2], and photochemistry [3]. The increased interest in miniaturization has also raised the need for light control at the nanoscale, where plasmonics, the surface electromagnetic waves formed by the coupling of photons and the electron plasma, have become the most promising alternative to reach this goal [4]. The advantage of plasmonics among other techniques for nanoscale light manipulation hinges on the ability of surface plasmons to confine light bellow the diffraction limit, giving rise to a large density of photons at a surface, and therefore increasing the chances for light-matter interactions.

For decades, noble metals like silver and gold have been the primary choice for plasmonics applications, given their low electron scattering rates and their ability to interact with light in the visible part of the spectrum. The great level of expectation from plasmonics led to the development of breakthrough applications like plasmonic interconnects [5], plasmonic photovoltaics [1], and biotherapy [6]. However, the progress in the field has been hindered by the intrinsic electron-scattering losses and degradation in noble metals. The rise of the field of near-field thermal radiation, where strong thermal radiation beyond the Planck blackbody limit can be achieved in materials supporting surface electromagnetic waves, imposed another limitation for noble metals, as proper materials require strong

interaction with light below the near-infrared spectrum and high melting temperatures [7].

The field of plasmonics is now evolving to overcome the limitations of traditional noble metals, either by the search for alternative materials or by optimizing the intrinsic decay mechanisms. One example is the emergence of graphene, which has successfully been proved to support strongly confined and long propagating surface plasmons in the terahertz and mid-infrared range, opening new venues for the development of plasmonic interconnects and near-field thermal radiation, among other applications. Another example is the study of plasmon-induced hot electrons and holes in noble-metal nanoparticles for photocatalysis [3], phototection [8] and photovoltaics [9]. Together with the evolution of the field, new challenges have risen to describe the physics of the phenomena properly. Thus, a revisit and upgrade of existing theories in plasmonics is necessary.

1.2 Objective

Plasmonic responses can be strongly manipulated by reducing the size of the material. Unlike the interaction of light with the electron plasma in an extended surface, electrons oscillations in small metallic geometries can strongly interact with far-field light, giving rise to localized surface plasmons (LSPs) [10]. The electromagnetic response of LSPs is conditioned by the structure's size, shape and the properties of the surrounding media. The LSP properties can be also affected by the near-field coupling with other nanostrutures. This process is known as plasmon hybridization, in analogy to the hybridization of orbitals in molecules. Plasmon hybridization has proved to lead to interesting phenomena like non-symmetric resonances [11], tuning of radiative properties [12] and waveguiding [13].

The objective of this work is to understand the mechanisms underlying plasmonic coupling and hybridization in small structures and then apply this knowledge to novel plasmonic phenomena, such as graphene plasmonics and plasmon-induced hot carrier generation. We

will apply the method of surface charge under the electrostaic approximation to derive appropriate models and explore (i) extreme blueshifting of localize surface plasmon in graphene nanodisks stacks, (ii) near-field radiation in graphene nanodisk dimers, (iii) plasmonic thermal transport in graphene nanodisk arrays, and (iv) plasmon-induced hot carrier generation in metallic nanosphere dimers.

1.2.1 Extreme Blueshift of Localized Surface Plasmons in Graphene Nanodisk Stacks

Graphene holds great potential for surface plasmons with comparatively larger energy confinement and decay length than noble metals. The reasons are rooted into its extraordinary high electron mobility and electrical tunability of its carrier concentration, which show potential for tightly confined and long propagating surface plasmon modes, with tunable spectrum ranging from the terahertz to the mid-infrared [14]. In order to fully compete with noble metals, the free electron concentrations in graphene needs to be large enough to achieve surface plasmons at the visible range of the spectrum. However, the largest electrons concentration in graphene achieved experimentally show plasmon resonances only up to the mid-IR [15]. Among the different techniques that have been explored to push the spectrum of GSP up to higher frequencies [15, 16**?**], surface plasmon hybridization holds great potential. The 2D structure of graphene allows strong coupling between parallel graphene nanostructures and a large blue-shifting of the resonant frequencies of the so-called bright modes [17, 18].

We will investigate plasmonic hybridization in graphene nanodisk stacks for blueshifting of the fundamental bright mode. We will identify the key mechanisms responsible for this phenomenon together with the limits for extreme blueshifting of graphene surface plasmons.

1.2.2 Near-field Radiation Heat Transfer in Graphene Disk Dimers

Thermal radiation between two bodies separated by a distance smaller than the dominant thermal wavelength at the temperatures of the objects can exceed the Planck blackbody limit [19]. The enhancement over the blackbody limit is due the tunneling of evanescent electromagnetic waves at the surface of the bodies. This enhancement can be several orders of magnitude in materials that support surface plasmons or surface phonon-polaritons, providing that their activation energies are comparable to the thermal energy at the emitter's temperature. Because graphene surface plasmons can be activated at terahertz frequencies, this material has been proposed for strong near-field radiation enhancement[20]. Besides intensive work on extended graphene surfaces[20][21], the near-field thermal radiation properties of nanostructured graphene are largely unexplored.

We will study the near-field thermal radiation properties of surface plasmons in graphene nanodisks dimers. We will develop an analytical tool to achieve fast modeling of near-field thermal radiation in disk dimers. This model will be used to explore the effects of plasmon hybridization on near-field enhancement in different configurations.

1.2.3 Plasmonic Thermal Transport in Graphene Disk Arrays

The coherent and narrow band emission properties at the near-field has shown potential for the development of solid-state thermal devices. In this field, named as photon thermotronics [22], great number of devices have been proposed like thermal transistors, rectifiers and heat spliters.

We will study the thermal activation of surface plasmon modes in graphene nanodisk waveguides for applications as thermotronic interconnects. In this case, hybridization takes place by the formation of dispersion bands representing the propagation of single disk modes that are hopping from disk to disk. First, we will describe the waveguiding

properties of surface plasmons in a graphene disk array by calculating the plasmonic band structure. Then we will obtain the thermal properties of the array based on the dispersion bands of the modes.

1.2.4 Plasmon-induced Hot Carrier Generation in Nanoparticle Dimers

Localized surface plasmons in metal nanoparticles have long been regarded for their ability to capture far-field radiation, generating strong and localized electromagnetic energy at the surface of the particle that can be used in applications like light trapping and local heating.

In the transient process between light absorption to local heating, however, a series of processes occurs. After light absorption by LSP resonance, the energy can be dissipated radiatively via re-emission of photons or non-radiatively through excitation of hot carriers, which possess energies larger than the equilibrium distribution. In a normal situation, hot-carriers eventually relax via electron-electron and electron-phonon scattering, leading to Joule heating. By inducing intermediate processes before relaxation occurs, however, hot-carriers can be extracted and used in photochemistry [23], photodetection [8] or photovoltaics [9].

Although experimentally demonstrated, the physics underlying this phenomenon is not well understood, especially regarding light absorption in nanoparticle clusters. We will study the influence of surface plasmon hybridization in silver nanoparticles dimers on the generation of hot carriers. We will use the method of surface charges to model the electrostatic field distribution. These results will then be used to predict the distribution of hot electrons using the free-electron model.

1.3 Methods

We consider nanoparticles that are smaller than the wavelength of the surroundings. In this regime, the temporal dependence of the electromagnetic field can be ignored and the problem is solved using electrostatics. The electrostatic approximation allows faster calculation as the number of governing equations to be solved is reduced. Additionally, given the large number of analytical solutions for electrostatic problems in the literature [24], simple models can be derived.

Under the electrostatic approximation, the plasmonic coupling between nanoparticles can be well described using the boundary charge method (BCM). The method consist in expressing the electrostatic response of a nanoparticle by an equivalent surface charge density, which is expressed in terms of a bi-orthonormal basis. We apply the BCM in all our calculations, using an appropriate basis to the specific geometry of the particle. This results in analytic solutions for spheres and disk geometries, that are used to predict the spectral response under plane wave illumination, near-field thermal radiation, plasmonic bandstructure.

1.4 Overview and Scope

In Chapter 2, the theoretical framework is described. The chapter is divided in three sections. The first section includes a brief description of the main concepts from electrodynamics. In the second section, the fundamentals of surface plasmons are explained, together with a description of the optical properties of the materials considered in this work. In the last section, the theory of surface plasmon hybridization is described, including a derivation of the models for two and three dimensional nanostructures.

Chapter 3 describes to the study of the effects of surface plasmon hybridization on

the blueshift of the resonant frequencies in graphene nanodisk stacks. Using analytical solutions for the far field response of stacked disks, a systematic analysis of surface plasmon hybridization in graphene disk stacks is performed. In the second part, the limits of the plasmonic frequency blushift achieved by this method are explored.

Chapter 4 focuses on the analysis of near-field thermal radiation between two graphene nanodisks. Here, analytical solution for the near-field thermal radiation between two disks are used to explore the dependence of the near-field thermal conductance on separation, orientation, disk diameter, electron mobility, and Fermi level. Given the accuracy and fast computation achieved from the analytical solution, the thermal radiation is explored in a large range of scenarios.

Chapter 5 consists of a study of the thermal transport properties of guided plasmonic modes in one dimensional graphene disk arrays. In the first section, the plasmonic band-structure and propagation properties are studied, including an analysis of the effects of radiation damping. In the second section, the thermal transport properties are studied, where the thermal conductivity, heat capacity, and thermal diffusivity are predicted for a large number of scenarios.

Chapter 6 corresponds to the study of hot carrier generation in silver nanosphere dimers. An analytical solution for the planewave response of nanosphere cluster is developed. The first part consists of the validation of the electromagnetic response predicted from the analytical solution. The second part corresponds in the calculation of hot carrier generation in a single nanosphere and a dimer, considering three values of relaxation time of hot carriers.

In Chapter 7 the major contributions of this work are presented and suggestions for future study are discussed.

Theory and Methods

This chapter describes the background and methods regarding basic theories and modeling techniques. As the study of plasmons is related to electromagnetic phenomena, we begin by describing the general concepts of the Maxwell equations, which are the governing equation of electrodynamics, together with a brief introduction of reflection and transmission of planar surfaces, the dyadic Green's function, and the fluctuation-dissipation theorem, which is the fundamental theory for study of radiative heat transfer. In the second part, we introduce the fundamentals of surface plasmons, including a description of the optical properties of plasmonic materials. In the last section, the theory of surface plasmon hybridization is introduced, where the specific methods for 3D and 2D nanostructures are described. This last section contains the essential models used in this work.

2.1 Introduction to Classical Electrodynamics

2.1.1 Maxwell Equations and Constitutive Relations

In macroscopic electrodynamics, the singular character of charges and their associated currents is avoided by considering volumetric charge density ρ_{3D} and current density $\boldsymbol{J}$. In this work, we label the volumetric charge density as ρ_{3D}, in order to distinguish it from the surface charge density, ρ. In differential form and in SI units the macroscopic Maxwell's

equations have the form [25]:

$$\nabla \times \boldsymbol{E}(\boldsymbol{r},t) = -\frac{\partial \boldsymbol{B}(r,t)}{\partial t}, \tag{2.1a}$$

$$\nabla \times \boldsymbol{H}(\boldsymbol{r},t) = \frac{\partial \boldsymbol{D}(\boldsymbol{r},t)}{\partial t} + \boldsymbol{J}(r,t) \tag{2.1b}$$

$$\nabla \cdot \boldsymbol{D}(\boldsymbol{r},t) = \rho_{3D}(\boldsymbol{r},t) \tag{2.1c}$$

$$\nabla \cdot \boldsymbol{B}(\boldsymbol{r},t) = 0, \tag{2.1d}$$

where $\boldsymbol{E}$ denotes the electric field, $\boldsymbol{D}$ the electric displacement, $\boldsymbol{H}$ the magnetic field, $\boldsymbol{B}$ the magnetic induction. Maxwell equations combine and complete the laws formerly established by Faraday, Ampere, Gauss, Poisson, and others. The components of these vector and scalar fields constitute a set of 16 unknowns. Depending on the considered medium, the number of unknowns can be reduced considerably. A complete solution of Maxwell equations must consider an appropriate set of boundary conditions at the interface between two media 1 and 2, which are given by:

$$\hat{n} \times (\boldsymbol{E}_1 - \boldsymbol{E}_2) = 0 \tag{2.2a}$$

$$\hat{n} \times (\boldsymbol{H}_1 - \boldsymbol{H}_2) = \boldsymbol{\kappa} \tag{2.2b}$$

$$\hat{n} \cdot (\boldsymbol{D}_1 - \boldsymbol{D}_2) = \rho \tag{2.2c}$$

$$\hat{n} \cdot (\boldsymbol{B}_1 - \boldsymbol{B}_2) = 0, \tag{2.2d}$$

where $\boldsymbol{\kappa}$ and ρ are the surface conductivity and surface charge. Eqns. (2.2a) and (2.2b) represent the boundary conditions for the tangential components and Eqns. (2.2c) and (2.2d) the normal components.

In most practical situations, there are no sources in the individual domains, so that and $\boldsymbol{\kappa}$ and ρ consequently vanish. The four boundary conditions are not independent of

each other since the fields on both sides of the interface are linked by Maxwell equations.

$\boldsymbol{J}$, $\boldsymbol{D}$, and $\boldsymbol{B}$ can be related to the electric field $\boldsymbol{E}$ and the magnetic field $\boldsymbol{H}$ through constitutive relations. Though non-linear in their most complete form, constitutive relations can be treated in a linear form, whenever the field strengths are small enough [26]. Accordingly, the frequency domain and non-local electric displacement $\boldsymbol{D}$, magnetic induction $\boldsymbol{B}$, and the current density $\boldsymbol{J}$, are given by:

$$\begin{aligned}
\boldsymbol{D}(\boldsymbol{k},\omega) &= \varepsilon_0 \bar{\boldsymbol{\varepsilon}}(\boldsymbol{k},\omega)\cdot\boldsymbol{E}(\boldsymbol{k},\omega)\\
\boldsymbol{B}(\boldsymbol{k},\omega) &= \mu_0 \bar{\boldsymbol{\mu}}(\boldsymbol{k},\omega)\cdot\boldsymbol{H}(\boldsymbol{k},\omega)\\
\boldsymbol{J}(\boldsymbol{k},\omega) &= \bar{\boldsymbol{\sigma}}(\boldsymbol{k},\omega)\cdot\boldsymbol{E}(\boldsymbol{k},\omega),
\end{aligned}$$

where $\boldsymbol{k}$ and ω are the wavevector and the angular frequency, respectively.

In general, it is difficult to account for spatial dispersion in field calculations. However, in most cases of interest the effect is very weak and the k dependence, which is associated with non-local effects, can be ignored [25]. Temporal dispersion, on the other hand, is a widely encountered phenomenon and it is important to take it accurately into account.

A final constitutive equation for $\rho_{3D}(k,\omega)$ is established by the charge conservation equation, which is implicitly contained in Maxwell's equations:

$$\nabla\cdot\boldsymbol{J}(\boldsymbol{r},t)+\frac{\partial\rho_{3D}(\boldsymbol{r},t)}{\partial t}=0. \tag{2.4}$$

By applying a Fourier transform, we find the following relation between the charge density and the electric field:

$$\rho_{3D}(\boldsymbol{k},\omega)=\frac{1}{i\omega}\boldsymbol{k}\cdot\left[\bar{\boldsymbol{\sigma}}(\boldsymbol{k},\omega)\cdot\boldsymbol{E}(\boldsymbol{k},\omega)\right].$$

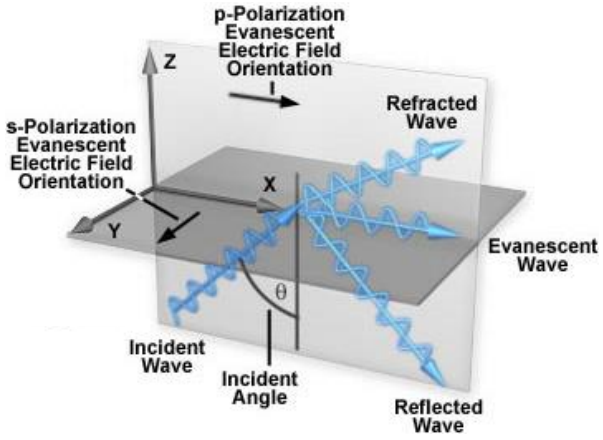

Figure 2.1: Schematic diagram of a plane wave incident at the interface between two media [27]. The plane formed between the wave vector of the incoming wave and the vector normal to the surface is called the plane of incidence. The polarization of the electromagnetic wave can be classified by separating the electric field waves traveling parallel to the plane of incidence (p-polarization), form those perpendicular to the plane of incidence (s-polarization). Additionally evanescent waves are formed at the interface between the two media.

2.1.2 Reflection and Transmission of Electromagnetic Waves

Consider a plane wave traveling through a medium 1 that is incident on the interface between media 1 and 2 (Fig. 2.1). Under this situation, due to the impedance mismatch between the media, some portion of the wave will be transmitted through media 2, while the rest will be reflected back into media 1. The electric and magnetic fields at each media should satisfy the boundary conditions given by Eqns. (2.2a)–(2.2d):

$$\hat{n} \times (\boldsymbol{E_i}|_{z=0} + \boldsymbol{E_r}|_{z=0} - \boldsymbol{E_t}|_{z=0}) = 0 \tag{2.5a}$$

$$\hat{n} \times (\mu_0\mu_1\boldsymbol{H_i}|_{z=0} + \mu_0\mu_1\boldsymbol{H_r}|_{z=0} - \mu_0\mu_2\boldsymbol{H_t}|_{z=0}) = 0, \tag{2.5b}$$

where $\hat{n}$ is the unit vector normal to the surface of the interface. Here, we assume that the media are isotropic, local, and temporally dispersive. Thus, only two boundary conditions

are needed and the solution of the Maxwell Equations on each medium is given by plane waves.

An arbitrarily polarized plane wave $E_1 \exp(\boldsymbol{k}_1 \cdot \boldsymbol{r} - i\omega t)$ can always be written as the superposition of two orthogonally polarized plane waves. It is convenient to choose these polarizations parallel and perpendicular to the plane of incidence defined by the k-vector of the plane wave and the surface normal $\hat{n}$ of the plane interface (Fig. 2.1):

$$E_1 = E_1^{(s)} + E_1^{(p)},$$

where $E_1^{(s)}$ is parallel to the interface and $E_1^{(p)}$ is perpendicular to the wavevector k and $E_1^{(s)}$. Upon reflection or transmission at the interface, the polarizations (s) and (p) are conserved.

The procedure to solve Eqns. (2.5a) and (2.5b) can be found in a number of introductory textbooks of electrodynamics [28]. For simplicity, here we only provide the solution.

A direct consequence of the plane wave solution and the boundary conditions from Eqns. (2.5a) and (2.5b) is that the components of the wavevectors parallel to the interface, $k_{\parallel}$, are conserved which gives rise to Snell's law. On the other hand, the components of the wavevector perpendicular to the interface, k_z, are given by:

$$k_{z_1} = \sqrt{k_1^2 - k_{\parallel}^2} \tag{2.6a}$$

$$k_{z_2} = \sqrt{k_2^2 - k_{\parallel}^2}. \tag{2.6b}$$

Thus, the solution of Eqns. (2.5a) and (2.5b) is given by the ratio between the transmitted and reflected electric field and the incident field, also known as Fresnel coefficients.

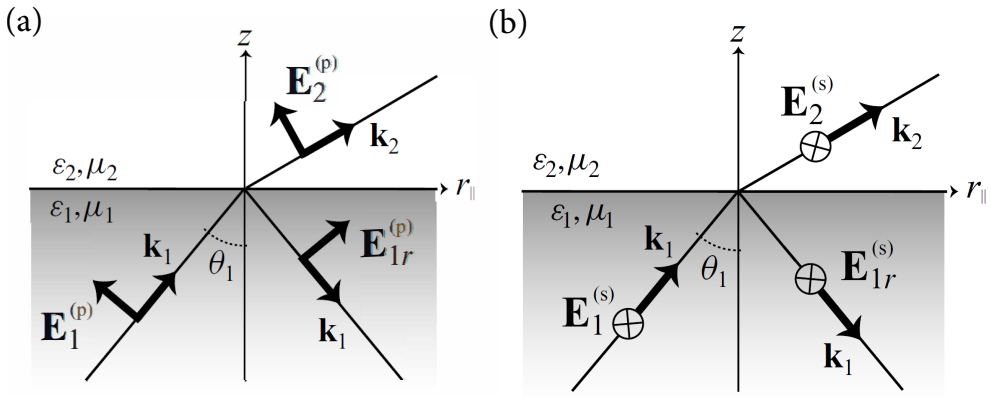

Figure 2.2: Schematic of incident, reflected and transmitted electromagnetic waves for (a) a p-polarized wave and (b) a s-polarized wave [25].

For a p-polarized wave [Fig. 2.2(a)] the Fresnel coefficients are given by:

$$r^{(p)} = \frac{E_r^{(p)}}{E_i^{(p)}} = \frac{\varepsilon_2 k_{z_1} - \varepsilon_1 k_{z_2}}{\varepsilon_2 k_{z_1} + \varepsilon_1 k_{z_2}} \tag{2.7a}$$

$$t^{(p)} = \frac{E_t^{(p)}}{E_i^{(p)}} = \frac{2\varepsilon_2 k_{z_1}}{\varepsilon_2 k_{z_1} + \varepsilon_1 k_{z_2}} \sqrt{\frac{\mu_2 \varepsilon_1}{\mu_1 \varepsilon_2}}, \tag{2.7b}$$

where $r^{(p)}$ and $t^{(p)}$ are Fresnel coefficients for the reflected and transmitted wave.

Similarly for an s-polarized wave [Fig. 2.2(b)], we get:

$$r^{(s)} = \frac{E_r^{(s)}}{E_i^{(s)}} = \frac{\mu_2 k_{z_1} - \mu_1 k_{z_2}}{\mu_2 k_{z_1} + \mu_1 k_{z_2}} \tag{2.8a}$$

$$t^{(s)} = \frac{E_t^{(s)}}{E_i^{(s)}} = \frac{2\mu_2 k_{z_1}}{\mu_2 k_{z_1} + \mu_1 k_{z_2}}. \tag{2.8b}$$

2.1.3 Dyadic Green's Functions

An important concept in field theory is the Green's functions: the fields due to a point source. In electromagnetic theory, the dyadic Green's function $\bar{\boldsymbol{G}}$ is essentially defined by the field $\boldsymbol{E}$ at the field point r generated by a current (Fig. 2.3). From the Maxwell

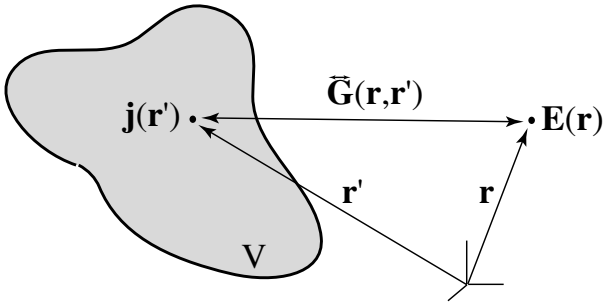

Figure 2.3: Illustration of the dyadic Green's function [25]. The Green's function renders the electric field at the field point r due to a single point source $\boldsymbol{J}(r)$ at the source point r'. Since the field at r depends on the orientation of $\boldsymbol{J}$, the Green's function must account for all possible orientations in the form of a tensor.

equations it follows that the electric and magnetic fields obey the equations:

$$\nabla \times \nabla \times \boldsymbol{E} - k^2 \boldsymbol{E} = i\omega\mu \boldsymbol{J}(\boldsymbol{r}) \tag{2.9a}$$

$$\nabla \times \nabla \times \boldsymbol{H} - k^2 \boldsymbol{H} = \nabla \times \boldsymbol{J}(\boldsymbol{r}). \tag{2.9b}$$

Then we need a dyadic Green's function that satisfies the equation:

$$\nabla \times \nabla \times \bar{\boldsymbol{G}}(\boldsymbol{r}, \boldsymbol{r}') - k^2 \bar{\boldsymbol{G}}(\boldsymbol{r}, \boldsymbol{r}') = \bar{\boldsymbol{I}} \delta(\boldsymbol{r} - \boldsymbol{r}'), \tag{2.10}$$

where $\bar{\boldsymbol{I}}$ is a unitary matrix.

The solution is given by the dyadic Green's Function [25]:

$$\bar{\boldsymbol{G}}(\boldsymbol{r}, \boldsymbol{r}') = \left(\overleftrightarrow{I} + \frac{1}{k^2} \nabla\nabla\cdot \right) \bar{\boldsymbol{I}} G_0(\boldsymbol{r}, \boldsymbol{r}'), \tag{2.11}$$

where $G_0(r, r')$ is the scalar Green's function given by [25]:

$$G_0(\boldsymbol{r}, \boldsymbol{r}') = \frac{e^{\pm ik|\boldsymbol{r}-\boldsymbol{r}'|}}{4\pi|\boldsymbol{r} - \boldsymbol{r}'|}, \tag{2.12}$$

Thus, the general solution for the electric and magnetic fields are:

$$\boldsymbol{E}(r) = \boldsymbol{E}_0 + i\omega\mu_0\mu \int_V \bar{\boldsymbol{G}}(\boldsymbol{r}, \boldsymbol{r}') \cdot \boldsymbol{J}(\boldsymbol{r}')dV' \tag{2.13a}$$

$$\boldsymbol{H}(r) = \boldsymbol{H}_0 + \int_V \left[\nabla \times \bar{\boldsymbol{G}}(\boldsymbol{r}, \boldsymbol{r}')\right] \cdot \boldsymbol{J}(\boldsymbol{r}')dV', \tag{2.13b}$$

where we consider the fact that the solution given by the dyadic Green's function is a particular solution to the non-homogeneous Helmholtz equations and so we need to include a solution to the homogeneous equation $\boldsymbol{E}_0$ and $\boldsymbol{H}_0$ to complete the general solution.

Is important to mention that the volume integral equations are valid in the space outside the source volume V in order to avoid the singularity of $\bar{\boldsymbol{G}}$ at $r = r'$.

2.1.4 Theory of Thermal Radiation by Fluctuating Sources

The Planck's law for blackbody radiation is a valid approximation for predicting the radiative energy emitted by an object at large distances. However, this expression strongly differs from the true behavior in the near-field regime, *i.e*, at distances smaller than half of the wavelength of the emitted electromagnetic radiation. This is because Planck's law ignores the contribution from the evanescent fields whose contribution becomes dominant in the near-field [19].

A complete picture of thermal radiation must therefore consider the complete nature of the electromagnetic fields emitted by the fluctuating current and charges in the material. In cases where the system is close to equilibrium, fluctuations can be described by linear response theory, where the fluctuation-dissipation theorem remains the most important theory [29].

The fluctuation-dissipation theorem states that the dissipation in a non-equilibrium system is related to the spontaneous fluctuations occurring at different times in the equi-

librium system [25]. Among the different expressions that can be derived for this theorem, the most relevant for matters of this research is the spectral correlation between fluctuating currents $\boldsymbol{J}$ and the dissipation of the material, which is given by:

$$\langle \boldsymbol{J}^*(\boldsymbol{r},\omega)\boldsymbol{J}(\boldsymbol{r}',\omega)\rangle = \frac{\omega\varepsilon_0}{\pi} Im\left[\varepsilon(\omega)\right]\theta(\omega,T)\delta(\boldsymbol{r}-\boldsymbol{r}'), \tag{2.14}$$

where $\theta(\omega,T) = \frac{\hbar\omega}{1-\exp\left(-\frac{\hbar\omega}{k_B T}\right)}$ is the mean energy of the quantum oscillator and $\varepsilon(\omega)$ is the dielectric constant of the material.

Eqn. (2.14) is the starting point of many expressions pertaining the study of fluctuating electrondynamics [19]. For instance, the power emitted by an object, which is given by the power dissipated by the induced electric field $P = \int \boldsymbol{J}^* \cdot \boldsymbol{E} dV$, can be obtained by combining Eqn. (2.13a) and Eqn. (2.14). After some algebraic manipulations, the emissive power of an object is given by [25]:

$$P = \frac{k^2}{2\pi} Im\left[\varepsilon(\omega)\right]\theta(\omega,T) Tr\left\{ \int_V Im\left[\bar{\boldsymbol{G}}(\boldsymbol{r},\boldsymbol{r})\right] dV \right\}. \tag{2.15}$$

The above expression highlights the importance of the dyadic Green's function in the estimation of radiative heat transfer in the near field. The form of the dyadic Green's function is strictly dependent on the geometries and boundary conditions of the problem, and only a few analytic solutions have been derived for infinite surfaces [30] and spheres [31]. For more complex geometries, numerical methods, such as the boundary element methods are normally used [32]. The method rely in the expansion of fictitious surface currents, whose dyadic Green's function is given by the dipole model [33].

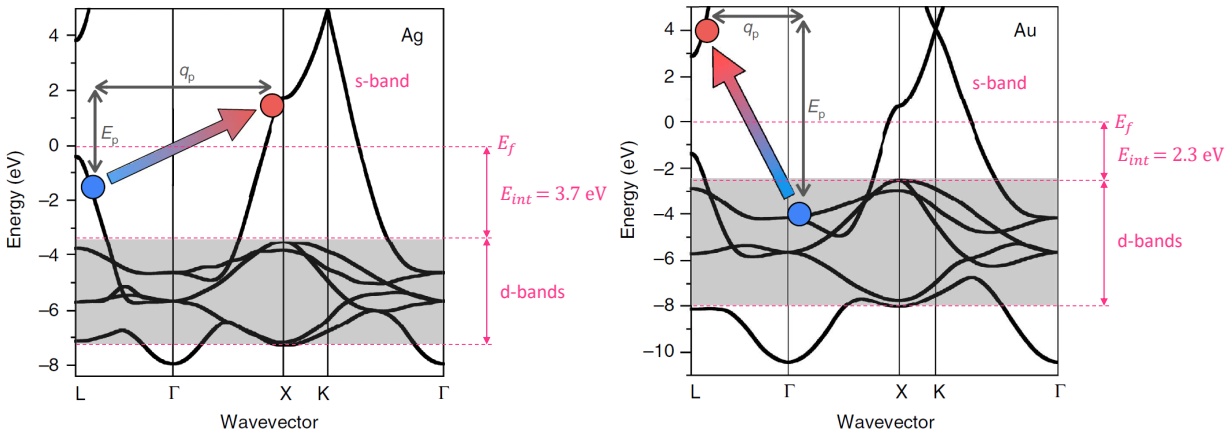

Figure 2.4: Electronic bandstructure of silver (Ag) and gold (Au), indicating a generalize transition induced by energy, E_p and momentum, q_p. The difference, E_{int}, between the Fermi level and the highest energy of the d-bands represents the minimum energy required for interband transitions [34].

2.2 Fundamentals of Surface Plasmons

2.2.1 Optical Properties of Plasmonic Materials

2.2.1.1 Metals

The optical properties of metals can be explained by the plasma model, which considers a free electron gas moving against a fixed background of positive ion cores. In this model, the details of the atomic lattice and electron-electron interactions are ignored. Instead, a characteristic collision frequency, γ, is used to represent the damped motion of the electron gas. Thus, from the equations of motion for the electron gas under an external electromagnetic field [10], the following model is derived:

$$\varepsilon_m = \varepsilon_\infty - \frac{\omega_p^2}{\omega\left(\omega + i\gamma\right)}, \tag{2.16}$$

where ω_p is the electron plasma frequency, which is proportional to the electron charge density inside the metal, and ε_∞ is a constant representing the residual polarization due to the positive background of ion cores.

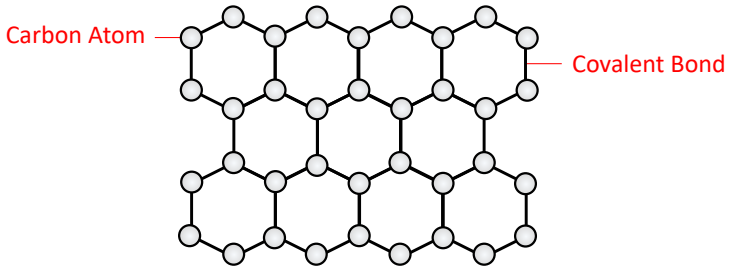

Figure 2.5: Crystal structure of graphene.

While for alkali metals Eqn. (2.16) is a fair model for frequencies up to the ultraviolet, for noble metals the validity is limited by the existence of interband transitions in the visible range [10]. In the case of silver, interband transitions from electrons at the d-bands occur for photon energies larger than 3.7 eV (Fig. 2.4), and Eqn. (2.16) remains valid in the visible spectrum ($\varepsilon_\infty = 4.18$, $\gamma = 60$ meV and $\omega_p = 9.07$ eV). For gold, interband transisions occurs for photons in the visible spectrum (photon energies above 2.3 eV), and the optical properties have to be extracted from measurements [35].

2.2.1.2 Graphene

Graphene is a two dimensional carbon allotrope. Its crystal structure is formed by covanlently bonded carbon atoms forming a honeycomb structure (Fig. 2.5). The interaction between low energy electrons and the lattice is described by the Dirac equation [36]. This gives rise to an electronic dispersion defined by energy bands of cosine shape and conical sections near the edges of the Brillouin zone (Fig. 2.6). At the conical sections, electrons behave as relativistic Dirac fermions with an effective speed, v_f of 10^6 m/s and room temperature mobility, μ, exceeding $15,000$ cm^2/Vs [36].

Intrinsic graphene behaves as a semi-metal with the Fermi level of electrons located at the contact point between the two conical bands, which is known the Dirac point. Injection of charge carriers trough electrical gating or chemical doping moves the Fermi level, E_f, to a new energy defined by, $E_f \approx \hbar v_f \sqrt{\pi n_e}$, where n_e is the concentration of additional

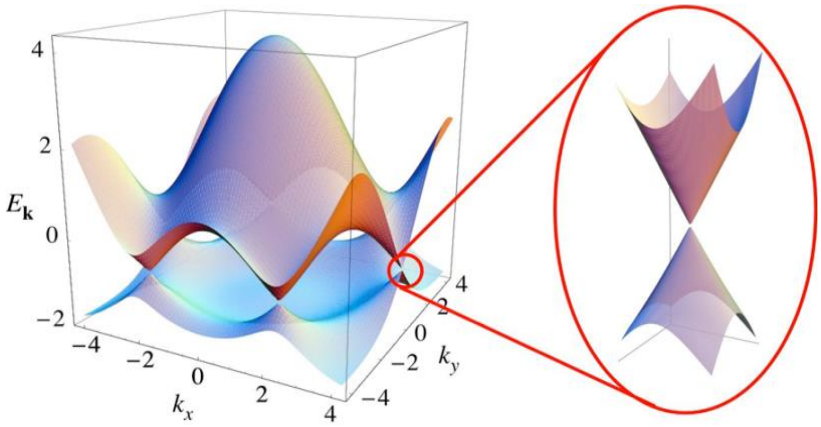

Figure 2.6: Electronic bandstructure of graphene [37].

charge carriers [15]. Thus, injection of charge carriers changes the electronic properties of graphene from semi-metal to metal (Fig. 2.7). Fermi levels up to 1 eV have been realized by electrical gating [15].

The optical response of intrinsic graphene is determined by the direct excitation of electrons by photons, as shown in Fig. 2.8(a), giving rise to the well known 2.3% absorption for monolayer graphene [38]. Injection of charge carriers opens an optical gap of size $2E_f$ for direct excitations. In this case, photons with energies larger than $2E_f$ are absorbed due to the interband transition of electrons, while lower energetic photons induce intraband transitions, as shown in Fig. 2.8(b).

Mathematically, the optical response of graphene is represented by the two-dimensional optical conductivity, σ. In the local limit, the optical conductivity of graphene is given by [39]

$$\sigma(\omega) = \frac{2e^2 k_{\mathrm{B}} T}{\pi\hbar^2} \frac{i}{\omega + i\tau^{-1}} \ln\left[2\cosh\left(E_f/2k_{\mathrm{B}}T\right)\right] + \frac{e^2}{4\hbar}\left[H(\omega/2) + \frac{4i\omega}{\pi}\int_0^\infty \frac{H(x) - H(\omega/2)}{\omega^2 - 4x^2} dx\right], \tag{2.17}$$

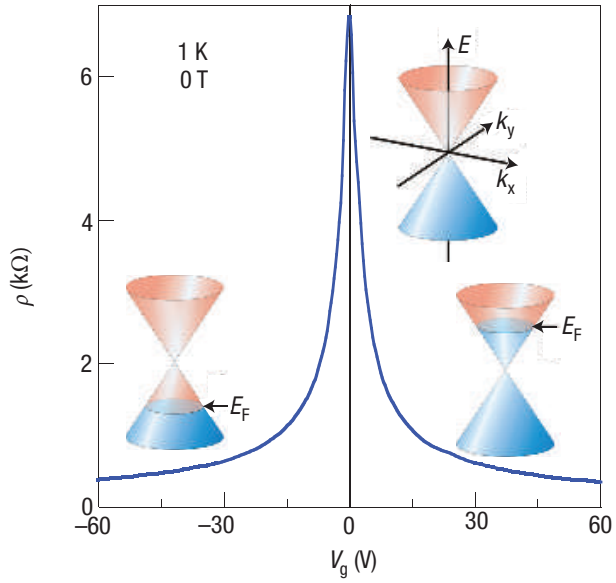

Figure 2.7: Electrical resistivity of single-layer graphene as a function of the voltage bias [36].

where

$$H(x) = \frac{\sinh(\hbar x/k_{\mathrm{B}}T)}{\cosh(E_f/k_{\mathrm{B}}T) + \cosh(\hbar x/k_{\mathrm{B}}T)}.$$

Here, e is the electron elementary charge, k_{B} is the Boltzmann constant, T is the temperature, $\hbar$ is the reduced Planck constant, ω is the angular frequency, and τ is the impurity-limited lifetime [15]. The first term on the right-hand side corresponds to the contribution from intraband transitions and the second term corresponds to the contribution from interband transitions.

Optical losses associated with intraband trasitions are given by $\tau = \mu E_f/ev_f^2$ [15]. Unless noted, we consider a mobility of 10,000 cm^2/V·s, which is a conservative value compared with the largest mobilities observed in high-quality suspended graphene [36].

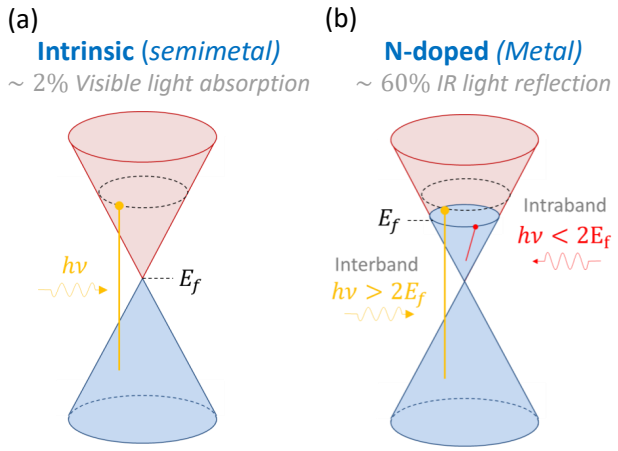

Figure 2.8: Electronic transitions induced by photons in (a) intrinsic graphene and (b) doped graphene

At low temperatures ($E_f/k_BT \gg 1$), Eqn. (2.17) reduces to

$$\sigma(\omega) = \frac{2e^2E_f}{\pi\hbar^2}\frac{i}{\omega + i\tau^{-1}} + \frac{e^2}{4\hbar}\left[\Theta(\hbar\omega - 2E_f) + \frac{i}{\pi}\ln\left|\frac{\hbar\omega - 2E_f}{\hbar\omega + 2E_f}\right|\right], \tag{2.18}$$

where Θ is the step function.

2.2.2 General Theory of Surface Electromagnetic Waves

Consider the Fresnel coefficients for a p-polarized wave [Eqns. (2.7a) and (2.7b)]

$$r^{(p)} = \frac{\varepsilon_2 k_{z_1} - \varepsilon_1 k_{z_2}}{\varepsilon_2 k_{z_1} + \varepsilon_1 k_{z_2}}$$
$$t^{(p)} = \frac{\varepsilon_2 k_{z_1}}{\varepsilon_2 k_{z_1} + \varepsilon_1 k_{z_2}}\sqrt{\frac{\varepsilon_1}{\varepsilon_2}},$$

where we consider that both media are non-magnetic, *i.e.* $\mu_1 = \mu_2 = 1$.

A pole in the Fresnel coefficients ($\varepsilon_2 k_{z_1} + \varepsilon_1 k_{z_2} = 0$) is given when the following relation

is satisfied:

$$\frac{k_{z_2}}{k_{z_1}} = -\frac{\varepsilon_2}{\varepsilon_1}. \tag{2.19}$$

In order to find a real solution for Eqn. (2.19), $\varepsilon_1\varepsilon_2 < 0$. In our case, we consider an electromagnetic wave traveling in medium 1 with $\varepsilon_1 > 0$, incident into a medium 2 with $\varepsilon_2 < 0$. As we will review later, negative permittivity can be found in materials sustaining polarization oscillations, like charge density waves or plasmons in metals, or optical phonons in polar dielectrics.

As we can intuitively predict from the Fresnel coefficients, cases where Eqn. (2.19) is satisfied imply that the intensity of the reflected (E_r) and transmitted (E_t) electric field at the interface would become orders of magnitude larger than the magnitude of the incident electric field E_i. In other words, there is an enhancement of the electric field intensity at the interface. We will further study the implication of this condition by analyzing the components of the wave vector.

From Snell's law, we know that the components of the wave vector parallel to the interface are equal ($k_{\|_1} = k_{\|_2} = k_p$), thus the normal components of the wavevectors are given by:

$$k_{z_1}^2 = \varepsilon_1 k_0^2 - k_p^2 \tag{2.20a}$$

$$k_{z_2}^2 = \varepsilon_2 k_0^2 - k_p^2, \tag{2.20b}$$

where we use the relation $k^2 = k_\|^2 + k_z^2$, the dispersion relation in each medium $k_1^2 = \varepsilon_1 k_0$, $k_1^2 = \varepsilon_2 k_0$, and $k_0 = \frac{\omega}{c_0}$ is the wavevector in the free space.

Combining Eqns. (2.19), (2.20a) and (2.20b), we get the following expression for the

parallel component of the wave vector k_p:

$$k_p = k_0 \sqrt{-\frac{\varepsilon_1 \varepsilon_2}{\varepsilon_1 + \varepsilon_2}}. \tag{2.21}$$

It can be demonstrated that, in the cases where $|\varepsilon_2| > \varepsilon_1$, the parallel component of the wavevector satisfies the relations $k_p > k_1$ and $k_p > k_2$. According to Eqns. (2.20a) and (2.20a), this condition means that the normal components of the wavevector become imaginary. The reflected and transmitted electromagnetic waves are evanescent in the normal direction, so they can only propagate along the surface at the interface between both materials. The physical meaning is that the electromagnetic wave is coupled to the polarization oscillations in the second medium, creating a new electromagnetic mode called a surface polariton. Coupling of EM-waves with plasmons in metals leads to surface plasmon polaritions, and with optical phonons, surface phonon polaritons.

Additional lets analyze the case s-polarized waves in a non-magnetic medium ($\mu_1 = \mu_2 = 1$), the Fresnel coefficients are given by:

$$r^{(s)} = \frac{k_{z_1} - k_{z_2}}{k_{z_1} + k_{z_2}}$$
$$t^{(s)} = \frac{k_{z_1}}{k_{z_1} + k_{z_2}}$$

As we can notice, there are no poles in the Fresnel coefficients for an s-polarized wave, since the equation $k_{z_1} + k_{z_2} = 0$ has no real solutions. Consequently, surface polaritons cannot be excited by means of s-polarized waves.

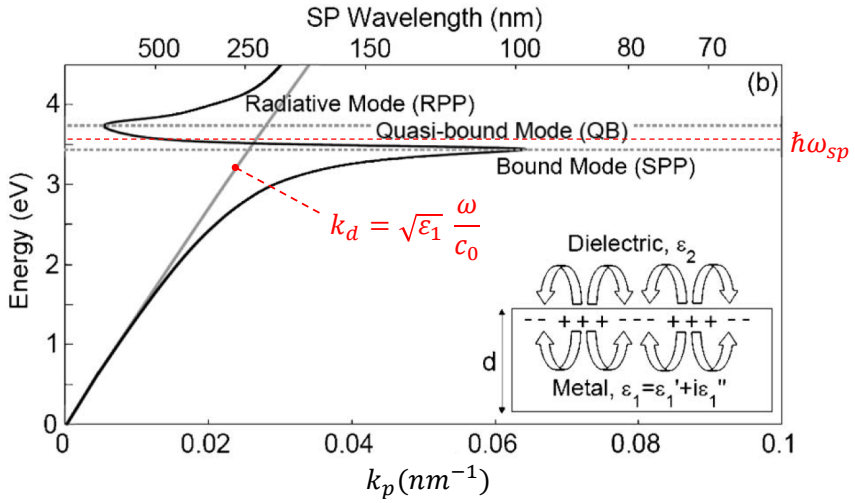

Figure 2.9: Surface plasmon dispersion relation for Ag/SiO_2 interface [40]. As a reference, the dispersion relation of EM-waves into the dielectric is drawn.

2.2.3 Dispersion Properties of Surface Plasmons

Direct substitution of Eqn. (2.16) into Eqn. (2.21), gives:

$$k_p = k_0\sqrt{\frac{\varepsilon_1}{\varepsilon_1+1}\cdot\frac{\omega_p^2-\omega^2-i\gamma\omega}{\omega^2-\omega_{sp}^2+i\gamma\omega}}, \tag{2.22}$$

where $\omega_{sp} = \frac{\omega_p}{\sqrt{1+\varepsilon_1}}$ is the Surface plasmon resonant frequency.

Eqn. (2.22) shows that the dispersion relation of surface plasmons polaritions (SPP) has a Lorentzian line shape, whose resonance is at a frequency ω_{sp} (Fig. 2.9). SPP correspond to the bound modes region, bellow the resonant frequency ω_{sp}, where the parallel wavevector is larger than the dispersion relation of the light in the dielectric (k_d). For frequencies larger than ω_{sp}, there is a zone of anomalous dispersion, characterized by modes with negative group velocities, called quasi-bound (QB) modes [40]. At even higher frequencies, the dispersion returns to a normal shape with positive group velocities. We call these modes radiative plasmon polaritons (RPP), since their parallel wave vector is smaller than that of the light in the dielectric, and so they are allowed to propagate back into the dielectric

media. At low frequencies, SPPs acquire the nature of a grazing-incidence light field, also known as Sommerfield-Zenneck waves [10], characterized by wave vectors with similar magnitude than the wave vector in the dielectric. Here, we will only focus on describing SPPs.

The energy carried by a SPP is given by:

$$P_{sp,d} = |r|^2 P_{inc} \cdot e^{-2Im[k_d]z - 2Im[k_p]x} \left(\hat{k}_d\right)$$
$$P_{sp,m} = |t|^2 P_{inc} \cdot e^{-2Im[k_m]z - 2Im[k_p]x} \left(\hat{k}_m\right),$$

where m stands for the metal side, d stands for the dielectric side, and P_{inc} is the power of the incident EM-wave. From this expression we can see that the energy of a SPP decays exponentially in the x-direction as $L_p = \frac{1}{2Im[k_p]}$, where L_p is the $1/e$ decay length. The exponential decay in the z-direction on the dielectric side represent the energy confinement of a SPP, and is quantified by $\hat{z} = \frac{1}{2Im[k_d]}$. SPPs with large L_p values are desirable in applications like SPP waveguiding, where transmission lines with low losses are required. On the other hand, energy confinement is inversely proportional to the E-field enhancement, and so large energy confinement (small $\hat{z}$), bellow the diffraction limit, are desirable in applications like optical sensing. Since the components of the wavevector are related by Eqns. (2.20a) and (2.20b), energy confinement and decay length are mutually dependent, and they show competing effects at different frequencies. The physical explanation is that large confinement on the dielectric side unavoidably induces more dissipation inside the metal (losses in metal, associated with $Im\left[\varepsilon_m\right]$, are larger than the losses in the dielectric) and consequently shorter $1/e$ decay lengths. For example, SPPs at silver/air interface at $\lambda_0 = 450$ nm shows a decay length and energy confinement of $L \approx 16$ μm and $\hat{z} \approx 180$ nm; while at $\lambda_0 = 1.5$ μm the decay length and energy confinement are $L \approx 1080$ μm and $\hat{z} \approx 2.6$ μm.

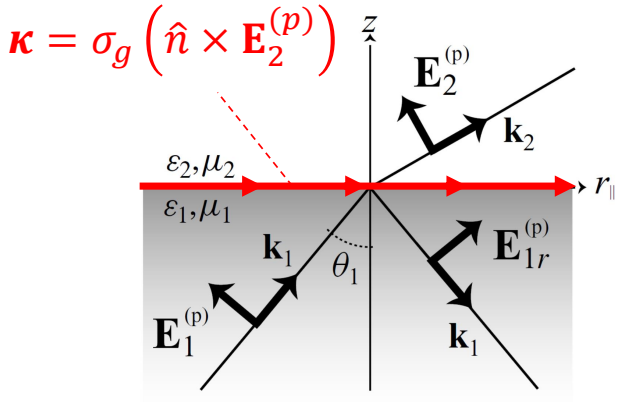

Figure 2.10: Reflection and transmission of an p-polarized EM-wave considering a surface current, $\boldsymbol{\kappa}$, at the interface between media 1 and 2. The surface current is defined by the product of the surface electrical conductivity, σ_g, and the component of the transmitted field parallel to the interface, $\hat{n} \times \boldsymbol{E}_2^{(p)}$.

Due to the large wave vector of SPPs compared with light in the dielectric, SPPs cannot be excited by direct illumination. Consequently, in order to increase the wavevector of the external beam, different techniques have been developed, like prism coupling, periodic grating surfaces, highly focused optical beams, and near field excitation [10].

Due to the large carrier densities in most metals *i.e.*, large ω_p, SPP resonant frequencies are found in the visible and near UV range. Scattering losses can dramatically affect the performance of SPPs, and so noble metals (low scattering frequencies γ) like silver, platinum or gold are the first preference in plasmonic applications. SPPs in metals exist normally in the visible range and so are preferred for applications like optical sensing and solar energy.

2.2.4 Graphene Plasmonics

Graphene has emerged as an alternative platform for surface plasmons. The reason lies in its large electron mobility and the metallic behavior under induction of charge carriers, that allows the excitation of surface plasmons with large energy confinement and decay lengths. Due to the low electron densities compared with noble metals (low ω_p), graphene

surface plasmons normally exist between the terahertz and mid-infrared range, although there is great amount of research devoted to push up the resonant frequencies to the visible range [15]. Additionally, the injection of carriers can be controlled by chemical doping or electrical gating, and so the frequency spectrum of surface plasmons in graphene can be tuned.

The study of electromagnetic waves interacting with a single layer of graphene can be approximated by representing a layer of graphene as a charged surface dividing two interfaces, as shown in Fig. 2.10. In the case of a charged interface, a modification of the Fresnel coefficients is needed in order to consider the discontinuity between the parallel components of the magnetic field, *i.e.*, $\hat{n} \times (\boldsymbol{H}_1 - \boldsymbol{H}_2) = \boldsymbol{\kappa} = \sigma_g (\hat{n} \times \boldsymbol{E}_2)$. Thus, the Fresnel coefficients for a p-polarized wave are given by:

$$r^{(p)} = \frac{\varepsilon_2 k_{z_1} - \varepsilon_1 k_{z_2} + \frac{\sigma_g}{\varepsilon_0 \omega} k_{z_1} k_{z_2}}{\varepsilon_2 k_{z_1} + \varepsilon_1 k_{z_2} + \frac{\sigma_g}{\varepsilon_0 \omega} k_{z_1} k_{z_2}} \tag{2.23a}$$

$$t^{(p)} = \frac{\sqrt{\varepsilon_1 \varepsilon_2} k_{z_1}}{\varepsilon_2 k_{z_1} + \varepsilon_1 k_{z_2} + \frac{\sigma_g}{k_0} k_{z_1} k_{z_2}}. \tag{2.23b}$$

According to Eqns. (2.23a) and (2.23b), the dispersion relation for SPPs in graphene is given by the solution of

$$\frac{\varepsilon_2}{\sqrt{\varepsilon_2 k_0^2 - k_p^2}} + \frac{\varepsilon_1}{\sqrt{\varepsilon_1 k_0^2 - k_p^2}} = -\frac{\sigma_g(\omega)}{\varepsilon_0 \omega}, \tag{2.24}$$

where we replace the Eqns. (2.20a) and (2.20b), into the respective values of k_{z_1} and k_{z_2}.

Solution of Eqn. (2.24) is not trivial, as the equation is non-linear. Fig. 2.11 shows the dispersion relation of graphene surface plasmons for different Fermi levels. For frequencies close to the resonant conditions, k_p becomes larger than the wavevector in the free space

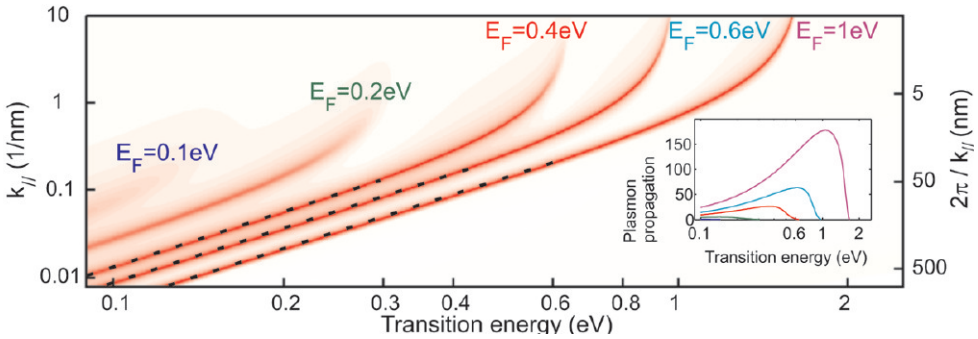

Figure 2.11: Dispersion relation of surface plasmons in graphene at different Fermi levels. Inset shoes the $1/e$ decay length in units of frequency cycles, L_p/λ_p, where λ_p is the wavelength of the surface plasmon [14].

($k_p \gg \sqrt{\varepsilon_1}k_0$ and $k_p \gg \sqrt{\varepsilon_2}k_0$) and Eqn. (2.24) can be approximated as

$$k_p \approx i\frac{\varepsilon_0\omega\left(\varepsilon_1+\varepsilon_2\right)}{\sigma_g(\omega)}. \tag{2.25}$$

2.2.5 Localized Surface Plasmons

We have seen that SPPs are propagating, dispersive electromagnetic waves coupled to the electric oscillations of polarizable materials at a dielectric interface. Localized surface plasmons on the other hand are non-propagating excitations of the conduction electrons of nanostructures coupled to the electromagnetic field. In this case, the curved surface of the particle exerts an effective restoring force on the driven electrons, so that a resonance can arise, leading to field amplification both inside and in the near-field zone outside the particle. Another consequence of the curved surface is that plasmon resonances can be excited by direct light illumination, in contrast to propagating SPPs.

The interaction of a particle of size D with the electromagnetic field can be analyzed using the simple quasi-static approximation [41], provided that $D \ll \lambda$, *i.e*, the particle is much smaller than the wavelength of light in the surrounding medium. In this case, the phase of the harmonically oscillating electromagnetic field is practically constant over the

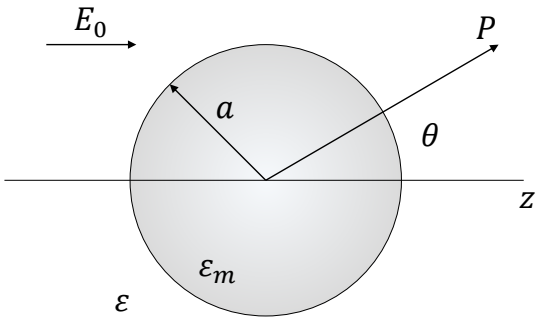

Figure 2.12: Sketch of a homogeneous sphere placed into an electrostatic field.

particle volume, so that one can calculate the spatial field distribution by assuming the simplified problem of a particle in an electrostatic field (the magnetic fields vanish in this regime). The harmonic time dependence can then be added to the solution once the field distributions are known.

Consider a homogeneous isotropic sphere of radius a, that is surrounded by a static field $E = E_0\hat{z}$ (Fig. 2.12). Under the influence of the oscillating electric field, the particle becomes polarized. The electric field inside the particle $\boldsymbol{E}_{in}$ and outside $\boldsymbol{E}_{out}$ (near to the particle surface), are given by [24]:

$$\boldsymbol{E}_{in} = \frac{3\varepsilon}{\varepsilon_m + 2\varepsilon}\boldsymbol{E}_0 \tag{2.26a}$$

$$\boldsymbol{E}_{out} = \boldsymbol{E}_0 + \frac{3\hat{n}(\hat{n}\cdot\boldsymbol{p}) - \boldsymbol{p}}{4\pi\varepsilon_0\varepsilon}\frac{1}{r^3}, \tag{2.26b}$$

where $\boldsymbol{p}$ is the dipole moment developed inside the particle, given by:

$$\boldsymbol{p} = 4\pi\varepsilon_0\varepsilon a^3\frac{\varepsilon_m - \varepsilon}{\varepsilon_m + 2\varepsilon}\boldsymbol{E}_0. \tag{2.27}$$

From here, it becomes evident that the dipole moment experiences a resonant condition at a frequency ω_{lpr}, when $Re\left[\varepsilon_m(\omega_{lsp})\right] \approx -2\varepsilon$, which again can be satisfied for polarizable materials ($\varepsilon_m < 0$). We call this localized polaritons resonance (LPR). In the case of metals,

direct substitution of Eqn. (2.16) into Eqn. (2.27), ignoring scattering losses ($\gamma = 0$), gives that the resonant condition is reached at $\omega_{lpr} = \omega_p/\sqrt{2\varepsilon}$; where we notice a strong dependence with the properties of the surrounding media.

The solution given in Eqn. (2.27) is a simplified expression to explain the modification of the nature of surface plasmons, as a result of the confinement of the polarizable charges inside a geometry smaller than the wavelength of light in the surrounding media. In a general case however, there is more than a dipolar resonant condition as the charges inside the particle can reach different resonant modes, in analogy to electronic energy levels in the hydrogen atom model as a result of the confinement of electrons into a small energy potential. Furthermore, besides the dependence of ω_{lpr} on the surrounding media, the frequency can be also tuned by other factors like the shape and size of the particle.

2.3 Surface Plasmons Hybridization Theory

The strong light confinement in a plasmonic nanoparticle is known to produce strong interaction with the electric charges located near its surface. As a result, when a second nanoparticle is brought in near proximity, a strong coupling occurs. This coupling induces strong modifications in the spectral response compared to a single particle. This phenomenon, known as surface plasmon hybridization, in analogy to the hybridization of molecular orbitals and has been the subject of numerous studies given its potential to produce non-symmetric resonances [11], tuning of radiative properties [12] and waveguiding [13].

Under the electrostatic approximation, surface plasmon hybridization can be studied by the so-called boundary charge method [42, 43], which replaces the volumetric response of the particle by an equivalent surface charge density. The method has variations depending on if the objects are 2D or 3D. In this section, we describe the general formalism

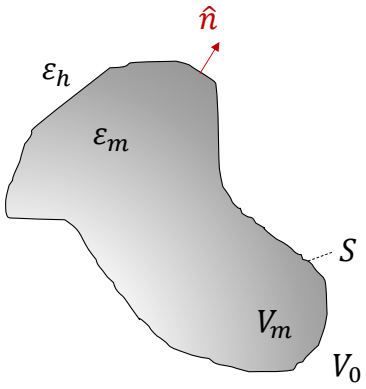

Figure 2.13: Sketch of a homogeneous nanoparticle of dielectric constant ε_m in a host environment of dielectric constant ε_h.

considered for the study of 2D and 3D nanoparticles. The specific form of this formalism for nanospheres and graphene nanodisks, which correspond to models used in this work, are given in Appendices A.1 and A.2.

The solution obtained from the boundary charge method set the basis for other calculations like absorption and scattering of plane waves, near-field radiation heat transfer, and plasmonic bandstructure. The details of these calculations are provided in the appendices B, C and D, respectively.

2.3.1 Hybridiation theory for 3D nanoparticles

Consider a nanoparticle of arbitrary shape of dielectric constant ε_m in a dielectric host of dielectric constant ε_h, as shown in Fig. 2.13. Under the electrostatic approximation, the problem reduces to finding the electrostatic potential, ψ, satisfying the following set of

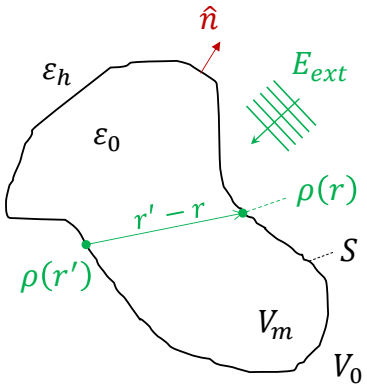

Figure 2.14: Sketch of the surface charge at a position $\boldsymbol{r}$ interacting with other charges at $\boldsymbol{r}'$ and an external electric field $\boldsymbol{E}_{ext}$. The nanoparticle has a surface charge labeled by S.

equations:

$$\nabla^2\psi = 0 \text{ in } V_m, \tag{2.28a}$$

$$\nabla^2\psi = 0 \text{ in } V_0, \tag{2.28b}$$

$$\psi\big|_{S^-} = \psi\big|_{S^+} \tag{2.28c}$$

$$\varepsilon_m \left(\hat{n}\cdot\nabla\psi\right)\big|_{S^-} = \varepsilon_h \left(\hat{n}\cdot\nabla\psi\right)\big|_{S^+}, \tag{2.28d}$$

$$\lim_{r\to\infty} \psi = 0, \tag{2.28e}$$

Solution of Eqns. (2.28a)–(2.28e) can be obtained by replacing the volumetric charge density in V_m by a surface charge density ρ at the surface S. These surface charge mimic the overall response of the nanoparticle. The electric field and potential at a position r created by the surface charge is given by:

$$\boldsymbol{E}'(\boldsymbol{r}) = \frac{1}{4\pi\varepsilon_0}\int_{S'} \frac{\boldsymbol{r}-\boldsymbol{r}'}{|\boldsymbol{r}-\boldsymbol{r}'|^3}\rho(\boldsymbol{r}')dS', \tag{2.29a}$$

$$\psi(\boldsymbol{r}) = \frac{1}{4\pi\varepsilon_0}\int_{S'} \frac{1}{|\boldsymbol{r}-\boldsymbol{r}'|}\rho(\boldsymbol{r}')dS'. \tag{2.29b}$$

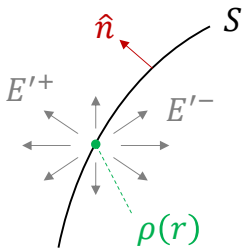

Figure 2.15: Sketch of the electric field induced by a surface charge at the surface S

The solution given by Eqn. (2.29b) automatically satisfies Eqns. (2.28a)–(2.28c) and (2.28e). In order to solve Eqn. (2.28d), we first consider the total electric field at r induced by the surface charge at r and the rest of surface charges in the domain, as shown in Fig. 2.14. Mathematically, this is expressed as

$$\boldsymbol{E}(\boldsymbol{r}) = \boldsymbol{E}'(\boldsymbol{r}) + \frac{1}{4\pi\varepsilon_0}\int_{S'}\frac{\boldsymbol{r}-\boldsymbol{r}'}{|\boldsymbol{r}-\boldsymbol{r}'|^3}\rho(\boldsymbol{r}')dS' + \boldsymbol{E}_{ext}(\boldsymbol{r}), \tag{2.30}$$

where $\boldsymbol{E}_{ext}$ is an external electric field and $\boldsymbol{E}'(\boldsymbol{r})$, is the induced field due to the existence of a surface charge at r.

In order to find $\boldsymbol{E}'(\boldsymbol{r})$, it is instructive to analyze the effect of the existence of a surface charge in the surface S. As shown in Fig. 2.15, a surface charge located a r induces electric fields propagating inside, $\boldsymbol{E}'^{-}$, and outside, $\boldsymbol{E}'^{+}$, the particle. It can be demonstrated that this fields are related to the surface charge by [44]:

$$\hat{n}_r \cdot \boldsymbol{E}'^{-}(\boldsymbol{r}) \simeq -\frac{\rho(\boldsymbol{r})}{2\varepsilon_0}, \tag{2.31a}$$

$$\hat{n}_r \cdot \boldsymbol{E}'^{+}(\boldsymbol{r}) \simeq \frac{\rho(\boldsymbol{r})}{2\varepsilon_0}, \tag{2.31b}$$

Introducing Eqns. (2.31a) and (2.31b) into Eqn. (2.30) gives

$$\hat{n}_r \cdot \boldsymbol{E}^-(\boldsymbol{r}) = -\frac{\rho(\boldsymbol{r})}{2\varepsilon_0} + \frac{1}{4\pi\varepsilon_0}\int_{S'} \frac{\hat{n}_r \cdot (\boldsymbol{r}-\boldsymbol{r}')}{|\boldsymbol{r}-\boldsymbol{r}'|^3}\rho(\boldsymbol{r}')dS' + \hat{n}_r \cdot \boldsymbol{E}_{ext}(\boldsymbol{r}), \tag{2.32a}$$

$$\hat{n}_r \cdot \boldsymbol{E}^+(\boldsymbol{r}) = +\frac{\rho(\boldsymbol{r})}{2\varepsilon_0} + \frac{1}{4\pi\varepsilon_0}\int_{S'} \frac{\hat{n}_r \cdot (\boldsymbol{r}-\boldsymbol{r}')}{|\boldsymbol{r}-\boldsymbol{r}'|^3}\rho(\boldsymbol{r}')dS' + \hat{n}_r \cdot \boldsymbol{E}_{ext}(\boldsymbol{r}), \tag{2.32b}$$

Substitution of Eqns. (2.32a) and (2.32b) into Eqn. (2.28d) gives

$$\frac{1}{2}\eta\ \rho(\boldsymbol{r}) = \frac{1}{4\pi}\int_{S'} \frac{\hat{n}_r \cdot (\boldsymbol{r}-\boldsymbol{r}')}{|\boldsymbol{r}-\boldsymbol{r}'|^3}\rho(\boldsymbol{r}')dS' - \varepsilon_0\left[\hat{n}_r \cdot \boldsymbol{E}_{ext}(\boldsymbol{r})\right] \tag{2.33}$$

where

$$\eta = \frac{\varepsilon_h + \varepsilon_m}{\varepsilon_h - \varepsilon_m} \tag{2.34}$$

It can be demonstrated [42], that for object of arbitrary shape Eqn. (2.33) can be solved by a set of eigenfunctions, β_k, satisfying the orthogonality property

$$\int_S\int_{S'} \beta_l(\boldsymbol{r})\frac{1}{|\boldsymbol{r}-\boldsymbol{r}'|}\beta_k(\boldsymbol{r}')dS'dS = \delta_{lk}.$$

By expanding the surface charge density as $\rho = \sum_k c_k\beta_k$, replacing into Eqn. (2.33) and taking the inner product with the functions $\varphi_l = \int_S \beta_l(\boldsymbol{r})\frac{1}{|\boldsymbol{r}-\boldsymbol{r}'|}dS$, we get

$$\left[\boldsymbol{G} - \boldsymbol{G}^0\right]\boldsymbol{c} = \boldsymbol{X}, \tag{2.35}$$

where the interaction matrices $\boldsymbol{G}$, $\boldsymbol{G}^0$, and $\boldsymbol{X}$ are given by:

$$G_{lk} = \frac{1}{2}\eta\langle\varphi_l, \beta_k\rangle \tag{2.36a}$$

$$G^0_{lk} = \langle\varphi_l, \Upsilon * \beta_k\rangle \tag{2.36b}$$

$$X_l = \langle\varphi_l, E_{ext}\rangle, \tag{2.36c}$$

and

$$\Upsilon = \frac{\hat{n}_r \cdot (\boldsymbol{r} - \boldsymbol{r}')}{|\boldsymbol{r} - \boldsymbol{r}'|^3}.$$

Here, $\langle \cdot\cdot, \cdot\cdot \rangle$ represents the standard inner product $\langle u, v \rangle = \int d^2\boldsymbol{r}\ (u^* v)$, and the $*$ symbol represents the transformation

$$Q * \beta = \int_{S'} Q(\boldsymbol{r}, \boldsymbol{r}')\beta(\boldsymbol{r}')dS'.$$

Solution of Eqn. (2.35) gives the overall response of the nanoparticle under an external electromagnetic field. The real advantage of this method lies in the analysis of systems of multiple nanoparticles interacting under an external electric field. Considering a system of N nanoparticles, the fundamental equation representing the interaction between the nanoparticle n and the surrounding nanoparticles and external field is

$$\frac{1}{2}\eta_n\ \rho^n(\boldsymbol{r}_n) = \sum_{m=1}^{N} \frac{1}{4\pi} \int_{S_m} \frac{\hat{n}_r \cdot (\boldsymbol{r}_n - \boldsymbol{r}_m)}{|\boldsymbol{r}_n - \boldsymbol{r}_m|^3} \rho^m(\boldsymbol{r}_m) dS_m - \varepsilon_0 \left[\hat{n}_r \cdot \boldsymbol{E}_{ext}(\boldsymbol{r}_n)\right]. \tag{2.37}$$

By following a similar procedure as before, we derive

$$\left[\sum_{\nu=1}^{N} \boldsymbol{G}^{\nu} - \boldsymbol{G}^{0}\right] \boldsymbol{c} = \boldsymbol{X}, \tag{2.38}$$

where the interaction matrices $\boldsymbol{G}^{\nu}$ and $\boldsymbol{G}^{0}$ are composed of $N \times N$ sub-matrices whose elements are given by:

$$G^{\nu,mn}_{j_m j_n} = \begin{cases} \frac{1}{2}\eta_n \langle \varphi^m_{j_m}, \beta^n_{j_n} \rangle & \text{if } m = n = \nu \\ 0 & \text{Otherwise} \end{cases} \tag{2.39}$$

$$G^{0,mn}_{j_m j_n} = \langle \varphi^m_{j_m}, \Upsilon * \beta^n_{j_n} \rangle, \tag{2.40}$$

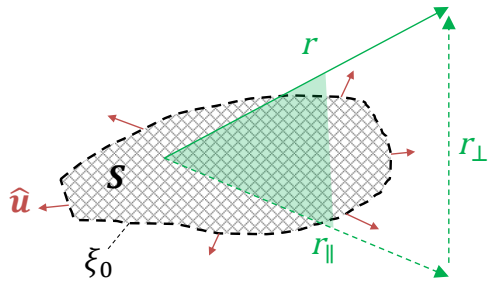

Figure 2.16: Schematic representation of a graphene nanostructure and the coordinates considered for the electrostatic theory.

and $\boldsymbol{X}$ is a column matrix composed of N sub-matrices of the form $X^m_{jm} = \langle \varphi^m_{jm}, E_{ext} \rangle$. Solution of Eqn. (2.38) gives the magnitude of the expansion coefficients c and thus the total response of the system of N nanostructures.

The specific form of the bi-orthogonal basis and the interaction matrices for a sphere geometry is given in Appendix A.1.

2.3.2 Hybridization theory for 2D nanostructures

Consider a 2D nanostructure as a flat conducting surface with no thickness (Fig. 2.16). In the electrostatic regime, the electromagnetic response of a graphene nanostructure located between two media with dielectric constants ε_1 and ε_2 is given by the electric potential ψ that results from the induced surface charge density ρ as [15]

$$\psi_{out}(\boldsymbol{r}) = \frac{1}{\varepsilon_0 \varepsilon_m} \int_S d^2\boldsymbol{r}'_{\parallel} \; K(\boldsymbol{r}, \boldsymbol{r}'_{\parallel}) \rho(\boldsymbol{r}'_{\parallel}). \tag{2.41}$$

Here, $\varepsilon_m = \frac{\varepsilon_1 + \varepsilon_2}{2}$, and $K(\boldsymbol{r}, \boldsymbol{r}') = \frac{1}{4\pi|\boldsymbol{r} - \boldsymbol{r}'|}$ is the Green's function anywhere outside the graphene nanostructure and $\boldsymbol{r} = \boldsymbol{r}_{\parallel} + \boldsymbol{r}_{\perp}$ is a vector defined by components on the surface, $\boldsymbol{r}_{\parallel}$ and normal to the surface, $\boldsymbol{r}_{\perp}$, as shown in Fig. 2.16. The integration domain, S, is defined along the surface of the nanostructure. This solution automatically satisfies Eqns. (2.28a), (2.28b), (2.28d) and (2.28e).

The induced surface charged density is related to the induced electric potential at the surface, ψ_{in}, by the continuity equation ($\nabla_{\parallel} \cdot \boldsymbol{J} = i\omega\rho$, where $\nabla_{\parallel}$ is the two dimensional nabla operator) and by representing the surface current in terms of the electric potential as $\boldsymbol{J} = -f(\boldsymbol{r}_{\parallel})\sigma(\omega)\nabla_{\parallel}\psi_{in}$, which gives the expression [15]

$$i\omega\rho = -\nabla_{\parallel} \cdot \left[\sigma(\omega) f(\boldsymbol{r}_{\parallel}) \nabla_{\parallel}\psi_{in}\right]. \tag{2.42}$$

Here, $\sigma(\omega)$ is the optical conductivity of the nanostructure and $f(\boldsymbol{r}_{\parallel})$ is a filling function that is unity inside the graphene nanostructure domain and zero elsewhere.

We express ψ_{in} as a function of ρ using an appropriate choice of Green's function as [45]

$$\psi_{in}(\boldsymbol{r}_{\parallel}) = \frac{i\omega}{\sigma(\omega)} \int_S d^2\boldsymbol{r}'_{\parallel}\ g(\boldsymbol{r}_{\parallel}, \boldsymbol{r}'_{\parallel})\rho(\boldsymbol{r}'_{\parallel}), \tag{2.43}$$

where $g(\boldsymbol{r}_{\parallel}, \boldsymbol{r}'_{\parallel})$ is a Green's function satisfying the relations

$$f\nabla^2_{\parallel} g = -\delta(\boldsymbol{r}_{\parallel} - \boldsymbol{r}'_{\parallel})$$
$$\left[\hat{u} \cdot \nabla_{\parallel} g\right]\Big|_{\boldsymbol{r}_{\parallel}=\xi_0} = 0,$$

where ξ_0 represents the contour of the nanostructure and $\hat{\boldsymbol{u}}$ is a vector normal to the edge of the nanostructure.

In the definition of Eqn. (2.43) we assume no tunneling of charges at nanostructure's edge [45], *i.e.*,

$$\left[\hat{u} \cdot \nabla_{\parallel} \psi_{in}\right]\Big|_{\boldsymbol{r}_{\parallel}=\xi_0} = 0,$$

,

The electrostatic interaction of a system with N 2D nanostrutures and an external field with an electric potential, ψ_{ext}, is modeled by using Eqns. (2.41) and (2.43) and

substituting to Eqn. (2.28d). For example, the continuity of the electric potential at the surface of a nanostructure n gives [24]

$$\psi_{in}^{n}(\boldsymbol{r}'_n - \boldsymbol{r}_n) = \sum_{\nu=1}^{N} \psi_{out}^{\nu}(\boldsymbol{r}'_n - \boldsymbol{r}_\nu) + 2\psi_{ext}(\boldsymbol{r}'_n). \tag{2.44}$$

The summation on the right-hand side of Eqn. (2.44) accounts for the interaction of the nanostructure n with the rest of the nanostructures ν ($\nu = 1, 2, ...N$), including the interactions with its own induced electrostatic potential, i.e $\psi_{out}^{n}(\boldsymbol{r}'_n - \boldsymbol{r}_n)$. A factor of two is considered in the external field potential as the field acts on both sides of the nanostructure surface.

We construct a system of N equations by applying Eqn. (2.44) to each nanostructure. The solution is found by expanding the surface charge density $\rho^{\nu}, \nu = 1, 2...N$ into a set of normal modes and taking the inner product on both sides of Eqn. (2.44). The surface current expansion is represented as

$$\rho^{\nu}(\boldsymbol{r}_{\parallel}) = \sum_{j}^{\infty} c_j^{\nu} \beta_j^{\nu}(\boldsymbol{r}_{\parallel}), \tag{2.45}$$

where c_j^{ν} and β_j^{ν} are the j-mode constant and function basis in the nanostructure ν.

We finally derive the system of equations

$$\frac{1}{2}\left[\sum_{\nu=1}^{N} \boldsymbol{G}^{\nu} - \boldsymbol{G}^{0}\right] \boldsymbol{c} = \boldsymbol{X}, \tag{2.46}$$

where the interaction matrices $\boldsymbol{G}^{\nu}$ and $\boldsymbol{G}^{0}$ are composed of $N \times N$ sub-matrices whose

elements are given by:

$$G^{\nu,mn}_{j_m j_n} = \begin{cases} \frac{i\omega}{\sigma(\omega)} \langle \beta^m_{j_m}, g^\nu * \beta^n_{j_n} \rangle & \text{if } m = n = \nu \\ 0 & \text{Otherwise} \end{cases} \tag{2.47}$$

$$G^{0,mn}_{j_m j_n} = \frac{1}{\varepsilon_0 \varepsilon^m_h} \langle \beta^m_{j_m}, K * \beta^n_{j_n} \rangle, \tag{2.48}$$

and $\boldsymbol{X}$ is a column matrix composed of N sub-matrices of the form $X^m_{j_m} = \langle \beta^m_{j_m}, \psi_{ext} \rangle$.

The specific form of the bi-orthogonal basis and the interaction matrices for a two dimensional disk geometry is given in Appendix A.2.

Extreme Blueshift of Localized Surface Plasmons in Graphene Nanodisk Stacks

3.1 Introduction

Surface plasmons on doped graphene have attracted significant interest due to their extraordinary properties, like strong field confinement, long propagation distance and tunability, making them an attractive alternative to surface plasmons on noble metals [14, 46]. A number of experiments have demonstrated that localized surface plasmons can be effectively excited by free space photons in graphene nanostructures like nanodisks or nanoribbons [14, 46], which offers the possibility to control the resonant frequencies not only by chemical doping or gate voltage, but also by adjusting the nanostructure size [14]. However, graphene surface plasmons normally exist in the mid-infrared (IR) and terahertz range, due to the low carrier concentrations attainable in graphene in comparison with noble metals [17, 46]. While the resonant frequency of a graphene nanostructure can be blueshifted in theory by increasing its carrier concentration or reducing its size [47, 48], it is still experimentally challenging to push the resonant frequency significantly beyond the mid-IR range. An alternative method to increase the resonant frequency of graphene surface plasmons beyond the mid-IR range is by critical coupling of surface plasmons in single-layer graphene with wave guided modes [16]. Through this method it has been proven that it is possible to achieve a strong optical response at a wavelength of 1.5 μm. However,

since the physical mechanism used by this approach is based on the absorption properties of graphene beyond the plasmonic response, some interesting features of surface plasmons like electrical tunability or field enhancement cannot be explored. Another feasible method for increasing surface plasmon resonant frequency in graphene is via surface plasmon hybridization [46, 49]. Due to the quantum nature of Dirac fermions, plasmon hybridization by using graphene stacks can efficiently increase the resonant frequency and the amplitude of surface plasmon modes [17, 18].

In this work we investigate the extreme blueshift of the surface plasmon resonant frequency by plasmon hybridization in graphene disk stacks. We begin with an analysis of the hybridization of surface plasmon modes by reducing the distance between disks. Then we focus on hybrid modes whose resonant frequencies are blueshifted with respect to their original uncoupled modes and study the physical mechanism involved in the hybridization process. In the last section, we explore some extreme cases, regarding the maximum gap between disks for strong coupling between surface plasmons, maximum blueshift of resonant frequency physically attainable through hybridization in a stack configuration, and the absorption and scattering spectrum for an extreme blueshift case. Our work is focused on dipolar plasmons, since these modes can be easily excited by plane waves. The study is based on semi-analytical expressions obtained from the problem of graphene disk stacks under a non-retarded approach, which has been proved to accurately represent the interaction between electromagnetic waves and localized surface plasmons on graphene nanostructures at long wavelengths [50, 51, 52, 53]. Our method is a combination of the work done by Fetter [45] to extract the eigenmodes of the uncoupled surface plasmons for disk geometry and optical coupling theory [54], which considers the effects of interparticle coupling. Through the optical coupling theory, we construct a eigenvalue equation, from which the coupled or hybrid modes are extracted. Unlike the coupled dipole theory [52],

whose formulation is restricted to cases where the distance between bodies is larger than their characteristic dimensions, the optical coupling theory has the advantage of providing enough accuracy even at small distances, since its fundamentally considers the multiple interactions between all the eigenmodes.

By using the direct implementation of the optical coupling theory to model the coupling between graphene nanostructures, we develop a complete and robust methodology for analyzing the interactions between graphene nanostructures and an external field that is simple and accurate. Some important results can be easily extracted, e.g., the interaction between eigenmodes and between nanostructures, as well as scattered or absorbed power. This methodology can also be extended to other graphene nanostructures like semi-infinite sheets, nanoribons and nanorings, whose analytical solutions for a quasi-static field have been derived previously.

Though the fundamentals of this method rely on the electrostatic approximation, we confirm though comparison with numerical simulations based on the boundary element method (BEM) that our results remains fairly accurate for a broad spectrum.

3.2 Methods

The optical response of graphene is modeled considering the optical conductivity from Eqn. (2.18). The near-field coupling between graphene disks is calculated under the electrostatic approximation [41]. The solution is obtained using the boundary charge method from Section 2.3.2. The hybrid eigenfrequencies and eigenvectors are obtained from the eigenvalue problem in Eqn. (D.1). The scattering and absorption cross sections are extracted from Eqns. (B.4) and (B.7).

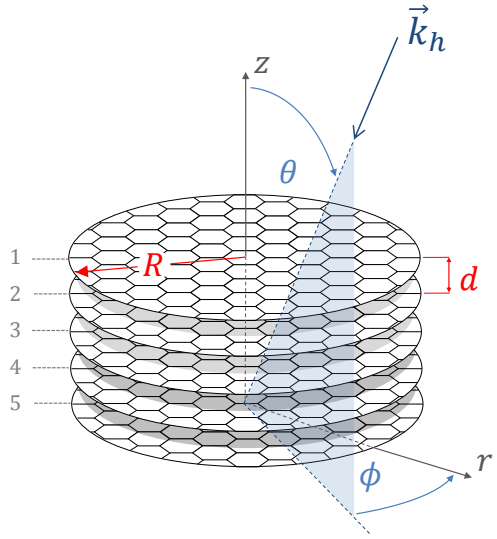

Figure 3.1: Schematic of the graphene disks stack structure considered for the analysis.

3.3 Results and Discussions

3.3.1 Analysis of surface plasmon hybridization in disk stacks

In our study, we consider a stack of graphene disks with a radius R, separated by a distance d (Fig. 3.1). The disks are labeled from top to bottom starting from 1 to N, where N is the number of disks stacked. In order to include the effects of the substrate, we assume that the stacked structure is totally embedded in the host material ε_h. For the results of scattered and absorbed power, we consider an incident plane wave whose direction is defined by the zenith θ and azimuth ϕ angles according to Fig. 3.1.

From hybridization theory [55, 56], it is known that when two or more graphene disks are stacked together, each uncoupled mode splits into N hybrid modes. This is a result of the mutual interaction between the evanescent fields from each disk [12]. For example, hybridization in a two disks stack causes each base mode to split into a higher frequency mode or bright mode, and a lower frequency mode or dark mode [51]. In general, the number of hybrid modes is very large and it is very difficult to distinguish their associated

uncoupled modes. A large distances, however, the coupling between disks is very weak, so that the magnitude of the hybrid eigenvalues λ_γ remains very close to their original ith uncoupled mode λ_i. Thus we can track the evolution of the hybrid modes as a function of R/d, beginning with a small value of R/d, which allow us to link each hybrid mode with its original uncoupled mode. We represent this process with the parameter $\lambda_i/\lambda_{\gamma,i}$, where $\lambda_{\gamma,i}$ is the eigenvalue of the γ hybrid mode derived from the ith uncoupled mode. In the case of non-dispersive materials, this relation can be approximated as a relation of their respective eigenfrequecies as follows:

$$\frac{\lambda_i}{\lambda_{\gamma,i}} = \frac{\omega_{\gamma,i}\sigma(\omega_i)}{\omega_i\sigma\left(\omega_{\gamma,i}\right)} \approx \left(\frac{\omega_{\gamma,i}}{\omega_i}\right)^2. \tag{3.1}$$

To derive this equation, we ignore the effect of the relaxation time τ and inter-band transitions on the conductivity of graphene. However, we observe that this approximation does not significantly alter the results, in comparison with those using the whole expression of the optical conductivity.

We study the evolution of $\omega_{\gamma,i}/\omega_i$ as a function of R/d in disk stacks with different number of disks. Here, only the results for a stack of 5 graphene disk are shown (Fig. 3.2). However, similar conclusions can be drawn for stacks with different number of disks. As the relative distance R/d is increased, we observe that the lowest uncoupled mode ($i = 1$) splits into 5 branches. At relatively large separation between disks ($R/d \sim 1$), we observe the hybrid modes are separated evenly. However at $R/d > 100$ we observe that only one mode goes to higher frequency.

In order to analyze the effective response of this structure, we calculate the absorption efficiency (Absorption Cross Section/DiskArea) for 5 graphene ($E_f = 0.6$ eV) disks stacked, with 100 nm diameter, and 30 nm gap between disks (Fig. 3.3). In nondimensional units, this corresponds to $R/d \approx 1.67$ (dashed line in (Fig. 3.2). Analysis of the effective response

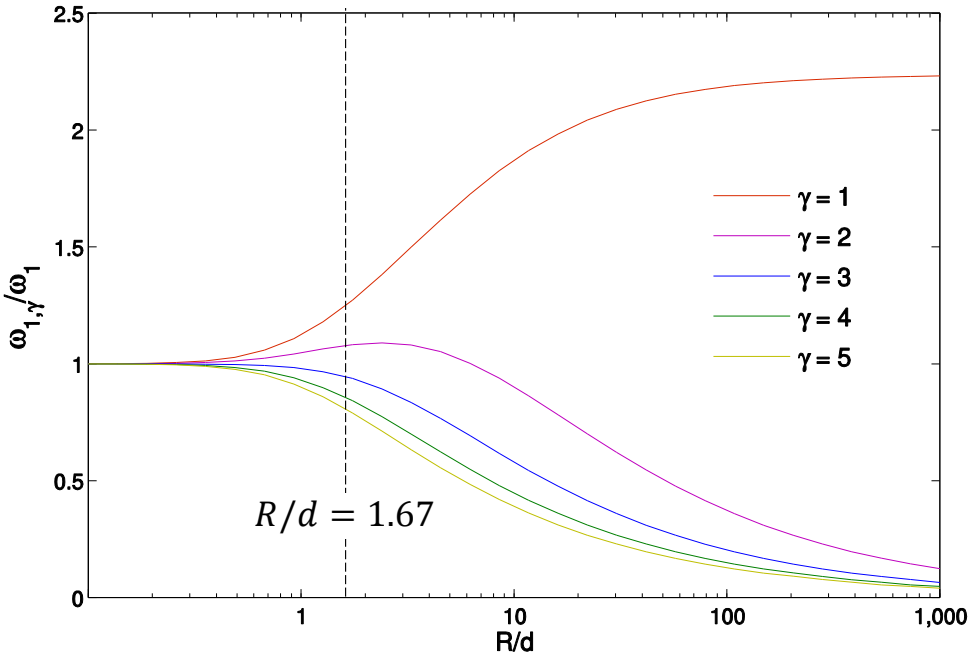

Figure 3.2: Splitting of the normalized resonant frequency of first base mode into hybrid modes in a five diskssstack configuration.

reveals that at the highest frequency mode, all the disks reach a resonant condition. This is represented by the simultaneous peaks in the absorption efficiency of each disk, indicating that this mode has also the largest intensity. For the rest of the hybrid modes, we can find that only a few disks resonate together. Our results show good agreement with numerical simulations using the BEM [33].

Plasmon hybridization is the consequence of mutual interaction between the different eigenmodes from each particle. However, by analyzing the expansion coefficients in two disks stack [Fig. 3.4(a)], we find that the hybridization of the first base mode is mainly driven by mutual interactions between the uncoupled modes of the same first level. This is due to the resonant factor in the expression of the expansion coefficients in Eqn. (2.46). In the case of hybridization of the first base mode in a two disks stack, the resonant frequency of the hybrid mode is always closer to the resonant of the first base eigenmode than the resonant frequency of higher order base modes, which means that the resonant factor of

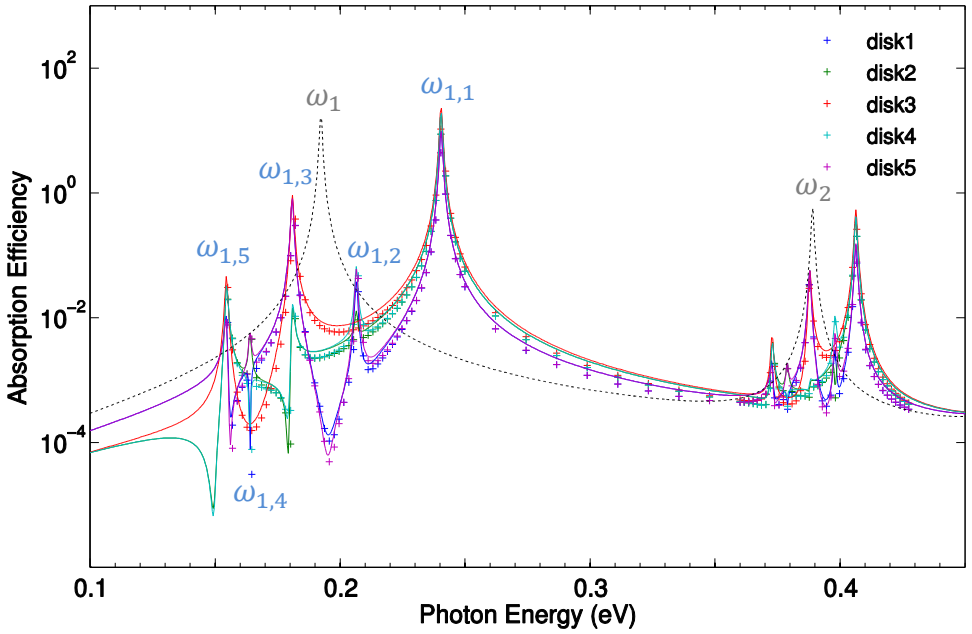

Figure 3.3: Absorption efficiency for 5 graphene disk stacked ($D = 100$ nm; $E_f = 0.6$ eV, $d = 30$ nm, $\varepsilon_h = 1$). Light incident normal to the disk array ($\theta = 0, \phi = 0$). The black dashed line represents the absorption efficiency of one graphene disk regarding similar features. The small crosses correspond to results from numerical simulation by the boundary element method (BEM) [33]

the first mode in Eqn. (2.46) is dominant [54].

Based on this finding, we derive an analytical expression to predict the resonant frequency of the bright ($\omega_{i,+}$) and dark ($\omega_{i,-}$) hybrid modes of the ith uncoupled mode in a two disks stack:

$$\left(\frac{\omega_{i,\pm}}{\omega_i}\right)^2 - 1 = \pm\pi\left(2i+\frac{3}{2}\right)\left(2i+\frac{5}{2}\right)\int_0^\infty \left(\frac{J_{2i+2}(p)}{p}\right)^2 e^{-\frac{d}{R}p}dp. \tag{3.2}$$

This expression can be derived from the eigenvalue problem from Eqn. (D.1), considering only the interaction between the ith eigenmode $|\rho_i\rangle$ and the first term of the polynomial expansion from Eqn. (A.4), together with the properties of the Bessel functions [45]. Although the results are not shown here, we find that considering only the first polynomial term in the expansion of Eqn. (A.4), does not add a significant loss of accuracy compared

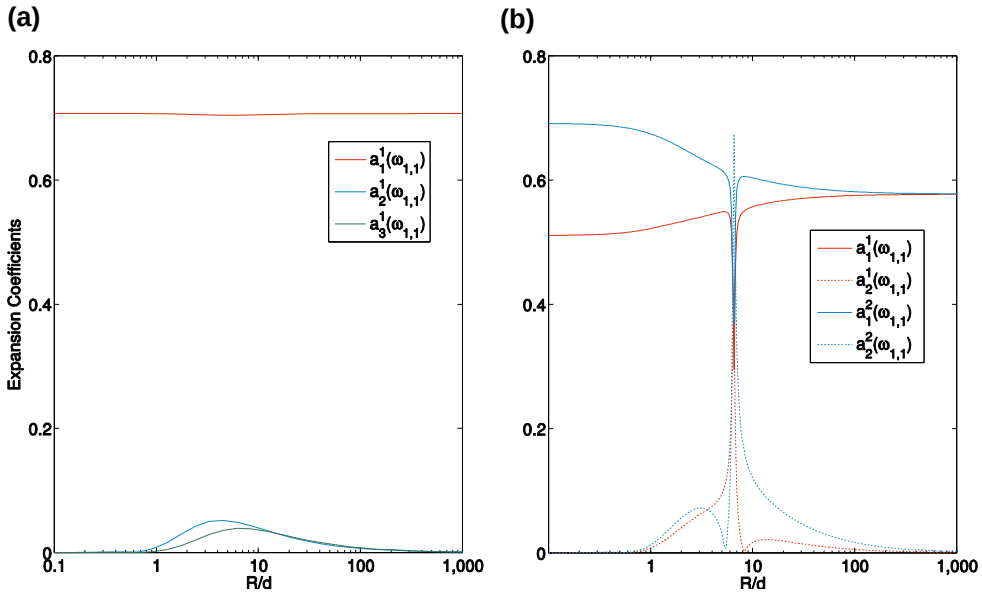

Figure 3.4: Expansion coefficients for graphene disk stacks at $\omega_{1,1}$ for: (a) two disks, (b) three disks.

with the results for an expansion with a larger number of polynomials.

For disk stacks having a larger number of disks, we observe that hybridization of the ith base mode is mainly driven by the coupling of base modes of the same order, with exceptions when the resonant of the high frequency hybrid mode meets the resonant of a higher order base mode [Fig. 3.4(b)]. When this occurs, there is a significant contribution from the higher order base modes due to the coupling between them. At $R/d \approx 10$, the contribution of the second base-mode is on the same order of magnitude with the first mode. However, we find that the whole distribution can be accurately described by considering only the dominant base mode, so this small perturbation can be ignored.

3.3.2 Blueshift of surface plasmon resonant frequency

In this section we study the blueshift of the resonant frequency in graphene disk stack. We restrict our analysis to the high frequency branch derived from the lowest uncoupled mode ($\omega_{1,1}$), since the this mode has the largest intensity.

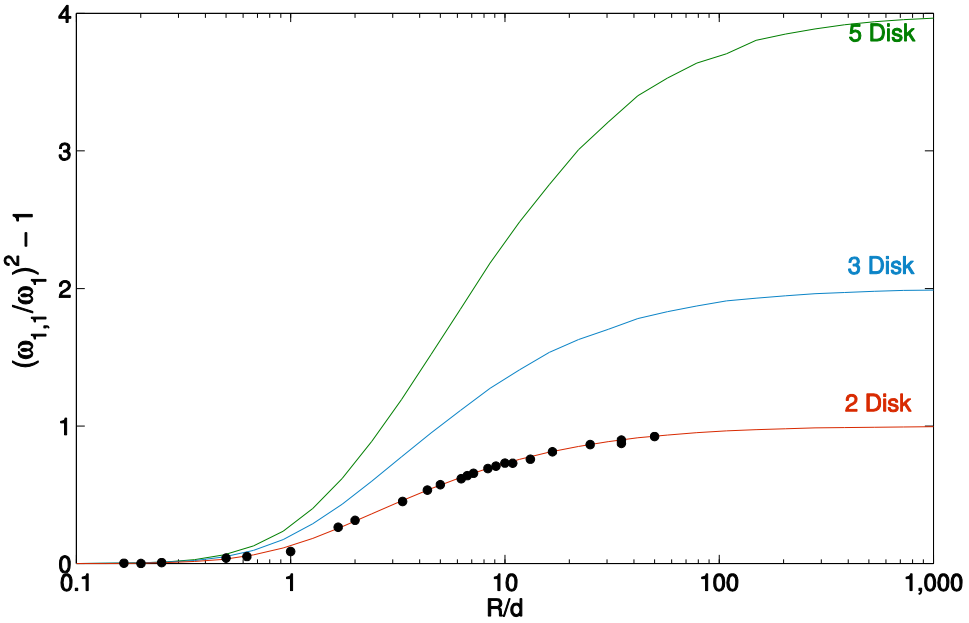

Figure 3.5: Normalized resonant frequency of the high frequency hybrid mode from the lowest uncoupled mode ($k = 0$), for stacks with different number of disks.

In Fig. 3.5, we plot the dispersion of the high frequency branch ($\omega_{1,1}$) according to disk separation for different numbers of disks in the stack. The black dots represent results obtained through numerical simulations from using the BEM [33, 57] for a two disks stack. From this plot we can distinguish a weak coupling region, a strong coupling region, and a transition region in between. The weak coupling region is characterized by a small blueshift of the resonant frequency. It can also be observed that regardless of the number of disks in the stack, the response is similar, indicating that each disk interacts mainly with its nearest neighbors. Due to the large disk separation, surface plasmon hybridization in this regime can be easily described by using a simple dipole model [33]. In the strong coupling region, the resonant frequency reaches a limit dictated by the relation: $\omega_N/\omega_1 = \sqrt{N}$; where ω_N and ω_1 are the resonant frequencies for the high frequency branch and the uncoupled mode, respectively, and N is the number of disks stacked. A similar relation was found in a study of surface plasmon hybridization from the coupling between two graphene sheets at long wavelengths ($\kappa/\kappa_F \ll 1$) [18]. From this relation, it can be inferred that in the

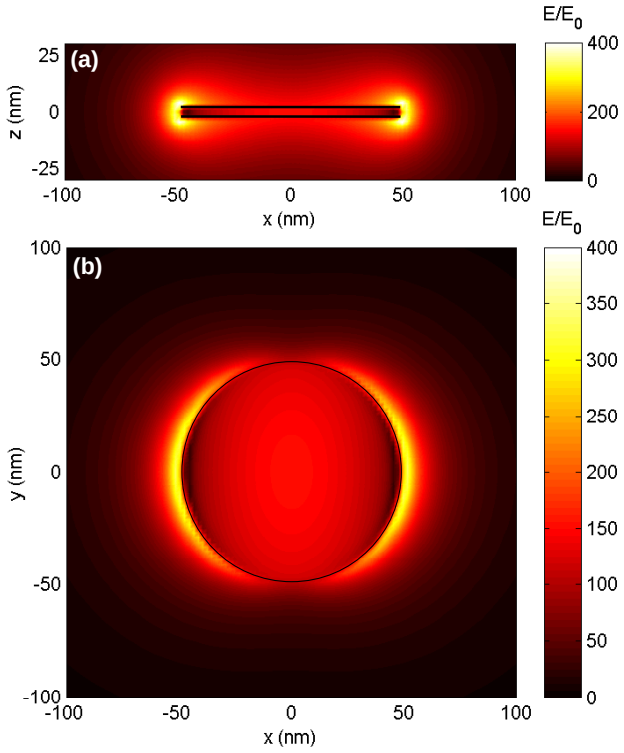

Figure 3.6: E-field distribution for two Graphene disks (D = 100 nm, E_f = 0.6 eV) separated by 5 nm ($R/d = 10$), at the bright mode resonant frequency. (a) Cross plane perpendicular to the disk; (b) Cross plane parallel to the disk, located between both disks.

strong coupling regime, geometric effects are negligible and the response is mainly driven by interaction between the entire surfaces. Finally, it is also observed that disk stacks with a larger number of disks require shorter distances in order to reach the strong coupling limit.

In order to understand the underlying physics in the transition region, we plot the electric field distribution of the bright mode resonant frequency for a two disks stack (Fig. 3.6), by means of numerical simulations using the BEM. We observe that surface charge is mostly distributed at the edge of the disk, meaning that the coupling between disks in this regime is mainly driven by edge plasmon modes. This implies that the geometry of the nanostructure plays a major role in the hybridization process at this regime.

We analyze the strength of the interactions between disks in the case of a 5 disk stack

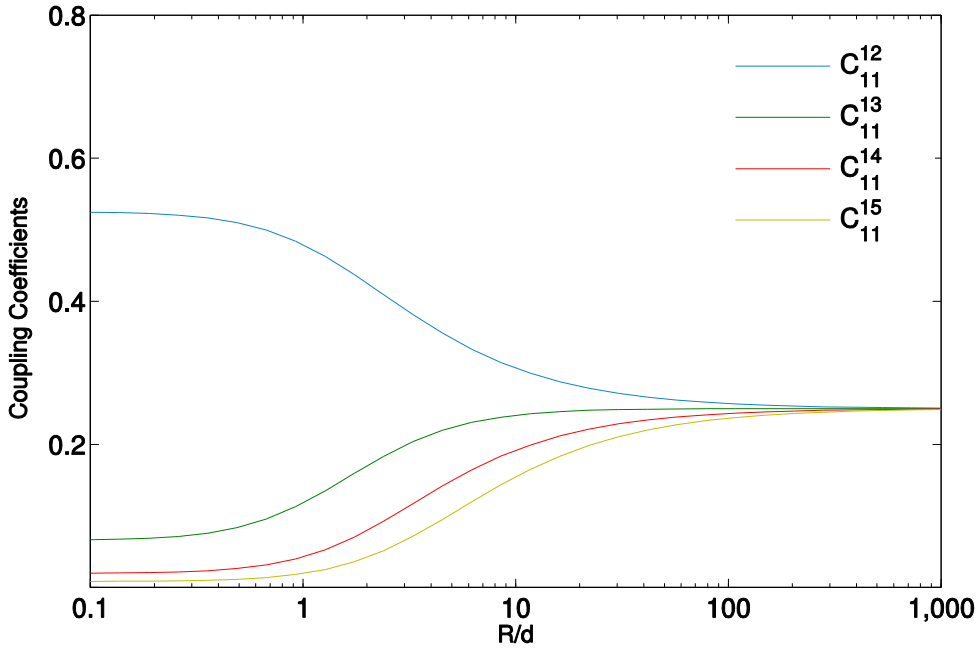

Figure 3.7: First mode coupling coefficients of disk 1 (Fig. 3.1) and its neighbors in a 5 disk stack.

(Fig. 3.7) by using the coupling coefficients from Eqn. (2.48). As mentioned in Section 3.3.1, most of the energy interaction between disks results from coupling between modes of the same order, so we consider only the first mode of the expansion in Eqn. (A.4), which provides a clear picture regarding the interaction between disks. Only the coupling coefficient for disk 1 are shown here (Fig. 3.1). However, due to the symmetry of the structure, these results can also be used to represent the coupling of intermediate disks with their neighbors. We can see from Fig. 3.7 that the weak coupling regime is dominated by the interaction of disks with their nearest neighbors. When the distance between disks falls in the transition region, the interaction with other disks rapidly increases and the interaction with its nearest neighbor decreases. Finally, in the strong coupling regime, the interaction energy between disks is evenly distributed.

As mentioned before, disk stacks with a larger number of disks require shorter distances in order to reach the strong coupling limit. We estimated the maximum normalized distance

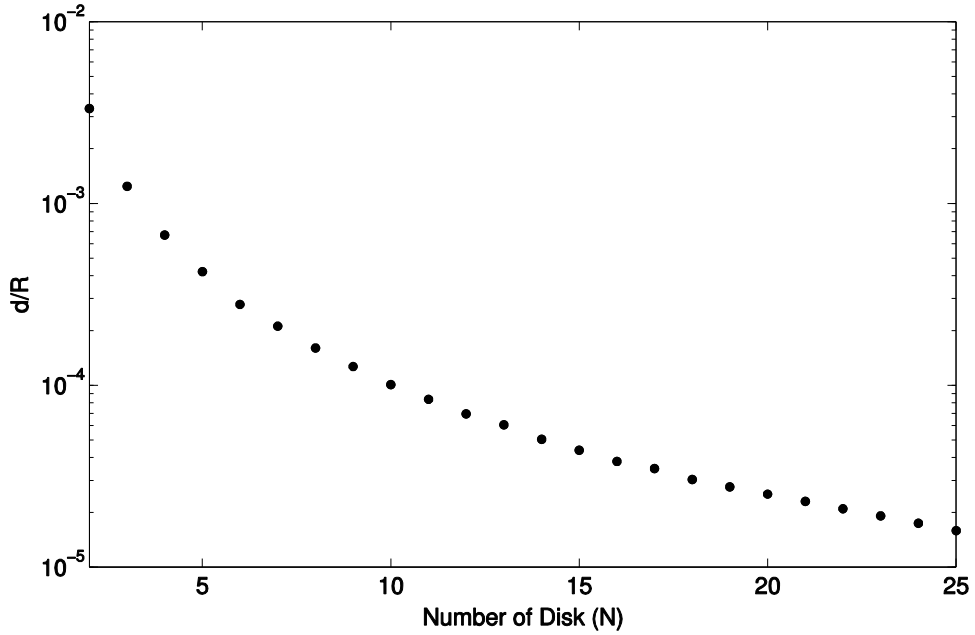

Figure 3.8: Normalized disk separation required to reach 99% of the strong coupling limit according to numbers of disk stacked.

d/R required to reach 99% of the strong coupling limit (Fig. 3.8). From this figure, we can observe that the normalized distance decreases asymptotically as the number of disks increases.

Although there is no upper limit for the blueshift of the plasmons resonant frequency through stacked graphene nanostructures, we can infer from the relation for the strong coupling limit ($\sqrt{N}$), that the frequency blueshift per additional layer dresses at a rate of $1/(2\sqrt{N})$. For disk stacks with more than 25 layers, this means a blueshifting rate of less than 10%, which can be used as an approximation for the upper limit of the blueshift resonant frequency. As an extreme case, we consider a stack of graphene disks of 50 nm in diameter and a doping level of $E_f = 1.0$ eV embedded in a low refractive index material ($n \sim 1$). This limit corresponds to a blueshift of the resonant frequency up to 3.98 eV (or 312 nm in wavelength). However, according to Fig. 3.8, the strong coupling limit for a twenty five disks stack is reached at $d/R \sim 10^{-6}$, which is an unrealistic result in the

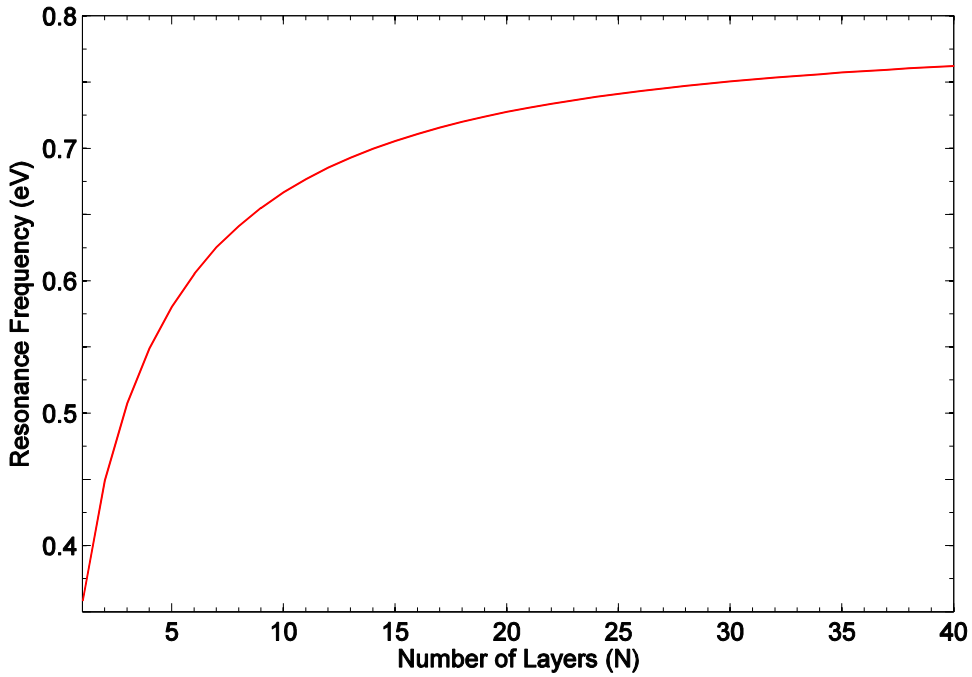

Figure 3.9: Blueshift of the eigenfrequency in graphene disk stacks (D=50 nm, E_f=1.0 eV, d=5 nm) with different numbers of disks.

context of the physics of the problem.

Considering a more realistic scenario, we assume a minimum separation of 5 nm regarding the same characteristics for the graphene disks (D = 50 nm, E_f = 1.0 eV) and analyze the blueshift of the resonant frequency as the number of disk stacked is increased (Fig. 3.9). The results are obtained by ignoring the effect of the relaxation time τ and interband transitions from the expression of the electrical conductivity of graphene [Eqn. (2.18)]. From this figure, we observe that the resonant frequency becomes saturated at a maximum around 0.76 eV (1.63 μm).

In order to understand how plasmon hybridization impacts the effective response of the structure considered before, we analyze the absorption and scattered efficiencies for a stack of 25 disks (Fig. 3.10), which considers a summation of the scattered and absorbed power from each disk in the stack. Our results show a blueshift of the resonant frequency up to 0.69 eV (1.8 μm), represented by the highest peak in the absorption curve. In the

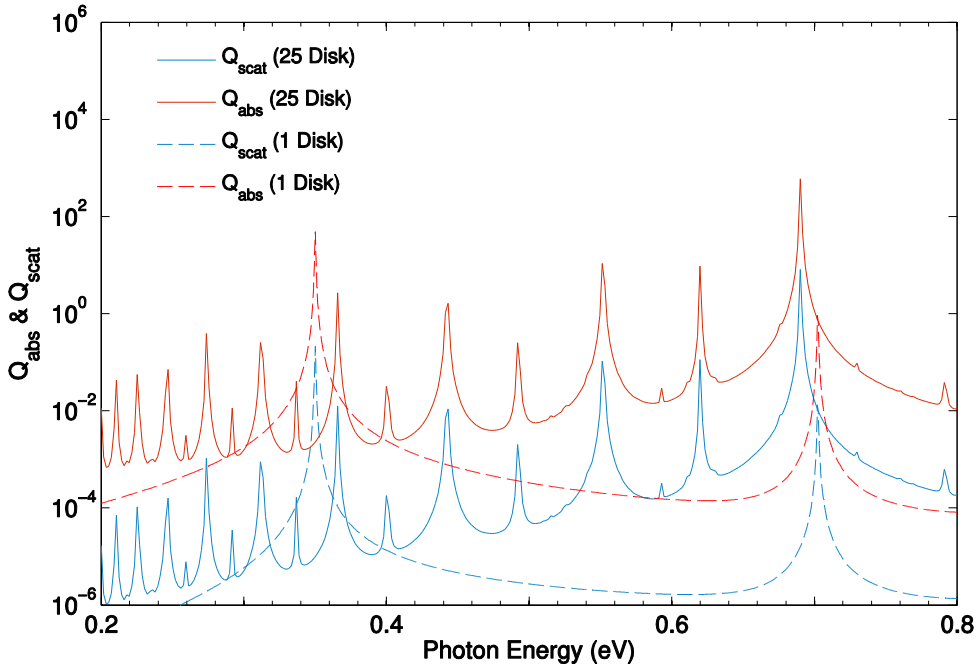

Figure 3.10: Scattering and absorption efficiencies for one graphene disk (D=50 nm, E_f=1.0 eV), and for a twenty five disks stack in which the disks have similar features.

results from Fig. 3.10, we considered all the terms from Eqn. (2.18). This explains the difference with resonant frequency of 0.74 eV for a twenty five disks stack, predicted in the results from Fig. 3.9. Since at this scenario the relative distance ($R/d = 5$) is far from the strong coupling regime ($R/d \sim 10^6$), we also expect to see more than one high frequency mode. Additionally, it can be observed from Fig. 3.10 that the maximum absorption and scattering efficiencies are 12 and 39 times larger than those of a single disk.

3.4 Summary

We have systematically studied the blueshift of the resonant frequency of graphene surface plasmons due to plasmon hybridization using disk stacks. The results reveal that as the distance between disks in an N disk stack is reduced, the original base modes split into N hybrid modes, as a result of surface plasmon hybridization, from which at large values of

R/d only one mode goes to higher frequency. We observe that the hybridization of each uncoupled mode mainly relies on the coupling of modes of the same order. Hybrid mode distribution according to disk separation shows that there is a transition regime between the weak and strong coupling regimes produced by the coupling of edge plasmon modes, where geometry factors are dominant. Hybridization of surface plasmon modes in graphene disk stacks demonstrates a promising way to effectively increase the resonant frequency up to the near-IR spectrum, opening a wide range of applications for graphene plamonics.

Near-Field Radiative Heat Transfer in Graphene Plasmonic Nanodisk Dimers

4.1 Introduction

Radiative heat transfer between two bodies separated by a sub-wavelength gap is called near-field radiation. In this regime, tunneling of evanescent electromagnetic waves leads to heat transfer rates beyond the Planck blackbody limit [19]. The enhancement can be several orders of magnitude in materials that support surface electromagnetic modes, providing that their activation energies are comparable to $k_{\mathrm{B}}T$, where k_{B} is the Boltzmann constant and T is temperature. Thus, polar dielectrics such as SiO_2 and SiC, which support surface phonon-polaritions in the near-infrared part of the spectrum, demonstrate near-field radiation enhancement at room temperature [58, 59]. The near-field thermal radiation response of a bulk material can be modified when it is nanostructured into subwavelength geometries [31, 60, 61]. This technique has been explored in metamaterials for tunable near-field enhancement [62, 63, 64] and in photon-based solid-state thermal devices [65].

Graphene plasmonics has emerged as an alternative platform for strong near-field radiation enhancement [20, 21, 66], with potential application in heat flux spliting [67], thermal plasmonic interconnects [68], and ultrafast radiative cooling [69]. The linear electronic dispersion of graphene leads to a high electron mobility and allows for the induction of free carriers by chemical doping or electrical gating [70]. The resulting plasmons are long-

propagating and strongly-confined, with tunable frequencies from the terahertz towards the mid-infrared part of the spectrum [71]. The near-field thermal radiation properties of nanostructured graphene are largely unexplored. Numerical simulations are computationally expensive [15] and studies have been limited to theoretical approaches, such as the point dipole approximation [67] and perturbation theory [72], which are restricted to large separation gaps.

Herein, we study the near-field thermal radiation properties of surface plasmons in graphene nanodisks dimers. We use a semi-analytical model under the electrostatic approximation, which is suitable when the disk size is smaller than the wavelength of the electromagnetic waves in the surrounding media [50, 51, 52]. Our model extends the theory for a single disk developed by Fetter [45] to include analytical expressions for the Coulombic disk-to-disk interactions. Radiative heat transfer is modeled under a fluctuating surface charge formalism that results in a compact expression that uses the coupling matrices developed in the electrostatic formulation. We are thus able to capture near-field coupling at very small gaps with high accuracy. As the electrostatic theory in based on analytical expressions, we are able to obtain results two orders of magnitude faster than numerical simulations based on the boundary element method (BEM) [33].

The remainder of the paper is organized as follows. The mathematical formulation is described in Section 4.2. The hybridization of surface plasmon modes on disk dimers in co-axial and co-planar configurations is presented in Section 4.3.1. Near-field radiative heat transfer in these configurations is then examined in Sections 4.3.2 and 4.3.3. In Section 4.3.4, the near-field thermal conductance as a function of the orientation between the two disks is studied. The results are summarized in Section 4.4.

4.2 Methods

The optical response of graphene is modeled considering the optical conductivity from Eqn. (2.18). The near-field interaction between two graphene disks is calculated under the electrostatic approximation [41]. The solution is obtained by expanding the surface charge using an orthogonal basis and then considering the boundary conditions at the surface of each disk (see Appendix A.2). Using the fluctuation-dissipation theorem [73], we express the radiative heat conductance between two objects 1 and 2 in terms of the surface charge expansion elements as

$$G_{NF} = \int_0^\infty \Phi_{12}(\omega)\hbar\omega \frac{df_{\mathrm{BE}}}{dT} d\omega. \tag{4.1}$$

Here, f_{BE} is the Bose-Einstein distribution and $\Phi_{12}(\omega)$ is the ensemble averaged flux spectrum (Appendix C.1), which is given by

$$\Phi_{12}(\omega) = \frac{1}{2\pi}\mathrm{Tr}\left[\mathbf{G}^1_{AH}\mathbf{W}^*\mathbf{G}^2_{AH}\mathbf{W}\right]. \tag{4.2}$$

Here, Tr[·] is the trace of the matrix, $\mathbf{W} = 2\left[\mathbf{G}^1 + \mathbf{G}^2 + \mathbf{G}^0\right]^{-1}$ is the electrostatic polarization matrix, $\mathbf{G}^\nu$ and $\mathbf{G}^0$ are interaction matrices in the disk ν ($\nu = 1, 2$) and in the surrounding media [Eqns. (2.47) and (2.48)], and $\mathbf{G}_{AH} = \frac{1}{2}(\mathbf{G} - \mathbf{G}^*)$ is the anti-Hermitian part of $\mathbf{G}$. As shown in Appendix C.2, our theory and numerical simulations using the BEM show good agreement for frequencies bellow 80 THz.

4.3 Results and Discussion

4.3.1 Plasmonic hybrization in graphene disk dimers

Localized surface plasmons in an isolated graphene disk can be classified by radial ($k = 0, 1, ...$) and angular ($l = 0, \pm1, \pm2, ...$) indices [45]. In Fig. 4.1(a), the normalized electric

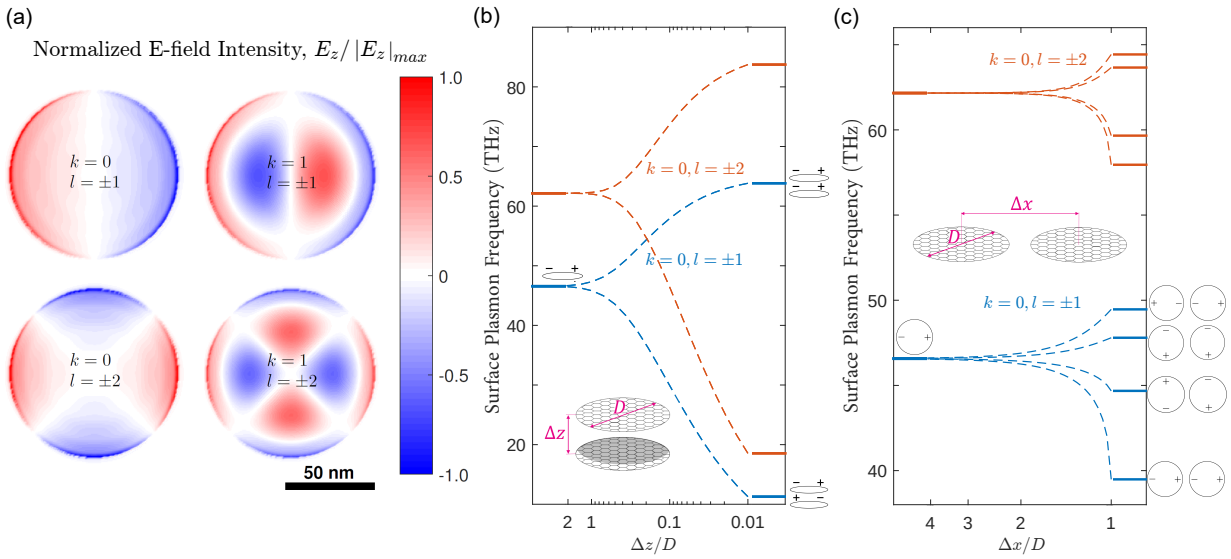

Figure 4.1: (a) Real part of the normalized electric field intensity in the direction perpendicular to the plane of the disk, $E_z/|E_z|_{max}$, showing the surface charge distribution of the localized surface plasmon modes $(k,l) = (0,\pm1), (0,\pm2), (1,\pm1)$, and $(1,\pm2)$ in an isolated graphene disk ($D = 100$ nm, $E_f = 0.6$ eV). Hybrid surface plasmon resonant frequencies of two graphene nanodisks in (b) co-axial and (c) co-planar configurations as a function of the gap between them ($D = 100$ nm, $E_f = 0.6$ eV). A schematic diagram of the charge distribution of the lowest dipole mode, $(k,l) = (0,\pm1)$, is drawn for each case, showing the form of the hybridized plasmon modes. Higher modes adopt similar hybridization behavior.

field in the direction perpendicular to the plane of a disk, $E_z/|E_z|_{max}$, for the $(k,l) = (0,\pm1), (0,\pm2), (1,\pm1)$, and $(1,\pm2)$ modes is shown for a disk diameter, D, of 100 nm and a Fermi level of 0.6 eV. The surface charge for modes with $k = 0$ is mostly distributed along the edge of the disk, while for $k = 1$ (and higher, not shown) the charge is distributed across the surface.

When two disks are separated by a small gap, the overall electromagnetic response differs from the response of an isolated disk. This phenomenon is known as surface plasmon hybridization and is a consequence of the near-field interaction between nanostructures [54, 74]. In the case of two co-axial graphene disks separated by a distance Δz, each fundamental mode hybridizes into a higher frequency mode and a lower frequency mode, as shown in Fig. 4.1(b) for $(k,l) = (0,\pm1)$ and $(0,\pm2)$. The high and low frequency modes

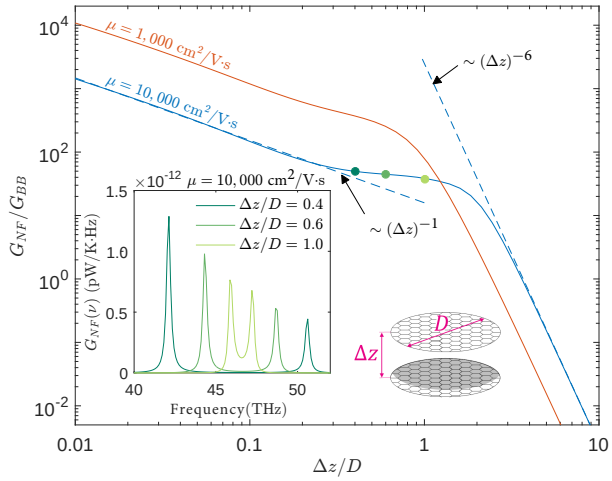

Figure 4.2: Near-field enhancement, G_{NF}/G_{BB}, of two co-axial graphene disks as a function of their separation ($D = 100$ nm, $E_f = 0.6$ eV). (Inset) Spectral radiative thermal conductance, $G_{NF}(\nu)$, showing the hybridization of the fundamental dipole mode $(k, l) = (0, \pm 1)$ at $\Delta z/D = 0.4$, 0.6, and 1.0.

are characterized by the charges on each disk oscillating in-phase and out-of-phase [51, 74]. In the limit of $\Delta z/D \ll 1$, the high frequency mode reaches a maximum given by $\sqrt{2}\omega_0$, where ω_0 is the resonant frequency of the non-hybridized mode [74].

In the case of two co-planar disks with center-to-center disk distance Δx, breaking the axial symmetry produces four hybrid modes for each fundamental mode, as shown in Fig. 4.1(c) for $(k, l) = (0, \pm 1)$ and $(0, \pm 2)$. The two central hybrid modes have the charges oscillating perpendicular to the Δx axis, with similar characteristics as the co-axial hybrid modes. The other two modes have the charges oscillating along the Δx axis. The resonant frequency is highest when the charges oscillate out-of-phase and is lowest when the charges oscillate in-phase. In both the co-axial and co-planar configurations, plasmon hybridization becomes weaker as the gap size increases and vanishes when the distance between the edges is larger than twice the disk diameter.

4.3.2 Near-field radiation in co-axial disk dimers

Surface plasmon hybridization plays a major role in near-field radiative heat transfer between two graphene disks. We evaluate the near-field radiative heat transfer enhancement as G_{NF}/G_{BB}. G_{NF} is the near-field radiative thermal conductance obtained from Eqn. (4.1) and G_{BB} is the blackbody radiative thermal conductance between one side of a graphene disk and a infinite surface [75],

$$G_{BB} = \sigma_{\mathrm{SB}} T^3 \pi D^2, \tag{4.3}$$

where σ_{SB} is the Stefan-Boltzmann constant. Here and in all following calculations, we consider a temperature of 300 K. As a reference, G_{BB} is 4.8×10^{-5} pW/K for a disk of 100 nm diameter.

The near-field enhancement between two suspended co-axial graphene disks of 100 nm diameter and a Fermi level of 0.6 eV is plotted in Fig. 4.2 as a function of their separation. Three regimes can be distinguished: (i) a weak coupling regime at large separations, where the response scales as $(\Delta z)^{-6}$, similar to the interaction between two small dipoles [60], (ii) a strong coupling limit at narrow gaps that scales as $(\Delta z)^{-1}$, and (iii) a transition regime in between. The deviation from the $(\Delta z)^{-6}$ scaling in the strong coupling and transition regimes is a result of the near-field interaction between nanostructures [61] and is indicative of the presence of surface plasmon hybridization. For $\Delta z/D < 3.7$, near-field radiative heat transfer exceeds the blackbody limit, reaching values three orders of magnitude larger when $\Delta z/D = 0.01$.

The role played by hybridization is different in the strong coupling and transition regimes. In the strong coupling regime, the shifts in the hybrid frequencies of each mode have reached their limit, as mentioned in Section 4.3.1. In this regime, the near-field conductance scales as $(\Delta z)^{-1}$, which is the same trend as for near-field radiation between two

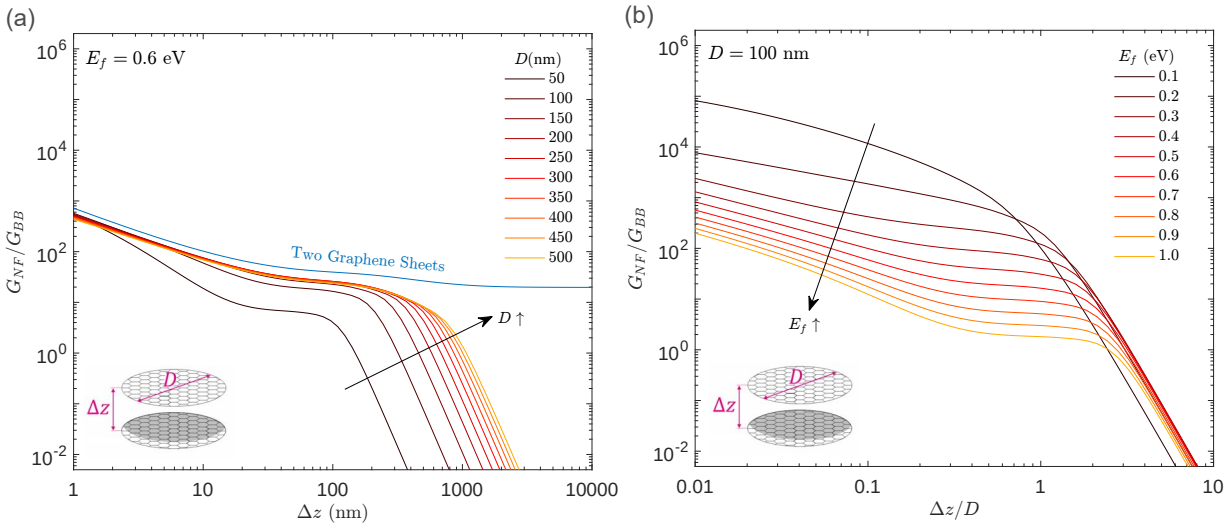

Figure 4.3: (a) Near-field radiation enhancement between two co-axial graphene disks ($E_f = 0.6$ eV), as a function of the distance Δz for disk diameters ranging from 50 to 500 nm. The blue line represents the near field enhancement between two graphene sheets with $E_f = 0.6$ eV. (b) Near-field radiation enhancement between two co-axial graphene disks ($D = 100$ nm) as a function of the distance Δz for Fermi levels ranging from 0.1 to 1.0 eV.

infinite parallel plates [20]. This result indicates that surface mode coupling is dominant. Near-field enhancement in the transition regime, on the other hand, is dominated by the shifting of the resonant frequencies, where interactions from the disk edges play the major role [74]. This phenomenon is observed in the spectral conductance, $G_{NF}(\nu)$, plotted in the inset of Fig. 4.2 for $\Delta z/D = 0.4$, 0.6, and 1.0 for the lowest dipole mode, $(k, l) = (0, \pm 1)$. The peaks are the result of resonances of the hybrid modes and separate as Δz decreases. Higher-order modes present a similar behavior. The shift of the resonant frequencies creates competing effects between a higher thermal activation of the red-shifted hybrid modes and a lower thermal activation of the blue-shifted hybrid modes.

To investigate the effects of optical losses in near-field radiation enhancement, we also considered a mobility of 1,000 cm^2/V·s. The resulting G_{NF}/G_{BB} is plotted in Fig. 4.2. When $\Delta z/D \gg 1$, the near-field enhancement is lower than the case with $\mu = 10,000$ cm^2/V·s. In this regime, the dipole approximation is valid [31, 61] and the near-field ther-

mal conductance between two nanostructures with electric polarizability α and separated by a distance d is [60].

$$G_{NF} \propto \int_0^\infty \frac{[\mathrm{Im}\,(\alpha)]^2}{d^6} \hbar\omega \frac{df_{\mathrm{BE}}}{dT} d\omega.$$

When optical losses increase, the peak in $\mathrm{Im}(\alpha)$ decays, reducing the near-field enhancement. For $\Delta z/D < 1$, the near-field enhancement is larger compared to the results for a mobility of 10,000 $\mathrm{cm}^2/\mathrm{V{\cdot}s}$, indicating that near-field radiation is dominated by optical losses. In the strong coupling regime ($\Delta z/D \ll 1$) near-field enhancement remains larger compared to the result for the larger mobility and the ratio between the two curves is constant. At $\Delta z/D = 0.01$, the near-field conductance exceed the blackbody limit by four orders of magnitude. The behavior in this regime is consistent with the theory of near-field radiation between two semi-infinite surfaces, where higher optical losses favor near-field enhancement [30].

The near-field enhancement between two co-axial graphene disks as a function Δz for disk diameters ranging from 50 to 500 nm is plotted in Fig. 4.3(a). The top line represents the near-field enhancement of two suspended infinite parallel graphene sheets, obtained from the model of Ref. 20. The near-field enhancement increases monotonically with increasing disk diameter in the weak coupling regime. In the strong coupling regime, the near-field enhancement approaches the limit given by the parallel graphene sheets.

In Fig. 4.3(b), the near-field enhancement between two co-axial graphene disks as a function of $\Delta z/D$ is plotted for a Fermi level ranging from 0.1 to 1.0 eV. All the curves show a similar trend in the weak coupling regime, followed by an increased near-field enhancement in the strong coupling regime as the Fermi level decreases. Lowering the Fermi level has two effects: (i) optical losses are increased due to higher rates of intraband and interband transitions, and (ii) the resonant frequencies are red-shifted [14], which increases the contribution from f_{BE}. In the strong coupling regime, the two effects both

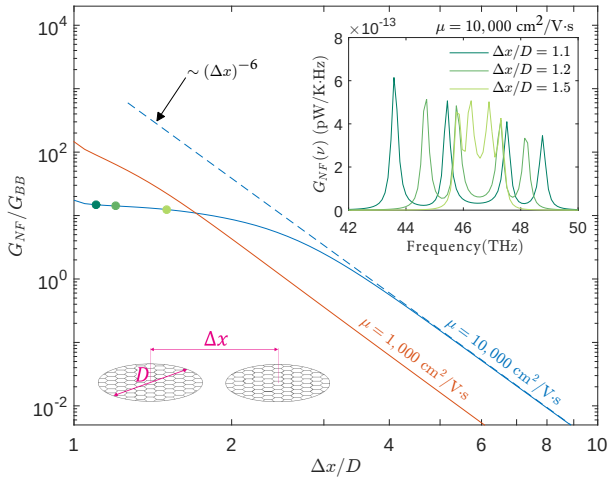

Figure 4.4: Near-field enhancement of two co-planar graphene disks at different gaps ($D = 100$ nm, $E_f = 0.6$ eV). (Inset) Spectral radiative thermal conductance showing the hybridization of the lowest dipole mode $(k, l) = (0, \pm 1)$ at $\Delta x/D = 1.1$, 1.2, and 1.5.

lead to larger near-field enhancement as E_f is reduced. In the weak coupling regime, where optical losses are unfavorable for near-field enhancement, the two effects compete and the curves overlap for different values of E_f. Due to the different role played by intraband transitions in the strong and weak coupling regimes, the curves cross in the transition regime.

4.3.3 Near-field radiation in co-planar disk dimers

We now consider the near-field radiative heat transfer enhancement G_{NF}/G_{BB}, between two co-planar disks. To be consistent with the analysis from Section 4.3.2, G_{BB} is taken to be the blackbody radiation heat conductance between the surface of one disk and an infinite surface [Eqn. (4.3)]. The blackbody radiation heat exchange between the disk's edge and an infinite surface is given by [75]

$$G_{BB}^{edge} = 8\pi\sigma_{SB}T^3Dt, \tag{4.4}$$

where $t = 0.5$ nm is the thickness of a graphene layer, which is based on previous studies on graphene plasmonic nanostructures [14, 76]. We note that studies of thermal transport in graphene often use a thickness of 0.34 nm, which is based on the layer separation in graphite [77, 78]. For a disk diameter of 100 nm, $G_{BB}^{edge} = 1.9 \times 10^{-6}$ pW/K, which is 25 times smaller than G_{BB}.

The near-field enhancement is also strong for two co-planar disks, as plotted in Fig. 4.4, where the thermal conductance exceeds the blackbody limit by a factor of ten when the gap is small. The near-field radiation follows three regimes, similar to the case of two co-axial disks. Given the scaling of the plot, only the weak and transition regimes can be distinguished. In the inset, the spectral data for $(k, l) = (0, \pm 1)$ for $\Delta x/D = 1.1$, 1.2, and 1.5 show that each fundamental localized surface plasmon mode is hybridized into four modes due to the breaking of axial symmetry, as explained by Fig. 4.1(c). At large separations, the thermal conductance reaches the weak coupling regime, where it scales as $(\Delta x)^{-6}$. Similar to the co-axial disk configuration, lower quality graphene shows a larger near-field enhancement only when $\Delta x/D < 2$.

4.3.4 Near-field radiation in disk dimers as a function of angle

As seen in Figs. 4.2 and 4.4, near-field interactions are conditioned by the distance between the two disks and their relative orientation. To further explore the orientation effect, in Fig. 4.5(a) we plot the near-field enhancement as a function of the orientation angle, θ, for center-to-center separations, Δr, of 105 nm, 120 nm, and 150 nm. As in Figs. 4.2 and 4.4, $D = 100$ nm and $E_f = 0.6$ eV. By changing the angle between the two disks, a minimum is observed at $\theta \approx 45°$ as they transition between the co-planar and co-axial orientations. The spectral heat conductance at a separation of 120 nm is plotted in Fig. 4.5(b) for the lowest dipole mode $(k, l) = (0, \pm 1)$ for $0° \leq \theta \leq 90°$, revealing the role played by surface plasmon

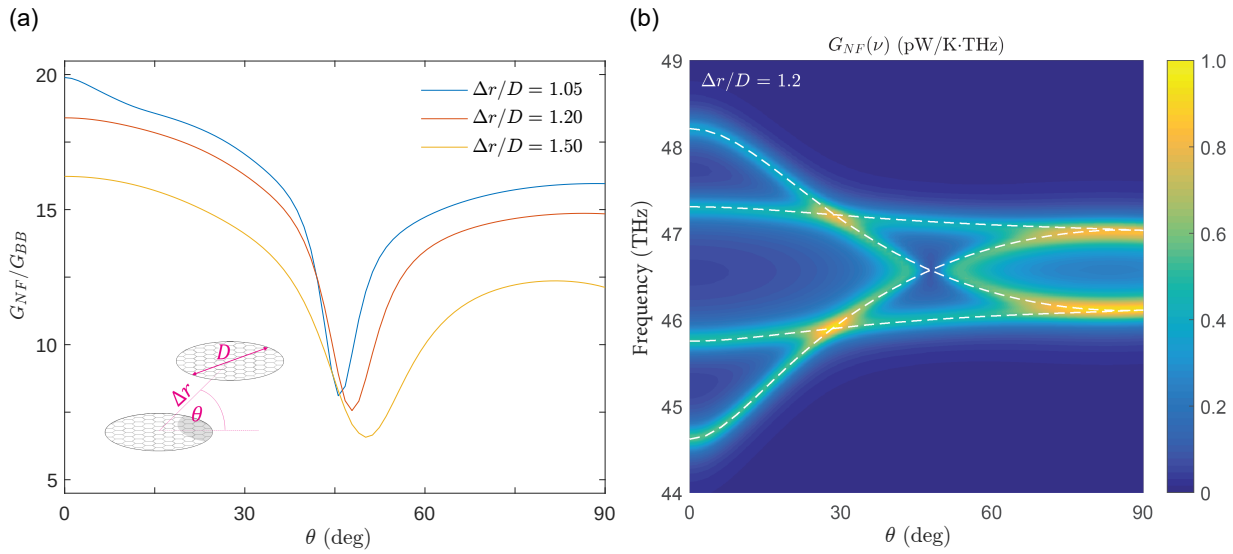

Figure 4.5: Near-field enhancement, G_{NF}/G_{BB}, between two graphene disks as a function of their orientation for center-to-center separations, Δr, of 105, 120, and 150 nm ($D = 100$ nm, $E_f = 0.6$ eV). (b) Spectral radiative heat conductance at $\Delta r = 120$ nm showing the hybridization of the fundamental diple mode, $(k, l) = (0, \pm 1)$, as a function of the angle.

hybridization. The hybridized resonant frequencies transition from four modes at $\theta = 0°$ to two two-fold degenerate modes at $\theta = 90°$. At $\theta = 48°$, two of the hybrid modes have the same resonant frequency, producing destructive interference and reducing the thermal conductance. This angle corresponds to the minimum in the near-field enhancement in Fig. 4.5(a).

4.4 Summary

We developed an electrostatic semi-analytical approach that is a powerful tool for fast modeling of near-field radiation in graphene nanostructures. Its application to two graphene disks demonstrates that near-field coupling can lead to an enhancement of radiative heat transfer beyond the blackbody limit for co-planar and co-axial configurations, as shown in Figs. 4.2 and 4.4. Three regimes were observed for near-field enhancement as a function of disk separation: a transition regime and a strong coupling regime for small separations,

which are dominated by surface plasmon hybridization, and a weak-coupling regime for larger separations that is dominated by dipole interactions. Larger optical losses increase near-field thermal conductance in the transition and strong-coupling regimes, while they are detrimental in the weak-coupling regime. The result for co-planar disks is particularly interesting, as classical theories for far-field radiation predict negligible heat transfer rates due to the small view factor. Varying the relative orientation between the disks can induce destructive interference between hybrid modes, which reduces the radiative heat transfer rate (Fig. 4.5).

Our findings demonstrate the potential of graphene nanostructures for tunable near-field radiation enhancement, paving the way for the development of graphene metamaterials and photon-based thermal solid-state devices. Co-planar nanodisk waveguides in particular have potential for tunable plasmonic heat transport. This concept is explored in Chapter 5.

Plasmonic Thermal Transport in Graphene Nanodisk Waveguides.

5.1 Introduction

Thermal activation of electromagnetic (EM) surface modes, such as surface plasmon-polaritons or surface phonon-polaritions, can lead to a thermal radiation flux at subwavelength gaps that is orders of magnitude larger than the Planck blackbody limit [19]. The strong near-field coupling in materials that support surface polaritons suggests a new form of thermal transport mediated by guided EM modes [79, 80, 81, 82]. While optical losses are essential for enhanced near-field radiative heat transfer [83, 84], they limit mode propagation in waveguides. As such, the thermal conductivities of polaritonic waveguides have been predicted to be small, with maximum values of 1×10^{-8} W/m-K for surface plasmons in a copper nanosphere array [79] and 0.04 W/m-K for surface phonon-polaritions in a silicon carbide nanospheroid array [80].

The emergence of graphene as a platform for terahertz surface plamons [14] has opened up new opportunities for radiative heat transfer [20]. The linear electronic dispersion of graphene gives rise to an extremely large intrinsic electron mobility and tunable control over induced charge carriers by chemical doping or electrical gating [70]. As a result, graphene can support thermally-activated, tunable, long-propagating [76, 85], and strongly-confined surface plasmons [71], leading to strong [20, 21, 66] and ultrafast [69] near-field radiative heat transfer. This behavior suggests the potential of graphene waveguides for efficient plasmonic thermal transport.

Herein, we study the thermal transport properties of surface plasmons in one-dimensional co-planar graphene nanodisk arrays. We use a semi-analytical model under the electrostatic approximation [83] that can accurately predict near-field interactions for disks with sizes smaller than the wavelength of the EM waves in the surrounding media [41]. From this theory, the band structure of guided modes is extracted and then used to predict the thermal properties in a diffusive regime. Unlike other studies that are based on dipole-dipole interactions [67, 76, 86] or perturbation theory [72], our model is not restricted by the separation between disks because the calculations are based on analytical expressions for the interactions between all plasmonic modes.

The remainder of the paper is organized as follows. In Section 5.2, the mathematical formulations for the optical conductivity of graphene and for predicting the plasmonic band structure are described. In Section 5.3, the dispersion relations and decay lengths of surface plasmons in graphene nanodisk arrays are analyzed and a non-dimensional model is proposed. In Section 5.4, the potential of graphene nanodisk waveguides for surface plasmon-enhanced thermal transport is assessed by predicting their heat capacities, thermal conductivities, and thermal diffusivities in a variety of configurations. The conclusions are presented in Section 5.5.

5.2 Methods

The optical response of graphene is modeled considering the optical conductivity from Eqn. (2.18).

The transport properties of guided surface plasmon modes in a periodic one-dimensional co-planar disk array are obtained from an eigenvalue problem that is described in **??**. To account for the effects of the substrate in supported disk arrays, we consider the disks to be between two regions with dielectric constants ε_1 (above the array) and ε_2 (the sub-

strate). Unless noted, $\varepsilon_1 = 1$, which corresponds to vacuum. The formulation considers the Coulombic (i.e., electrostatic) interactions between disks using the semi-analytical model from Appendix A.2 [Eqn. (A.13)]. The solution is given by a set of complex eigenfrequencies, $\tilde{\omega}_p$, whose real part, ω_p, defines the dispersion relation and whose imaginary part represents the mode's temporal losses through the relation $\tau_p = [2\mathrm{Im}(\tilde{\omega}_p)]^{-1}$. At low temperatures ($E_f/k_\mathrm{B}T \gg 1$) and surface plasmon energies, $\hbar\omega_p$, satisfying the condition $\hbar\omega_p/E_f < 1$, the second term on the right-hand side of Eqn. (2.18) becomes negligible and $\tau_p = \tau$.

5.3 Plasmonic properties

5.3.1 Dispersion relation and decay length

The dispersion relation of a one-dimensional array of highly-doped graphene ($E_f = 1.0$ eV) disks (100 nm diameter, D, and 110 nm center-to-center distance, Δx) over a substrate with $\varepsilon_2 = 2.4$ are plotted in Fig. 5.1(a). This Fermi level was chosen to show the upper limit of the wave-guiding properties in terms of doping by electrical gating. The dielectric constant of the substrate represents the average value for SiO_2 for the frequency spectrum considered in Fig. 5.1(a) [87]. The plasmonic bands can be classified according to the radial ($k = 0, 1, ...$) and angular ($l = 0, \pm1, \pm2, ...$) indices of the localized surface plasmons in a single graphene disk [83]. Here, only the modes corresponding to the lowest radial mode ($k = 0$) are presented. Modes with $k > 0$ have group velocities close to zero and their contributions to thermal transport can be ignored, as revealed by analysis of the frequency-dependent thermal conductivity accumulation (see Section 5.4.1). For each angular mode with $l > 0$, longitudinal and transverse polarizations are observed, where the modes on each disk oscillate parallel and perpendicular to the direction of propagation.

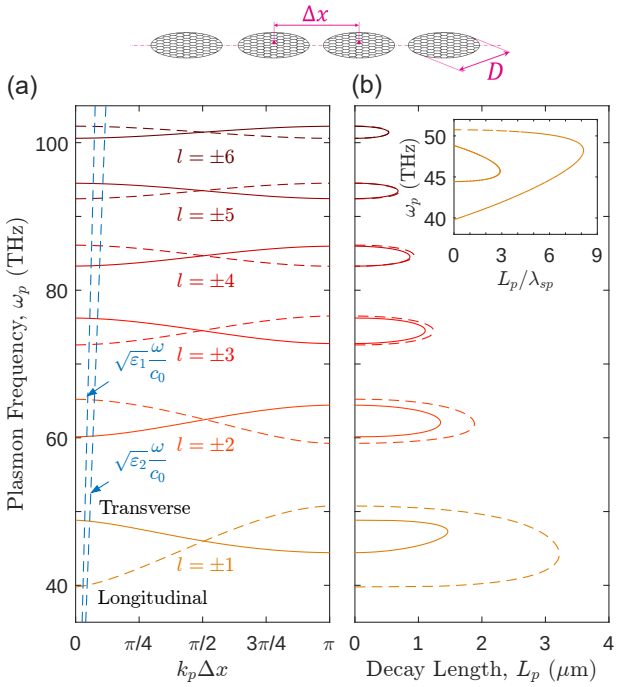

Figure 5.1: (a) Dispersion relation and (b) decay lengths of the lowest radial modes ($k = 0$) for a one-dimensional periodic co-planar array of graphene disks ($\Delta x = 110$ nm, $D = 100$ nm, $E_f = 1.0$ eV). The dispersion for EM-waves propagating in vacuum ($\varepsilon_1 = 1.0$) and in a dielectric substrate ($\varepsilon_2 = 2.4$) are included in (a) as a reference, where c_0 is the speed of light in vacuum. The inset of (b) shows the decay length in terms of number of cycles completed, L_p/λ_{sp}, for the fundamental dipole modes, $(k, l) = (0, \pm 1)$.

The dispersion relations of EM-waves in vacuum and in the dielectric substrate are also plotted. These linear bands show the large degree of confinement of the fundamental dipole modes $(k, l) = (0, \pm 1)$, as their dispersion lies mostly outside of the light cone.

The $1/e$ decay lengths, L_p, are obtained from

$$L_p = \tau_p v_g, \tag{5.1}$$

where $v_g = \frac{d\omega_p}{dk_p}$ is the group velocity of the surface plasmon and k_p is its wavenumber. As our model is based on the electrostatic approximation, radiation damping effects, *i.e.* surface plasmon decay through retardation of EM waves and radiation reaction, are ignored. Thus, the mechanisms of plasmon decay are directly related to the optical losses dictated

by intraband and interband transitions from Eqn. (2.17).

Using Eqn. (5.1), the decay lengths of the modes from Fig. 5.1(a) are plotted in Fig. 5.1(b). The longitudinal fundamental dipole modes have the largest decay lengths, with a maximum of 3.1 μm. The transverse fundamental dipole modes have a maximum decay length of 1.2 μm. Surface plasmon modes with $l > 1$ show smaller decay lengths as the magnitude of l increases due to a reduction in their group velocities. The number of wave-cycles completed, L_p/λ_p, for $l = \pm 1$, where $\lambda_p = 2\pi/k_p$ is the surface plasmon wavelength, is plotted in the inset to Fig. 5.1(b). The longitudinal and transverse modes reach a maximum of eight and three cycles before decaying.

5.3.2 Effect of radiation damping on the plasmonic band structure

Radiation damping, *i.e*, retardation of EM waves and radiation reaction, is neglected in our electrostatic model [Eqn. (D.1)]. Its effect is evaluated in this section by comparing the frequencies and decay lengths of the fundamental dipole modes $[(k, l) = (0, \pm 1)]$ predicted from our model with those obtained when the full dipole-dipole interactions are included. Higher-order modes cannot couple to light in the free space and are thus unaffected by radiation damping. The full dipole-dipole interaction model is based on the exact solution of the EM fields emitted by an electric dipole [D.2]. This approach has been used to represent the interactions between graphene nanodisks when $\Delta x/D > 1.5$ [88, 89]. To study arrays with $\Delta x/D < 1.5$, we built a model [Eqn. (D.9)] that considers electrostatic interactions of a disk with its nearest-neighbor and full dipole-dipole interactions with the other disks in the array. This added level of detail provides better accuracy in predicting the plasmonic band structure. In comparison with our electrostatic model, inclusion of the full dipole-dipole interactions results in a non-linear eigenvalue problem that does not

allow for the advantages of non-dimensionalization, which is proper from the electrostatic approach [54]. This means that a particular calculation is needed for every disk array configuration, while the electrostatic model allows to extract multiple band structures from a single non-dimensional dispersion (see Section 5.3.3). This is particularly relevant when multiple plasmonic band structures are required, as in the determination of the plasmonic thermal properties discussed in Section 5.4.

The surface plasmon frequencies and decay lengths of the longitudinal and transverse fundamental dipole modes obtained from the full dipole-dipole interaction and from our electrostatic model are plotted for arrays with disks of diameter of 100 nm in Fig. 5.2(a) and 500 nm in Fig. 5.2(b). In these plots, $E_f = 1.0$ eV, $\Delta x/D = 1.1$. We consider the case of suspended disk arrays ($\varepsilon_1 = \varepsilon_2 = 1$) as the full dipole-dipole interaction model is constructed on the basis of dipole arrays lying in a homogeneous host. The frequencies predicted for a disk diameter of 100 nm show no difference. The decay lengths show a deviation of at most 4.7%, which is a consequence of changes in the mode lifetime, as shown in Fig. D.2(a), which is a result of the radiation damping of modes bellow the lightline [90, 91]. For a disk diameter of 500 nm, a deviation of at most 0.4% is observed in the frequencies. The difference is characterized by a dip in the dipole-dipole prediction at the crossing between the light line and the transverse polarization band. It is a result of the coupling of dipole modes with light traveling in the free space due a lower degree of confinement [90]. The coupling with light in the free space also affects the mode lifetimes, as shown in Fig. D.2(b). As a result of these changes in the frequencies and lifetimes, the decay lengths predicted with the electrostatic model show a larger discrepancy than for $D = 100$ nm.

The average relative error between both models for disk arrays ($E_f = 1.0$ eV and $\varepsilon_1 = \varepsilon_2 = 1$) with diameters of 100, 200, 500, and 1000 nm and separations $\Delta x/D$ of 1.1,

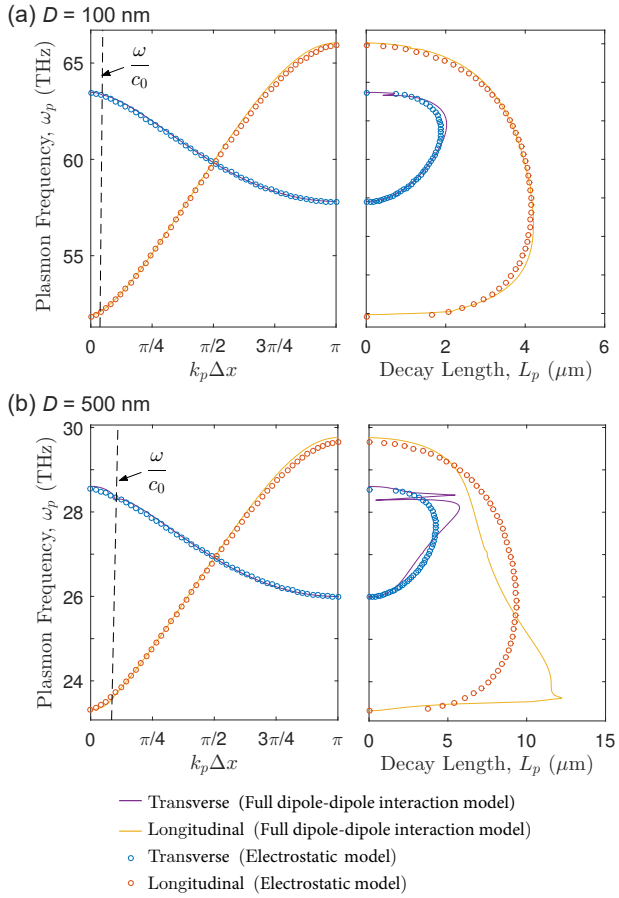

Figure 5.2: Surface plasmon dispersion relations and decay lengths of the fundamental dipole modes $[(k, l) = (0, \pm 1)]$ for an array of graphene nanodisks in vacuum with $\Delta x/D = 1.1$, $E_f = 1.0$ eV, $\varepsilon_1 = \varepsilon_2 = 1$, and (a) $D = 100$ nm, (b) $D = 500$ nm. The lines correspond to the full dipole-dipole interaction model from Eq. (S18) and the open circles correspond to the electrostatic model from Eqn. (D.1).

1.6 and 1.9 are provided in Table 5.1. For disk diameters of 100 and 200 nm, the deviation is less than 1% in the frequencies and less than 12% in the decay lengths. For the larger disk diameters, the frequencies remain within 1% agreement, but the decay lengths deviate by up to 23% ($D = 500$ nm) and 68% ($D = 1000$ nm). The deviation is the result of the lower degree of confinement as the disk size increases. Our electrostatic model is thus an efficient and accurate way to predict the plasmonic properties in disk arrays with diameters smaller than 200 nm. At larger disks diameters, the model continues to offers accurate predictions of the frequencies but loses accuracy for the decay lengths. The suitability of

Table 5.1: Average relative error in % of surface plasmon frequencies and decay lengths between the full dipole-dipole interaction model [Eq. (S18)] and the electrostatic model [Eqn. (D.1)]. $E_f = 1.0$ eV and $\varepsilon_1 = \varepsilon_2 = 1$.

	Frequency				Decay Length			
D (nm)	100	200	500	1000	100	200	500	1000
$\Delta x/D$	Transverse Modes							
1.1	0.09	0.12	0.14	0.21	4.7	7.9	19	42
1.6	0.03	0.04	0.07	0.14	5.7	8.0	16	45
1.9	0.02	0.03	0.06	0.14	6.7	12	22	68
$\Delta x/D$	Longitudinal Modes							
1.1	0.29	0.32	0.35	0.36	3.9	6.2	17	39
1.6	0.05	0.07	0.11	0.16	4.9	7.9	19	37
1.9	0.03	0.05	0.08	0.11	5.7	9.4	23	42

the electrostatic model for thermal conductivity prediction is investigated in Sec. 5.4.1.

5.3.3 Non-dimensionalization

Under the electrostatic approximation, the plasmonic eigenmodes of coupled nanostructures can be directly extracted from a non-dimensional Hermitian eigenvalue problem [54]. Inspection of Eqn. (D.1) shows that in the case of graphene nanodisk arrays, the non-dimensional eigenfrequency Ω_p is strictly dependent on the non-dimensional parameters $k_p\Delta x$ and $\Delta x/D$, where Ω_p is given by

$$\Omega_p = \sqrt{\frac{i\tilde{\omega}_p\varepsilon_0\varepsilon_h D}{2\sigma}}. \tag{5.2}$$

Here, ε_0 is the permittivity in vacuum and $\varepsilon_h = (\varepsilon_1+\varepsilon_2)/2$ is the average dielectric constant. This transformation allows us to reduce the number of independent variables that define the plasmon frequency, *i.e.*, $\omega_p = f(k_p, \Delta x, D, \varepsilon_h, \sigma)$. For a given $\Delta x/D$, multiple dispersion relations can be extracted from a single Ω_p dispersion. The dispersion relation given by Ω_p can be fitted using a electrostatic dipole-dipole interaction model (see Appendix **??**).

At low temperatures ($k_BT/E_f \ll 1$), σ is given by Eqn. (2.18). Assuming only intraband

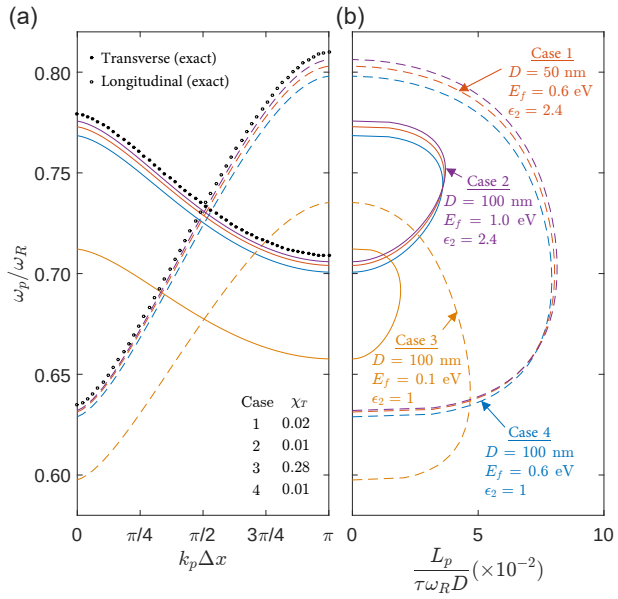

Figure 5.3: Non-dimensional (a) dispersion and (b) decay lengths for an array of co-planar graphene disks ($\Delta x/D = 1.1$) for the fundamental dipole modes, $(k, l) = (0, \pm 1)$, considering different disk diameters and carrier concentrations. The value of $\chi_T \equiv \hbar\omega_R k_B T/E_f^2$ is provided in the lower right-hand corner in (a) for each case.

transitions (*i.e.*, $\hbar\omega_p/E_f < 1$), Eqn. (5.2) can be simplified to

$$\Omega_p \approx \omega_p/\omega_R, \tag{5.3}$$

where

$$\omega_R = \sqrt{\frac{E_f e^2}{\pi\hbar^2\varepsilon_0\varepsilon_h D}} \tag{5.4}$$

is the characteristic plasmon frequency. With this result, a non-dimensional expression for the decay length is given by

$$\frac{L_p}{\tau\omega_R D} = \frac{\Delta x}{D}\frac{d\Omega_p}{d(k_p\Delta x)}, \tag{5.5}$$

where we replace τ_p by τ as only intraband transitions are present (see Section 5.2).

The characteristic plasmon frequency provides a reference of the frequency range of the plasmonic band structure. For example, for the conditions of the dispersion relation

plotted in Fig. 5.1(a), $\omega_R = 44$ THz, which is within the frequency range of the lowest bands. Based on the conditions used to derive Eqns. (5.3) and (5.5) (*i.e.*, low temperature and only intraband transitions), a criterion to evaluate the validity of the proposed scaling relations is $\chi_T \equiv \hbar\omega_R k_B T/E_f^2 \ll 1$.

The non-dimensional dispersion for $\Delta x/D = 1.1$ for the transverse and longitudinal fundamental dipole modes is plotted in Fig. 5.3(a) for a selection of E_f, D, and ϵ_2. The results are compared with the exact solution from Eqn. (5.2), which is plotted as black circles. The simplified expression for the frequency remains valid when $\hbar\omega_R k_B T/E_f^2 < 0.02$ (less than 1% relative error). For the case of $D = 100$ nm, $E_f = 0.1$ eV, and $\epsilon_2 = 1$ (case 3), which has $\chi_T = 0.28$, a deviation of up to 8% is present.

The non-dimensional decay lengths corresponding to the dispersion curves from Fig. 5.3(a) are plotted in Fig. 5.3(b). There is no exact solution to compare to for the decay length, as Eqn. (5.5) was obtained for the specific conditions of low temperature and only intraband transitions. The three curves that satisfy the criterion $\chi_T \ll 1$ fall within a range of 3%. The case 3 curve, which has $\chi_T = 0.28$, is redshifted by 8% and reduced in magnitude by 42% with respect to the others.

5.4 Guided Surface Plasmons as Heat Carriers

5.4.1 Heat capacity and thermal conductivity of disk arrays

We now evaluate the thermal transport properties of surface plasmons in one-dimensional co-planar graphene disk arrays using dispersion relations and decay lengths as obtained in Section 5.3. The results were obtained using the scaling rules from Eqns. (5.3) and (5.5) at a temperature of 300 K.

The volumetric heat capacity (J/m^3-K) due to surface plasmons in the disk array, C_t,

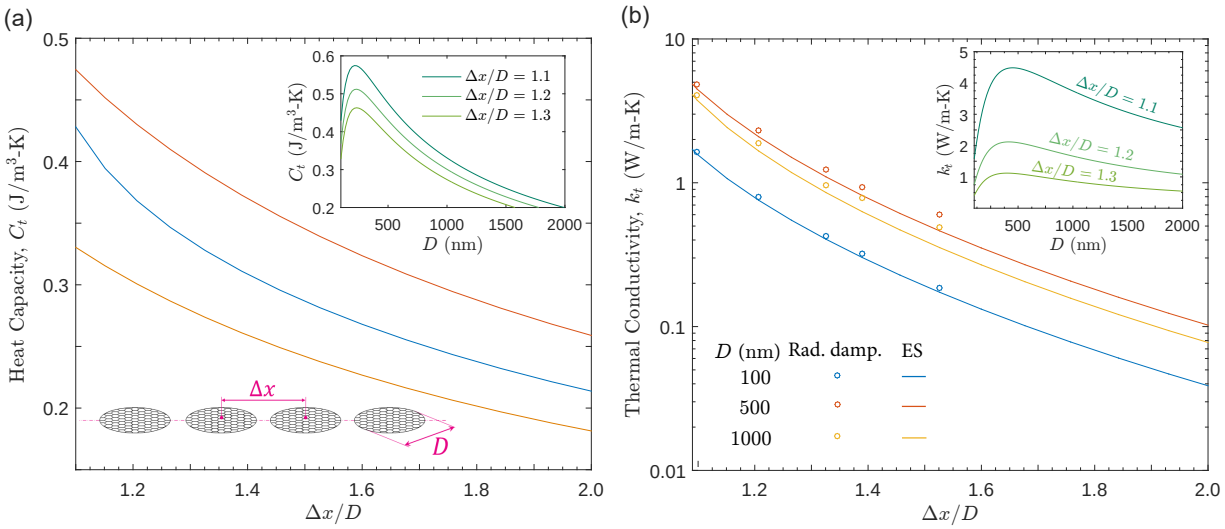

Figure 5.4: (a) Heat capacity and (b) thermal conductivity of co-planar disk arrays for different diameters and separations obtained from the electrostatic (ES) model. The data in open circles in (b) correspond to thermal conductivity predictions that consider radiation damping effects (Rad. damp.). $T = 300$ K, $E_f = 1.0$ eV, and $\varepsilon_2 = 2.4$ for all calculations.

is calculated from [92].

$$C_t = \frac{2}{A}\sum_{l,P}\int \hbar\omega_p^{l,P} D_p\left(\omega_p^{l,P}\right)\frac{df_{\mathrm{BE}}}{dT}d\omega_p^{l,P}, \tag{5.6}$$

where A is the disk's cross sectional area ($A = Dt$, where t is the thickness of a graphene layer), $D_p(\omega_p) = \frac{1}{\pi}\frac{dk_p}{d\omega_p}$ is the plasmonic density of states per unit of length, and $f_{\mathrm{BE}} = 1/[\exp(\hbar\omega_p/k_{\mathrm{B}}T) - 1]$ is the Bose-Einstein distribution. A graphene thickness of 0.5 nm is chosen based on previous studies of graphene plasmonic nanostructures [14, 76]. We note that studies of thermal transport in graphene often use a thickness of 0.34 nm, which is based on the layer separation in graphite [77, 78].

In Fig. 5.4(a), the heat capacity is plotted for doped graphene disk arrays ($E_f = 1.0$ eV) on a dielectric substrate ($\varepsilon_2 = 2.4$) as a function of the separation between disks $\Delta x/D$ at disk diameters of 100, 500, and 1000 nm. There is a monotonic increase of the heat capacity as Δx is reduced. This increase is a result of stronger near-field coupling, which

increases the number of thermally-activated modes. The heat capacities are $O(0.1$ J/m^3-K), small in comparison to the phonon heat capacity of a continuous grapehene sheet of 1.6×10^6 J/m^3-K [93].

Of these three diameters, the heat capacity is the largest for 500 nm throughout the $\Delta x/D$ domain, which is a result of competing effects. This phenomenon is demonstrated in the inset of Fig. 5.4(a), where the heat capacity is plotted as a function of D for $\Delta x/D = 1.1$, 1.2, and 1.3. As the diameter is reduced, the heat capacity in all three curves increases until reaching a maximum at $D = 234$ nm. To elucidate the origin of the maximum, Eqns. (5.3) and (5.5) are used to obtain a set of scaling rules for the parameters in Eqn. (5.6). For example, the density of states can be rewritten in the form

$$D_p(\omega_p) = \frac{1}{\pi D \omega_R} \left(\frac{D}{\Delta x} \right) \frac{d(k_p \Delta x)}{d\Omega_p}.$$

Here, the terms $\frac{D}{\Delta x}$ and $\frac{d(k_p \Delta x)}{d\Omega_p}$ are invariant under changes to D when $\Delta x/D$ is fixed, while the term $\frac{1}{\pi D \omega_R}$ scales as $D^{-1/2}$. Therefore, the density of states scales with the diameter as $D^{-1/2}$. From the same analysis, we find that ω_p scales as $D^{-1/2}$. Thus, as the diameter increases, the frequency spectrum is redshifted, increasing the contribution from df_{BE}/dT. This effect competes with the overall reduction in $\hbar \omega_p D_p(\omega_p)\, d\omega_p$, which scales as $D^{-3/2}$.

Thermal transport is diffusive for disk arrays longer than than the maximum surface plasmon decay length. In such cases, the array thermal conductivity, k_t, can be calculated from [79]

$$k_t = \frac{2}{A} \sum_{l,P} \int C(\omega_p^{l,P}) L_p^{l,P} v_g^{l,P} d\omega_p^{l,P}, \tag{5.7}$$

where $C(\omega) = \hbar \omega D_p(\omega) \frac{df_0}{dT}$ is the frequency-dependent heat capacity [see Eqn. (5.6)]. In writing Eqn. (5.7), we have taken the decay length to be the surface plasmon mean free path, as it represents the distance traveled by a plasmon before its energy dissipates due

to interband and intraband transitions (and radiation damping effects, when considered).

The thermal conductivities of the same arrays considered in Fig. 5.4(a) are plotted in Fig. 5.4(b) and are of $O(1$ W/m-K). At $\Delta x/D = 1.1$, the thermal conductivities for all three cases are two and eight orders of magnitude larger than previous predictions of 0.04 W/m-K for suspended SiO_2 nanospheroid arrays at a temperature of 500 K [80] and 1×10^{-8} W/m-K for copper nanosphere arrays at a temperature of 900 K [79]. For a given diameter, the thermal conductivity decays monotonically with increasing $\Delta x/D$, which is a result of the weaker near-field coupling between disks. For a given $\Delta x/D$, the thermal conductivity for an array with disks of diameter 500 nm is always larger than the other two cases, *i.e.*, thermal conductivity does not change monotonically with the diameter.

In the inset of Fig. 5.4(b), the thermal conductivity is plotted for $\Delta x/D = 1.1$, 1.2, and 1.3 as a function of the disk diameter. Similar to the heat capacity, there is a maximum due to the presence of competing effects. From Eqns. (5.3) and (5.5), L_p and v_g scale as $D^{1/2}$. Thus, the increased mode population for larger disks, represented by a larger contribution from df_{BE}/dT, competes with the decay in the overall contribution from $\hbar\omega_p D_p(\omega_p) L_p v_g d\omega_p$, which scales as $D^{-1/2}$.

The data plotted as open circles in Fig. 5.4(b) correspond to thermal conductivities predicted from the dispersion relations extracted form Eq. (S18), which includes radiation damping. For that calculation, we considered light traveling in a host material with a dielectric constant $\varepsilon_h = (\epsilon_1 + \epsilon_2)/2 = 1.7$. The two sets of results follow the same trend and our electrostatic model becomes more accurate as the gap between disks and the disk diameter decrease. The discrepancy is due to radiation damping effects on the plasmonic properties of the fundamental dipole modes, as discussed in Section 5.3.2. For a disk diameter of 100 nm, the error ranges from 5.4% at $\Delta x/D = 1.1$ to 8.0% at $\Delta x/D = 1.5$. For disk diameters of 500 and 1000 nm, the error ranges from 8.0 to 23% and 9.0 to 28%.

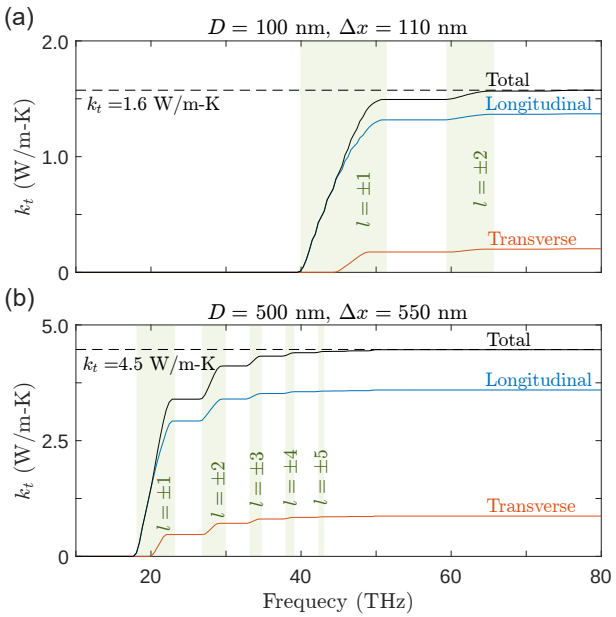

Figure 5.5: Frequency-dependent thermal conductivity accumulation, $k_t(\omega)$, for $\Delta x/D = 1.1$, $E_f = 1.0$ eV, $\varepsilon_2 = 2.4$, and (a) $D = 100$ nm and (b) $D = 500$ nm. The contribution from each band is labeled by its angular index l.

The errors are smaller than those for the decay lenghts provided in Table 5.1 because higher order modes, which are accurately predicted by the electrostatic model, contribute to thermal transport.

We analyze mode-dependent contributions to the thermal conductivity by evaluating the frequency-dependent thermal conductivity accumulation,

$$k_t(\omega) = \frac{2}{A}\int_0^{\omega}\sum_{l,P} C(\omega_p^{l,P}) L_p^{l,P} v_g^{l,P} d\omega_p^{l,P}, \tag{5.8}$$

for arrays with 100 and 500 nm diameter disks and $\Delta x/D = 1.1$. The results are plotted in Figs. 5.5(a) and 5.5(b). All modes (including those with $k > 0$) were considered in this calculation. The fundamental dipole modes are the main heat carriers, with longitudinal modes dominant over transverse modes. The contribution of $k > 0$ modes to the net thermal conductivity is less than 0.1% as a consequence of their small group velocities.

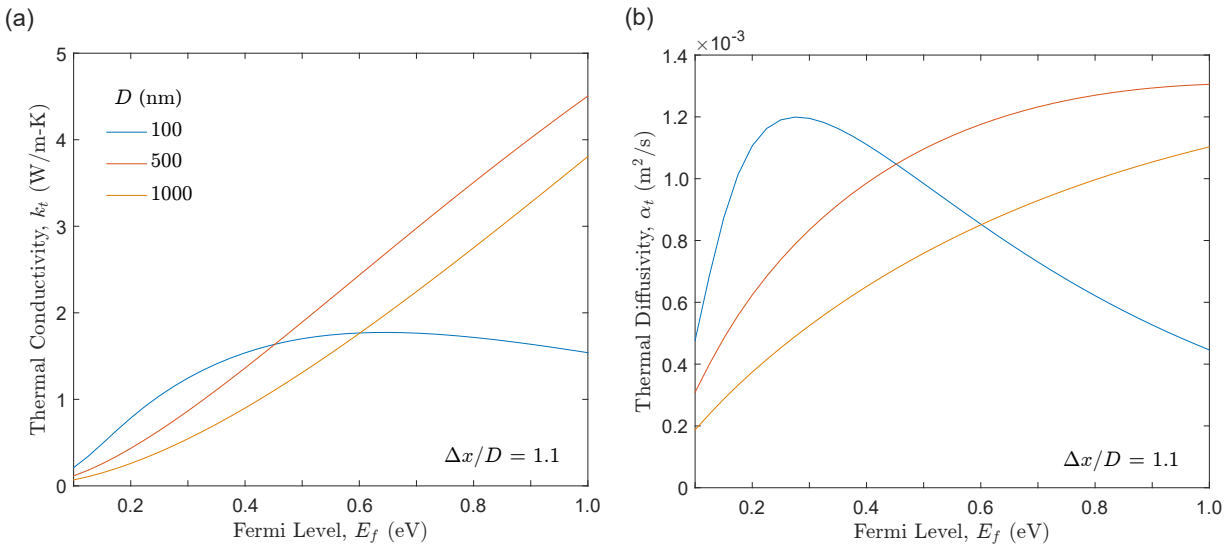

Figure 5.6: (a) Thermal conductivity and (b) thermal diffusivity as a function of the Fermi level in a graphene disk array with $\Delta x/D = 1.1$ and disk diameters of 100, 500, and 1000 nm on a dielectric substrate ($\varepsilon_2 = 2.4$).

For the disk array with $D = 500$ nm, there is a higher number of modes carrying heat ($l = \pm 1, \pm 2, \pm 3, \pm 4, \pm 5$) in comparison with the case for $D = 100$ nm ($l = \pm 1, \pm 2$), which is a result of the larger thermal activation when the diameter increases. Thus, varying the disk diameter (or E_f or ε_2) allows for direct control of the number of thermally-activated modes.

5.4.2 Fermi-level tuning of thermal transport

We now explore the tunability of thermal conductivity by varying the Fermi level up to 1 eV, as can be achieved from electrical gating. In Fig. 5.6(a), the thermal conductivity dependence on the Fermi level is plotted for disk arrays with $\Delta x/D = 1.1$, $\varepsilon_2 = 2.4$, and $D = 100$, 500, and 1000 nm. For a diameter of 100 nm, the thermal conductivity increases with E_f until it reaches a maximum at $E_f = 0.65$ eV, which indicates the existence of competing effects. As explained by Eqns. (5.3) and (5.5), when E_f is reduced, the plasmonic spectrum redshifts and the decay length is reduced. Thus, similar to the competing effects

associated with changing the disk diameter [see Fig. 5.4(b)], the increased population of thermally-activated modes competes with the reduction in $\hbar\omega_p$ and L_p. For diameters of 500 and 1000 nm, the maximum thermal conductivity is reached at Fermi levels larger than 1 eV, so that the thermal conductivity increases monotonically over the accessible range.

The effect of the Fermi level on the thermal diffusivity, α_t, is now analyzed. As surface plasmons are supported by the conduction electrons in graphene, the heat capacity of electrons, C_t^e, also needs to be considered, which is given by [92]

$$C_t^{e^-} = \frac{1}{3}\pi^2 D_e(E_f)\frac{k_B^2 T}{t}, \tag{5.9}$$

where $D_e(E) = 2E/(\pi\hbar^2 v_f^2)$ is the electron density of states in graphene [15]. As a reference, for $E_f = 0.1 - 1.0$ eV and $T = 300$ K, the electronic heat capacity ranges from 350 to 3500 J/m^3-K, which is three to four orders of magnitude larger than the plasmonic heat capacity.

The thermal diffusivity is thus calculated as $\alpha = k_t/(C_t + C_t^{e^-})$ and is plotted as a function of the Fermi level in Fig. 5.6(b). For a disk diameter of 100 nm, the thermal diffusivity reaches a maximum of 1.2×10^{-3} m^2/s at $E_f = 0.275$ eV. For diameters of 500 and 1000 nm, the thermal diffusivity grows monotonically over the accessible range of E_f, reaching values of 1.1×10^{-3} and 1.3×10^{-3} m^2/s at $E_f = 1.0$ eV. These values are ten times larger than the largest values reported for metals, suggesting fast response to temperature fluctuations [75].

Thermal diffusivity is a key property in the design of interconnects for thermotronic devices [94], as it sets the distance affected by an oscillating temperature signal (i.e., the thermal penetration depth, δ_{th}). For a sinusoidal temperature oscillation at frequency ν_t,

the thermal penetration depth is [95]

$$\delta_{th} = \sqrt{\frac{\alpha_t}{\pi \nu_t}}. \tag{5.10}$$

Consider an array of 100 nm diameter disks of period $\Delta x = 110$ nm and $E_f = 0.275$ eV on a quartz substrate, where $\alpha_t = 1.2 \times 10^{-3}$ m^2/s. At a frequencies of 4 and 96 MHz, the plasmons can carry energy over distances of 10 and 2 μm. At these frequencies, the temperature signal in quartz substrate decays at much shorter lengths of 0.7 and 0.1 μm, given its low thermal diffusivity (5.3×10^{-6} m^2/s) [75]. These frequencies are in the range of the bandwidth observed in photon-based thermal rectification [65]. Additionally, the frequencies of the thermally active plasmons modes (Fig. 5.5) are in the same range as the resonant frequencies for materials used in photon-based thermotronic devices [65, 67, 96, 97], meaning that the near-field coupling between the disk array and such devices can be strong. Graphene disks waveguides are thus highly compatible with thermotronic devices.

5.5 Conclusions

We studied plasmonic thermal transport in graphene nanodisk arrays. The coupling between disks was modeled using a semi-analytical model based on the electrostatic approximation. The plasmonic bandstrucure showed multiple non-localized bands, and $1/e$ decay lengths as large as 3.1 μm for 100 nm disk arrays [Figs. 5.1(a) and 5.1(b)]. As shown in Table 5.1, our electrostatic model can predict the plasmon frequencies(decay lengths) in arrays with disk diameters smaller than 200 nm to within 0.4(10)% of a model that considers radiation damping. As such, the plasmonic properties are well-described by non-dimensional analysis for disk diameters bellow 200 nm. At low temperatures, a set of scaling rules can be derived for the dispersion relations and decay length (Fig. 5.3). The

non-dimensional models demonstrate that the frequencies and decay lengths of guided plasmon modes can be tuned by changing the disk size and separation, substrate properties, and graphene's intrinsic optical properties, Fermi level, and electron mobility.

Heat carried by surface plasmons in disk arrays at room temperature offers tunable heat capacity and thermal conductivity up to 0.48 J/m^3-K [Fig. 5.4(a)] and 4.5 W/m-K [Fig. 5.4(b)] and control over the activated modes, as shown in Fig. 5.5. We demonstrated a Fermi level-dependent thermal conductivity and thermal diffusivity with values ranging up to 4.5 W/m-K (Fig. 5.6(a)) and 1.4 $\times 10^{-3}$ m^2/s (Fig. 5.6(b)). The thermal diffusivities are ten times larger than those of metals. We note that our calculations consider a graphene thickness of 0.5 nm. If a value of 0.34 nm is considered, which is consistent with other studies of thermal transport in graphene, the thermal conductivity and heat capacity would increase by a factor of 1.47. The thermal diffusivity is not affected by a change in the thickness.

Our results suggest that thermally-activated surface plasmons in graphene disk arrays can lead to long-range, tunable, and fast thermal transport. The tunable plasmonic band structure can be exploited to achieve strong near-field radiative coupling between the array and other thermotronic devices, suggesting compatibility for integration as thermotronic interconnects.

Plasmon-induced hot carriers in nanosphere dimers

6.1 Introduction

Plasmonic nanoparticles are regarded for their ability to strongly confine light. The strong light confinement has been used in application such as light-trapping [1], sensing [98], or local heating [99]. The later is a product of the Joule heating that takes place due to the scattering of the excited carriers. These excited carriers correspond to induced hot electrons and holes from the non-radiative decay of surface plasmons. They are considered *hot* because their energies are larger than those of thermal excitations at ambient temperatures.

The decay process of a plasmon and the subsequent local heating is described in Fig. 6.1 [3]. The first step corresponds to light absorption and excitation of localized surface plasmons, as shown in Fig. 6.1a. The surface plasmons decay radiatively via re-emission of photons or non-radiatively via excitation of hot electrons and holes (Fig. 6.1b). This process occurs at very short time scales, ranging between 1 to 100 fs. Next, hot-carriers relax via electron-electron or electron-phonon scattering, at time scales ranging from 0.1 to 1 ps, as shown Fig. 6.1c. In this process, the overall temperature of the system increases. Finally thermal dissipation occurs, at time scales from 0.1 to 10 ns (Fig. 6.1d).

By inducing intermediate processes before hot carrier relaxation occurs, however, highly energetic electrons and holes can be extracted for applications such as induced photochemistry [23], photovoltaic energy conversion [9], or photodetection [8]

The induced modification in the spectral response by surface plasmon hybridization can

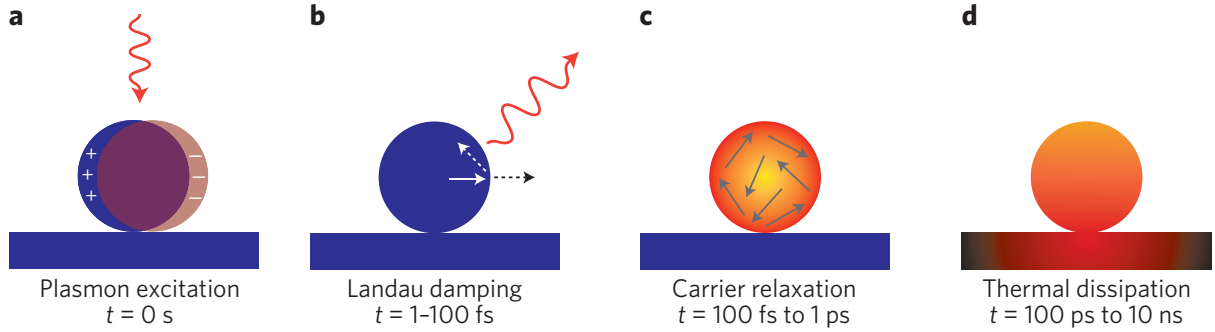

Figure 6.1: Photoexcitation and subsequent relaxation processes upon illumination of a metal nanoparticle with light and characteristic timescales [3]. (a) First, the excitation of a localized surface plasmon redirects the flow of light towards and into the nanoparticle. (b) LSP resonances are damped by radiative and non-radiative processes, via photon re-emission and electron-hole pairs excitation, respectively. (c) Excited electrons relax via scattering losses. (d) The system reach thermal equilibrium, leading to Joule heating of the particle and surroundings.

play an important role in the generation of hot carriers. As an example, plasmon coupling between two metal nanoparticles generates a splitting of the plasmonic resonances into a symmetric and a non-symmetric mode, whose frequencies and intensities can be tuned according to the particle separation and diameters [100]. A change in the absorption has direct consequences in the radiative decay of surface plasmons, and thus in the generation of hot carriers. Furthermore, the strong near-field coupling between nanoparticles induces regions of strong electric field intensity, so-called hot spots. These hot spots have demonstrated larger generation of hot carriers in comparison with those from a single sphere [101].

Although the enhanced generation of hot carriers in nanosphere dimers have been demonstrated [101], a clear description of the mechanisms involved is still not available. This is because previous studies are based in the electromagnetic field distribution obtained from numerical simulations, which are computationally expensive when used to predict the generation of hot carriers. For example we observed that the prediction of hot carrier generationin a 5 nm diameter sphere dimer using this method, can take approximately three

months at a single photon frequency.

Here, we will study the effect of coupling between metal nanostructures in the generation of hot carriers. We develop an analytical solution to model the electrostatic potential from nanopsheres clusters, which is based on the boundary charge method. This electric potential is then used to calculate the number of induced hot carriers by application of the Fermi golden rule. We consider a free electron model to describe the electronic states inside the metal, which is accurate for materials like silver, where interband transitions can be ignored [102, 103]. The calculation of hot carrier generation from our analytical model demonstrated higher efficiency than those form numerical simulations. Thus, we are able to explore different scenarios and understand the role of surface plasmons hybridization in hot carrier generation.

6.2 Methods

We consider silver nanospheres with sizes smaller than the light in the free space. Under this regime, the electrostatic approximation can be used, and the coupling between spheres is well described by the boundary charge method (BCM). Thus, the electrostatic potential on a sphere of radius R is given by:

$$\psi(r,\Omega) = \frac{1}{\varepsilon_0}\sum_{lm} c_{lm}\frac{R}{2l+1}\frac{1}{R^{3/2}}\left(\frac{r}{R}\right)^l Y_{lm}(\Omega_r), \tag{6.1}$$

where c_{lm} is the expansion coefficient obtained from the BCM), l and m are the angular momentum indexes and $Y_{lm}(\Omega_r)$ is the spherical harmonics at the solid angle Ω_r.

The electronic states are given by the solutions of the spherical quantum well problem:

$$\Psi = Aj_l\left(\frac{\sqrt{2m_eE}}{\hbar}\right)Y_{lm}(\Omega_r), \tag{6.2}$$

where j_l is the spherical Bessel function,

$$A = \sqrt{\frac{2}{R^3 j_{l+1}^2(\xi_{ln})}},$$

is the normalization constant, and

$$E = \frac{\hbar \xi_{ln}^2}{2m_e R^2},$$

is the electron energy. ξ_{ln} corresponds to the nth zero of the Bessel function j_l.

The number of excited hot electrons per unit time and volume is given by the Fermi golden rule

$$T_e(\epsilon_f, \omega_p) = \frac{4}{\tau_e} \sum_i f(\epsilon_i)[1 - f(\epsilon_f)] \cdot \left\{ \frac{|M_{fi}(\omega_p)|^2}{(\hbar\omega_p - \epsilon_f + \epsilon_i)^2 + \hbar^2 \tau_e^{-2}} + \frac{|M_{if}^*(\omega_p)|^2}{(\hbar\omega_p - \epsilon_i + \epsilon_f)^2 + \hbar^2 \tau_e^{-2}} \right\}, \tag{6.3}$$

where ϵ_f and ϵ_i correspond to the energies of electrons at the initial and final states, τ_e is the relaxation time of the hot carriers, ω_p is the frequency of the photon, and

$$M_{fi}(\omega_p) = \frac{1}{V} \int_V \Psi_f^*(\mathbf{r}) \psi(\mathbf{r}) \Psi_i(\mathbf{r}) dV \tag{6.4}$$

is the transition matrix element. A factor of two is included in Eqn. (6.3) to account for spin. The number of generated hot holes per unit time can be directly obtained from Eqn. (6.3) by interchanging the subscripts i and f after the summation symbol.

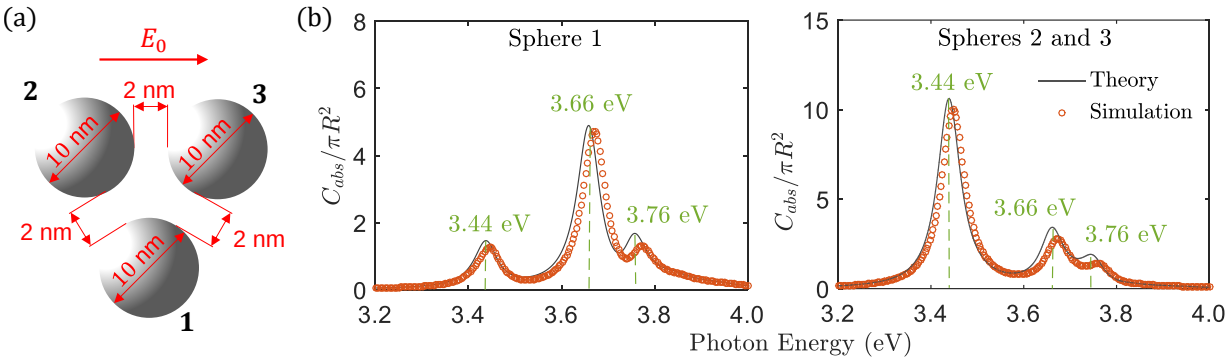

Figure 6.2: (a) Schematic of the three nanosphere cluster. (b) Absorption efficiency from each sphere in the three-nanosphere cluster.

6.3 Results

6.3.1 Validation of boundary charge methods for nanosphere clusters

Here, we validate our electrostatic model by calculating the absorption cross section of a three nanosphere cluster, as shown in Fig. 6.2(a). We consider an incident planewave with the electric field polarized along the axis connecting spheres 2 and 3. The array consists of three nanospheres of diameter 10 nm, forming a equilateral triangle, with a separation of 2 nm between the sphere surfaces. Our calculation are compared with numerical simulations using the boundary element method. The results are plotted in Fig. 6.2(b), showing excellent agreement between the two methods. The absorption spectrum is characterized by three resonances at photon energies of 3.44, 3.66, and 3.76 eV. The lower energy resonance is characterized by a stronger absorption from spheres 2 and 3, while the second peak at 3.66 eV is dominated by the absorption in sphere 1. The higher frequency peak shows low absorption in the three spheres.

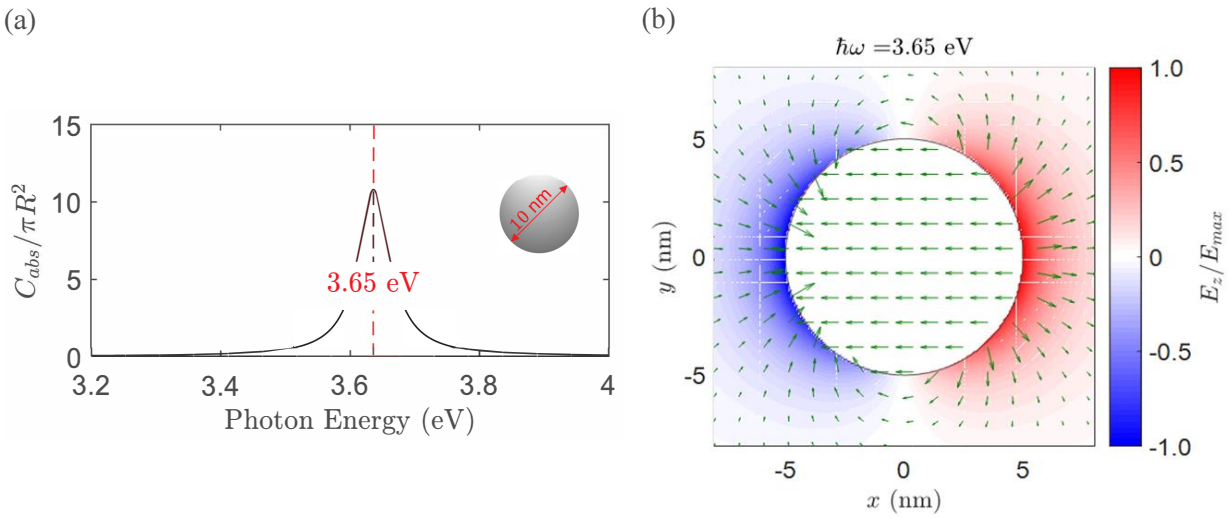

Figure 6.3: (a) Absorption efficiency from one nanosphere of diameter 10 nm excited by a planewave with the electric field polarized in the x direction. (b) Electric field distribution in the nanosphere. The arrows represent the intensity and direction of the components parallel to the plane, and the colors correspond to the intensity of the components normal to the plane, which are normalized by the maximum intensity of the normal components.

6.3.2 Hot carrier generation in a single sphere

In this section we study the generation of hot carriers in a single sphere of diameter 10 nm. We begin by calculating the absorption efficiency, as shown in Fig. 6.3(a). The absorption spectrum is characterized by a single peak at a photon energy 3.65 eV. This peak is characteristic of a surface plasmon resonance. The electric field distribution obtained from our analytic model is plotted in Fig. 6.3(b) showing patterns characteristic of dipole excitation.

We calculate the hot carrier generation from Eqn. (6.3) at at the resonance condition. The results plotted in 6.4 consider the hot carrier generation at the relaxation times 0.1, 0.5 and 1.0 ps. At $\tau_e = 0.1$ ps a pronounced peak near the Fermi level is observed for electrons and holes. The shape of the curve is characteristic of carrier generation at low relaxation times [102], and is the product of the larger magnitude of the transitions elements close to the Fermi level [104]. This is the underlying mechanism behind the Drude model [101].

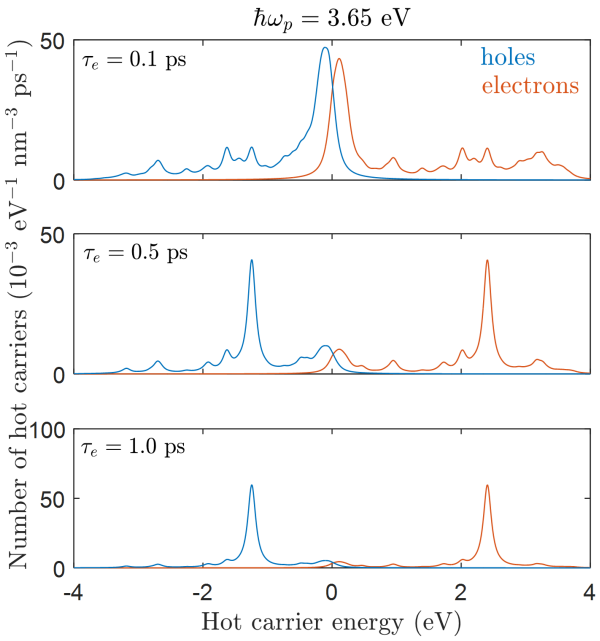

Figure 6.4: Number of excited hot electrons (red) and holes (blue) in a single sphere of 10 nm diameter for a photon energy 3.65 eV and relaxation times of 0.1, 0.5, and 1.0 ps.

At $\tau_e = 0.5$ ps the curves show to pronounced peak at -1.24 eV and 2.41 eV away from the Fermi level for hot holes and electrons, respectively. In this case, a larger relaxation time favors direct electronic transitions, which becomes evident by the energy difference between the two peaks matching the energy of the incident photon (3.65 eV) [102]. The response prevails for $\tau_e = 1.0$ ps, although with a larger number of generated hot carriers.

6.3.3 Hot carrier generation in a nanosphere dimers

Here, the hot carrier generation in a nanosphere dimer is studied. We consider two nanospheres of diameter 10 nm with a separation between surfaces of 2 nm. The incident electric field is polarized along the common axis between the two spheres. The absoption efficiency of one of the spheres is shown in Fig. 6.5. As a result of hybridization, two resonant peaks at 3.43 eV and 3.73 eV are present, with a larger absorption efficiency at the lower frequency peak.

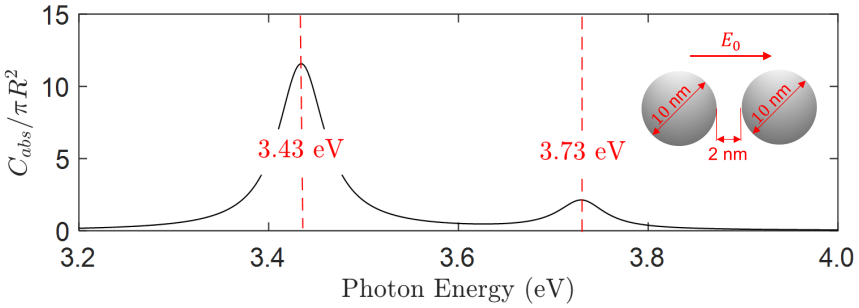

Figure 6.5: Absorption efficiency from two nanosphere of diameter 10 nm with a separation of 2 nm between surfaces. The incident electric field is polarized along the common axis between the two spheres

The spectral response of the dimer is characteristic of nanosphere dimers [55] and is a consequence of the constructive and destructive interference of the hybrid eigenmodes. This is explained in Fig. 6.6(a) and 6.6(b), where the electric field distribution at the two resonant peaks is shown. The resonance at 3.43 eV is characterized by two dipole modes oriented in the same direction. We refer to this mode as the symmetric mode. As the two dipoles are aligned, constructive interference induces a larger response. A restoring force opposed to the direction of the dipoles is developed, which reduces the resonant frequency from the original resonance of a single sphere. As a consequence, strong near-field coupling is developed in this region, which is known as a plasmonic hot spot. The electric field distribution at 3.73 eV is characterized by two dipoles oriented in opposite directions. We refer to this mode as the anti-symmetric mode. In this case, a small dipole is developed at the gap between the two spheres, with a resulting larger resonance condition. Because of the opposite orientation of the dipoles, destructive interference occurs, reducing the intensity of the absorbed light.

The hot carrier generation at the two resonant peaks is now investigated. The results are plotted in Fig. 6.6(c) and 6.6(d), and show the hot carrier generation at relaxation times of 0.1, 0.5, and 1.0 ps. The anti-symmetric mode shows a general lower generation rate than the symmetric mode and the single sphere. This is the result of the lower energy absorbed

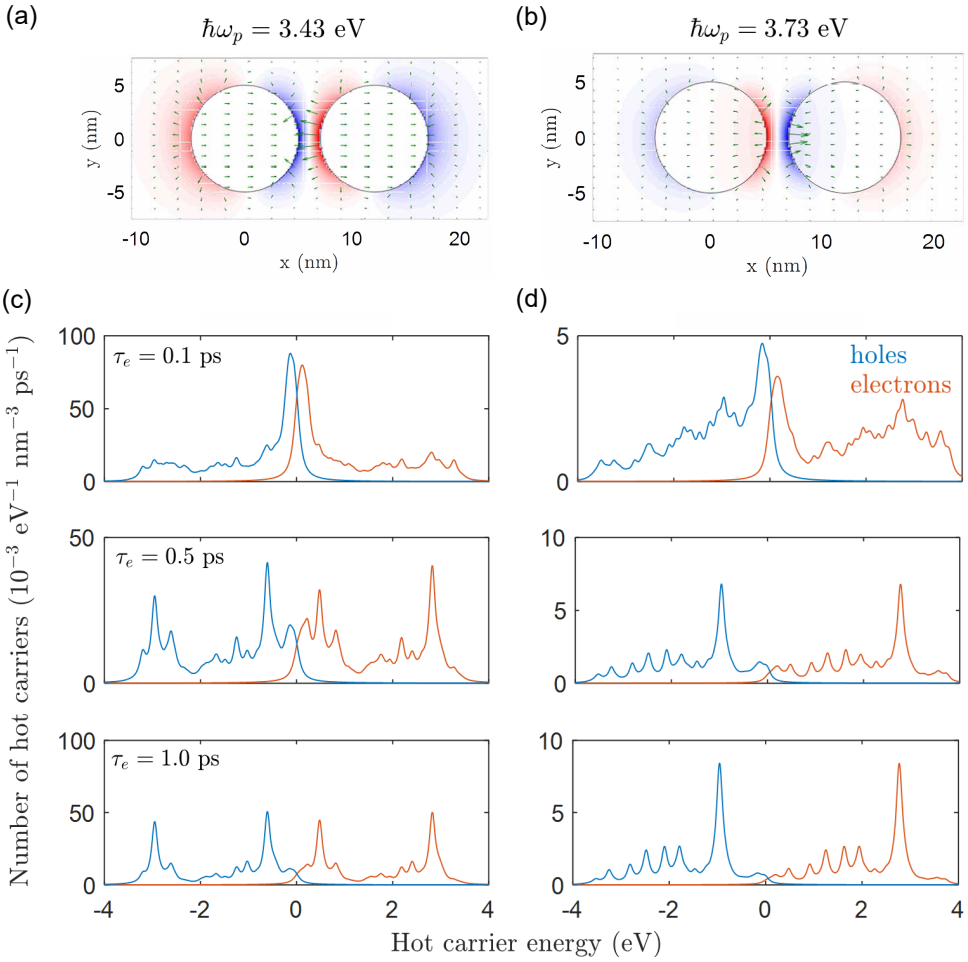

Figure 6.6: Electric field distribution for two nanospheres of diameter 10 nm and separation 2 nm excited by a planewave with the electric field polarized in the x direction, at (a) 3.43 eV and (b) 3.73 eV. The arrows represent the intensity and direction of the components parallel to the plane and the colors correspond to the intensity of the components normal to the plane, which are normalized by the maximum intensity of the normal components. Number of excited hot electrons (red) and holes (blue) in a nanosphere dimer of 10 nm diameter and 2 nm separation at relaxation times of 0.1, 0.5, and 1.0 ps and a photon energy of (c) 3.43 eV and (d) 3.73 eV

.

at this frequency. The symmetric mode shows a pronounced peak for hot electrons and holes close to the Fermi level when $\tau_e = 0.1$ ps, similar to the the response observed for a single sphere. At $\tau_e = 0.5$ ps, however, both hot electrons and hot holes show two sharp peaks at 3.12 and 0.61 eV for holes, and at 0.31 and 2.82 eV for electrons. This effect can be explained by the larger absorbed energy together with the influence of the plasmonic hot-spot.

In terms of computational time, the hot carrier generation obtained from the analytical solution was completed in 13 hours. This is comparatively more efficient than a prediction of hot carrier generation from numerical simulations, which we predicted to be 3 months for a 5 nm sphere dimer.

6.4 Summary

In this chapter the plasmon-induced hot carrier generation in nanosphere dimers was studied. The calculations are based on an analytical model under the electrostatic approximation that predicts the electromagnetic response of the dimer. The analytical model showed excellent agreement with numerical simulations using the boundary element method. The hot carrier generation is predicted using the Fermi golden rule considering a free electron model for the electronic states in the sphere and the electrostatic potential from our analytical model to calculate the transition matrix elements. This scheme allowed prediction of hot carrier generation in 150 times less computational time than using numerical simulations. The hot carrier generation in the dimer showed a larger number of generated hot carriers for the symmetric mode in comparison with that from a single sphere. When the relaxation time of hot carriers is larger than 0.5 ps, two pronounced peaks are observed for the hot electrons and holes. Each pair of electron-hole peaks is associated with direct transition due to photon absorption. This differs from the results in a single sphere, where only

one direct transition was observed. The results indicate the potential of surface plasmon hybridization to enhance hot carrier generation away from the fermi level, with potential applications in photochemistry and photovoltaic energy conversion. The efficiency of our model represent a first step towards studies of hot carriers generation in large scale systems such as large nanosphere clusters or long arrays.

Summary and Outlook

7.1 Overview

The work presented in this thesis focused on analyzing surface plasmon hybridization in novel plasmonic phenomena such as thermal transport in graphene plasmonics and plasmon-induced hot carrier generation. The electromagnetic response of nanoparticles clusters and arrays was predicted using surface plasmon hybridization theory under the basis of the boundary charge method. This method considers nanoparticles of sizes smaller than the wavelength of the electromagnetic field in the surrounding, such that the electrostatic approximation is valid. Based on this general formalism, analytical models for graphene nanodisks and silver nanospheres were obtained.

In Chapter 3, the extreme blueshift of the lowest surface plasmon resonant frequency by hybridization in graphene disk stacks was studied. After a systematic study considering the effect of the distance between disks and number of layers, it was observed that only one hybrid mode becomes blueshifted. For disk diameters as small as 50 nm and a Fermi level of 1.0 eV, it was predicted that the blueshifting saturates at a photon energy of 0.75 eV, which correspond to the near-IR spectrum.

In Chapter 4, the near-field radiation in a graphene disk dimer was studied. Using an analytical model, the near-field radiative thermal conductance between two graphene disks in co-axial and co-planar configurations was calculated as a function of the distance between them. The accuracy of the analytical model allowed us to predict the near-field thermal conductance at very small gaps, reaching a limit resembling the radiation heat exchange between extended graphene sheets. In this limit, two and four orders of magnitude

enhancement of the thermal conductance over the blackbody limit was predicted for co-planar and co-axial disk configurations. Analysis of thermal radiation as a function of the orientation between disks revealed regions of low thermal conductance, which are caused by destructive interference between hybrid modes.

In Chapter 5, the plasmonic thermal transport in one dimentional graphene nanodisk array was studied. The analytical model for graphene disks was used to predict the plasmonic bandstructure under a large number of scenarios. The plasmonic bandstructures show a large number of non-localized bands, and tunability over the frequency spectrum, and $1/e$ decay lengths. A large degree of confinement for the lowest dipole modes was predicted for disk arrays of sizes smaller than 200 nm. Thus, the effect of radiation damping can be neglected, allowing the use of non-dimensional analysis under the electrostatic approximation. The energy of the guided plasmonic modes in graphene disk arrays is comparable to the thermal energy of the system at room temperature. Heat capacities and thermal conductivities up to 0.48 J/m^3-K and 4.5 W/m-K were predicted, with control over the number of thermally activated bands. The predicted thermal diffusivity as a function of the Fermi level showed values up to 1.4×10^{-3} m^2/s, which is ten times larger than those of metals. Given the large values of thermal diffusivity, a fast transient response under temperature fluctuation is predicted, which can be explored for interconnects in photon-based thermotronics.

In Chapter 6, the hot carrier generation induced by surface plasmons in silver nanosphere dimers was explored. An analytical model for near-field coupling between the nanospheres was developed, allowing for fast calculation of hot carrier generation. Calculation of the absorption efficiency of a nanosphere dimer with the electric field polarized along the common axis between the spheres showed two resonance modes. The low frequency mode is characterized by a large absorption with symmetrically-oriented dipoles in the two spheres.

The high frequency mode showed lower absorption with two anti-symmetrically-oriented dipoles. The results of hot carrier generation showed larger generation rates for the symmetric mode in comparison with that for the anti-symmetric mode. When the relaxation time of electrons is larger than 0.5 ps, both electron and hole generation rates showed two peaks near 0 and at 3 eV away from the Fermi level. This behavior differs form the response of a single sphere where a single peak was observed for electrons at 3 eV and for holes near 0 eV.

7.2 Future Work

The work presented in this thesis elucidated the influence of plasmonic hybridization in the response of graphene plasmonic nanostructures and plasmon-induced hot carrier generation. Possible future directions include the study of graphene for photon-based thermotronic devices, photon upconversion in plasmonic dimers, and near-field thermophotovoltaic energy conversion.

7.2.1 Graphene nanostructures for photon-based thermal devices

As our results suggest, surface plasmons in graphene nanostructures offer great tunability over thermal radiation together with large thermal diffusivity, which translates into large control over the thermal radiation properties and fast response under temperature fluctuations. The latter statement is supported by recent findings [69], showing that the relaxation of electrons in a graphene disk due to thermal radiation to a neighboring disk occurs at shorter time scale than that due to electron-phonon scattering. The next step, will be towards experimental validation of these findings. As the presence of the substrate might strongly suppress the thermal conductivity signal, we suggest transient measurement techniques such as frequency domain thermoreflectance [105] or transient grating [106], which

allow a direct observation of the thermal diffusivity. The fabrication of an appropriate sample is not trivial, however, as current methods to pattern a graphene layer into an array of disks are known to reduce the optical losses [15], therefore strongly suppressing the thermal transport properties. Thus, cleaner fabrication methods are crucial for these measurements.

From a theroretical perspective, a future direction for thermally induced plasmons in graphene is in the development of photon-based thermotronic devices such as rectificators, transistors, and modulators. At low Fermi levels, the plasmonic response of graphene nanodisk is strongly dependent on the temperature. Thus, the radiation channels between two disks can be tuned on and off by varying the temperature of each disk, producing thermal rectification. The same reasoning can be used for thermal transistors. In the case of modulators, the heat flowing in two graphene disk arrays with different plasmonic band structures, can be combined to generate destructive or constructive interference. As the number of activated modes can be controlled, coherent heat can be exploited to achieve a large degree of modulation.

7.2.2 Hot carrier generation in large scale nanospheres clusters

The fact that surface plasmon hybridization modifies the generation of hot carriers from that of a single nanoparticle, sets a new paradigm for geometry-assisted transitions which can be efficiently modeled with the boundary charge method. Sphere heptamers, for example, can induce strong non-symmetric resonances, known as Fano-resonances [107], that induce region of the spectrum with strong absorption and low scattering. The anomalous response have been used to reduce the radiative decay of surface plasmons, and thus achieve optimal generation of hot carriers [8]. We anticipate that, besides the reduction in the radiative decay, the modification of the electromagnetic field distribution induced

by the Fano-resonance adds additional channels for electronic transitions. The boundary charge method will allow to quantify the relative contribution to hot carrier generation from these two mechanisms.

Another interesting problem correspond to the shifting of resonance modes to parts of the spectrum with large optical losses. As hot carrier generation is associated with Landau damping of surface plasmons, it is expected that larger optical losses will provide higher generation rates.[3]

7.2.3 Near-field thermophotovoltaic energy conversion

Thermophotovoltaic devices consist in the photovoltaic energy conversion of the thermal radiation emitted by a hot source different from the sun. Such devices offers a theoretical maximum conversion efficiency of 85% [108], beyond the estimated limit of a single junction solar cell. However, experimental results have only reached a maximum conversion efficiency of 6.8% [109].

As the distance between the emitter and photovoltaic converter can be reduced, near-field energy conversion can be achieved, with an expected increase in the efficiency. Thus, a theoretical maximum efficiency of a near-field based thermophotovoltaic energy conversion device have demonstrated to be 36%, using a photovoltaic cell based on III-V semiconductor [110]. However, fabrication of flat and cost effective III-V semiconductors still remains a challenge [111].

Strong near-field coupling can be largely enhanced when the two surfaces exchanging heat support surface electromagnetic modes at similar frequencies [19]. Thus, an alternative to III-V semiconductors would be replacing the photovoltaic cell by a metal layer enabling the generation of hot carriers. The hot carriers can be extracted by creating a Schottky barrier between the metal layer and a semiconductor. The idea, proposed by St-Gelais

et al [111], exploits both the ability to generate surface modes and the generation of hot carriers, with an estimated efficiency of 10-30% at 900-1500 K. Their study does not consider calculations of hot carrier generation. Instead, a fixed value of quantum efficiency is considered. Our analytical model for near-field coupling between spheres can be extended to include near-field thermal radiation, which can be used to explore the consequences on the generation of hot carriers. Thus, the hot carrier generation induced by near-field radiation between two spheres can be explored.

Analytical Solutions for Disk and Spheres

A.1 Analytical solution for plasmonic spheres

For a sphere of radius R, a convenient expansion of the surface charge is given by an orthogonal basis of the form [44]

$$\beta_{lm}(\Omega) = \frac{1}{R^{3/2}} Y_{lm}(\Omega), \tag{A.1}$$

where Ω is the solid angle formed from the center of the sphere

The electrostatic Green's function in spherical coordinates is given by [24]

$$\frac{1}{4\pi\,|\boldsymbol{r}-\boldsymbol{r}'|} = \sum_{l=1}^{\infty}\sum_{m=-l}^{l} \frac{1}{2l+1} Y_{lm}(\Omega) Y^{*}_{lm}(\Omega) \frac{r_{<}^{l}}{r_{>}^{l+1}} \tag{A.2}$$

where $r_{<}(r_{>})$ is the smaller(larger) of $|\mathbf{r}|$ and $|\mathbf{r}'|$, and l ($l = 0, 1, ...$) and m ($m = ..., -2, -1, 0, 1, 2, ...$) represent the index for the zenith and azimuth angles.

The self interaction matrices $G^{\nu}, \nu\nu$ and $G^{0,\nu\nu}$ are given by:

$$G^{\nu,\nu\nu}_{l_1 m_1, l_2 m_2} = \frac{1}{2}\eta \frac{1}{2l_1+1}\delta_{l_1 m_1, l_2 m_2}$$
$$G^{0,\nu\nu}_{l_1 k_1, l_2 k_2} = \frac{1}{2(2l_1+1)}\delta_{l_1 m_1, l_2 m_2},$$

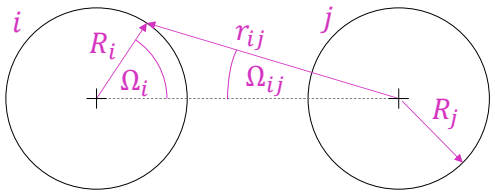

Figure A.1: Coordinates that describe the interaction between two spheres labeled i and j

The interaction matrix element between two spheres i and j, $G^{0,ij}_{l_i m_i, l_j m_j}$, is given by

$$G^{0,ij}_{l_i m_i, l_j m_j} = \sqrt{\frac{R_i}{R_j}} \cdot \frac{l_i R_j^{l_j+1}}{2l_j+1} \int_{\Omega_i} \frac{Y^*_{l_i m_i}(\Omega_i) Y_{l_j m_j}(\Omega_{ij})}{[r_{ij}(\Omega_{ij})]^{l_j+1}} d\Omega_i \tag{A.3}$$

where Ω_{ij} and $r_{ij}(\Omega_{ij}$ correspond to the solid angle and radius formed between the center of sphere j and a point at the surface of the sphere i, as shown in Fig. A.1.

A.2 Analytical solution for graphene nanodisks

For a disk of radius R, a convenient expansion of the surface charge is given by an orthogonal basis in cylindrical coordinates (r, ϕ, z) of the form[45]

$$\beta_{kl}(r, \phi) = P_k^{(L,0)}(1-2x^2) x^L \Theta(1-x) \frac{1}{\sqrt{2\pi}} e^{i\phi l}, \tag{A.4}$$

where $L = |l|$, $x = r/R$, $P_k^{(L,0)}$ are Jacobi polynomials, Θ is the step function, and k $(k = 0, 1, ...)$ and l $(l = ..., -2, -1, 0, 1, 2, ...)$ represent the radial and angular modes.

The advantage of using Eqn. (A.4) lies in the identity[112]

$$\int_0^R \beta_{kl}(r, \phi) J_l(pr) r dr = R p^{-1} J_{L+2k+1}(Rp) \frac{1}{\sqrt{2\pi}} e^{i\phi l}. \tag{A.5}$$

The electrostatic Green's function $K(\boldsymbol{\gamma}, \boldsymbol{\gamma}') = \frac{1}{4\pi|\boldsymbol{\gamma}-\boldsymbol{\gamma}'|}$ in cylindrical coordinates is given

by [24]

$$K(\boldsymbol{\gamma},\boldsymbol{\gamma}') = \frac{i}{2\pi}\sum_{l=-\infty}^{+\infty} e^{l(\phi-\phi')}\int_0^{\infty} Z_l(ik_z r)J_l(ik_z r')\cos[k_z(z-z')]dk_z, \tag{A.6}$$

where k_z is the wavevector in the direction normal to the plane of the disk and

$$Z_l(ik_z r) = \begin{cases} H_l(ik_z r) & , r > R \\ J_l(ik_z r) & , r \leq R \end{cases},$$

where H_l and J_l are the Hankel and Bessel functions. Similarly, $g^{\nu}(\boldsymbol{\gamma}_{\parallel},\boldsymbol{\gamma}'_{\parallel})$ can be expressed as [45]:

$$g^{\nu}(\boldsymbol{\gamma}_{\parallel},\boldsymbol{\gamma}'_{\parallel}) = \frac{1}{2\pi}\sum_{l=-\infty}^{+\infty} e^{l(\phi-\phi')}\left[\frac{(rr')^L}{2L} + \int_0^{\infty} J_l(ik_z r)J_l(ik_z r')k_z^{-1}dk_z\right]. \tag{A.7}$$

Using Eqn. (A.4) and the identity from Eqn. (A.5), together with the corresponding Green's functions from Eqns. (A.6) and (A.7), we calculate the self-interaction matrices elements from Eqns. (2.47) and (2.48). The result is [45]

$$G^{\nu,\nu\nu}_{l_1k_1,l_2k_2} = \frac{i\omega R^4}{\sigma(\omega)}\cdot\begin{cases} [4(L+2k_1)(L+2k_1+1)(L+2k_1)+2)]^{-1}\delta_{l_1,l_2} & k_1 = k_2 \\ [8(L+2k_1+1)(L+2k_1+2)(L+k_1+3)]^{-1}\delta_{l_1,l_2} & k_1 = k_2+1 \\ [8(L+2k_1+1)(L+2k_1+2)(L+k_1+3)]^{-1}\delta_{l_1,l_2} & k_1+1 = k_2 \\ 0 & \text{otherwise} \end{cases}$$

$$G^{0,\nu\nu}_{l_1k_1,l_2k_2} = \frac{R^3}{2\varepsilon_0\varepsilon_h}\cdot\frac{(-1)^{k_1-k_2+1}}{\pi[4(k_1-k_2)^2-1](L+k_1+1k_2+1/2)(L+k_1+k_2+3/2)}\delta_{l_1,l_2},$$

where $L = |l_1| = |l_2|$, and δ_{l_1,l_2} is the Kronecker delta that takes the value 1 when $l_1 = l_2$, and 0 otherwise. The presence of δ_{l_1,l_2} in the previous equations means that the interaction between different angular modes is forbidden.

The interaction matrix elements between two different disks m and n, $G^{0,mn}_{l_mk_m,l_nk_n}$, are

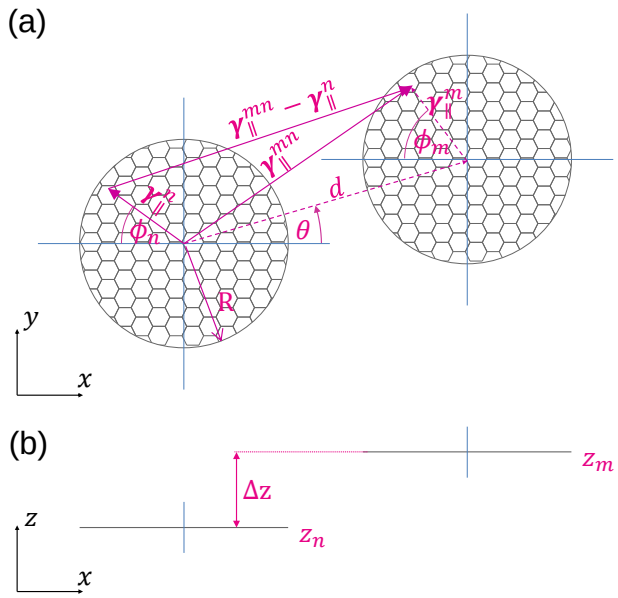

Figure A.2: Coordinates that describe the interaction between two disks labeled m and n. (a) Top view, (b) Lateral view.

obtained by using a transformation of the Green's function from Cartesian to cylindrical coordinates. This procedure allows for a simplification of the calculation by directly using Eqn. (A.5).

We consider the interaction of two disks m and n, as shown in Fig. A.2. Using Green's functions in the plane wave representation [113] the interaction elements are expressed as:

$$G^{0,mn}_{l_m k_m, l_n k_n} = \frac{i}{4\pi^2 \varepsilon_0 \varepsilon_h} \int_{S_m} d^2\boldsymbol{\gamma}_\parallel^m \int_{S_n} d^2\boldsymbol{\gamma}_\parallel^n \iint_{-\infty}^{\infty} d^2\mathbf{k}_\parallel \, {\beta^m_{l_m k_m}}^*(\boldsymbol{\gamma}_\parallel^m) e^{i\mathbf{k}_\parallel \cdot (\boldsymbol{\gamma}_\parallel^{mn} - \boldsymbol{\gamma}_\parallel^n)} \frac{e^{ik_{oz}\Delta z}}{2k_{oz}} \beta^n_{l_n k_n}(\boldsymbol{\gamma}_\parallel^n), \tag{A.8}$$

where $\Delta z = |z_m - z_n|$, $\mathbf{k}_\parallel = k_x\hat{x} + k_y\hat{y}$, and $k_{oz} = i\sqrt{k_x^2 + k_y^2}$.

Using the change of variables $k_r = \sqrt{k_x^2 + k_y^2}$ and $\varphi = \arctan(k_y/k_x)$, we obtain a new

expression for Eqn. (A.8) where the surface integrals are decoupled as

$$G^{0,mn}_{l_m k_m, l_n k_n} = \frac{1}{4\pi^2 \varepsilon_0 \varepsilon_h} \int_0^{2\pi} d\varphi \int_0^{\infty} k_r dk_r \frac{e^{-k_r \Delta z}}{2k_r} e^{ik_r d\cos(\theta-\varphi)} \times \int_{S_m} d^2\boldsymbol{\gamma}^m_{\parallel}\ \beta^m_{l_m k_m}{}^*(\boldsymbol{\gamma}^m_{\parallel}) e^{ik_r r_m \cos(\phi_m-\varphi)} \times \int_{S_n} d^2\boldsymbol{\gamma}^n_{\parallel}\ \beta^n_{l_n k_n}(\boldsymbol{\gamma}^n_{\parallel}) e^{ik_r r_n \cos(\phi_n-\varphi+\pi)}, \tag{A.9}$$

where we use the identity $e^{ik_{\parallel}\cdot\boldsymbol{\gamma}_{\parallel}} = e^{ik_r\cos(\varphi-\phi)}$, where ϕ is the angle formed by $\boldsymbol{\gamma}_{\parallel}$ and the x axis.

The surface integrals from Eqn. (A.9) can be simplified using the identity [24]

$$e^{ik_r r\cos\theta} = \sum_{q=-\infty}^{+\infty} i^q J_q(k_r r) e^{iq\theta}, \tag{A.10}$$

which gives

$$\int_{S_m} d^2\boldsymbol{\gamma}^m_{\parallel}\ \beta^m_{l_m k_m}{}^*(\boldsymbol{\gamma}^m_{\parallel}) e^{ik_r r_m \cos(\phi_m-\varphi)} = R_m^2 \sqrt{2\pi} i^{l_m} B^m_{l_m k_m}(R_m k_r) e^{-il_m\varphi} \tag{A.11a}$$

$$\int_{S_n} d^2\boldsymbol{\gamma}^n_{\parallel}\ \beta^n_{l_n k_n}(\boldsymbol{\gamma}^n_{\parallel}) e^{ik_r r_n \cos(\phi_n-\varphi+\pi)} = R_n^2 \sqrt{2\pi} i^{-l_n} B^n_{l_n k_n}(R_n k_r) e^{il_n\varphi}, \tag{A.11b}$$

where we used Eqn. (A.5) to get $B^n_{kl}(p) = \left(\frac{L}{l}\right)^l p^{-1} J_{L+2k+1}(p)$.

Inserting Eqns. (A.11a) and (A.11b) into Eqn. (A.9) gives

$$G^{0,mn}_{l_m k_m, l_n k_n} = \frac{R_m^2 R_n^2}{\varepsilon_0 \varepsilon_h} \int_0^{\infty} dk_r B^m_{l_m k_m}(R_m k_r) \times \frac{e^{-k_r \Delta z}}{2} \left[\frac{1}{2\pi} \int_0^{2\pi} e^{ik_r d\cos(\theta-\varphi)} i^{-(l_n-l_m)} e^{i(l_n-l_m)\varphi} d\varphi \right] \times B^n_{l_n k_n}(R_n k_r).$$

Using Eqn. (A.10) the term in the square brackets is reduced and the following expres-

sion is obtained

$$G^{0,mn}_{l_m k_m, l_n k_n} = \frac{R_m^2 R_n^2}{2\varepsilon_0 \varepsilon_h} \int_0^\infty dk_r \; B^m_{k_m,l_m}(R_m k_r) J_{l_n - l_m}(k_r d) e^{i\theta(l_n - l_m)} e^{-k_r \Delta z} B^n_{k_n,l_n}(R_n k_r), \quad \text{(A.12)}$$

which is valid when $d < R$. In the case where $d > R$, the Bessel function, $J_{l_n - l_m}(k_r d)$, needs to be replaced by the Hankel function, $H_{l_n - l_m}(k_r d)$, as only outgoing waves exist in this domain. This last change, however, leads to numerical instability in the integration, which can be solved by the change of variables $k_r = ik_z$. Thus, an appropriate expression expression for the domain $d > R$ is given by

$$G^{0,mn}_{l_m k_m, l_n k_n} = \frac{iR_m^2 R_n^2}{2\varepsilon_0 \varepsilon_h} \int_0^\infty dk_z B^m_{k_m,l_m}(iR_m k_z) H_{l_n - l_m}(ik_z d) e^{i\theta(l_n - l_m)} \cos(k_z \Delta z) B^n_{k_n,l_n}(iR_n k_z). \quad \text{(A.13)}$$

The terms $J_{l_n - l_m}(k_r d) e^{i\theta(l_n - l_m)}$ in Eqn. (A.12) and $H_{l_n - l_m}(ik_z d) e^{i\theta(l_n - l_m)}$ in Eqn. (A.13) represent the strength of interaction between different angular modes. At $d = 0$, this terms becomes δ_{l_m, l_n}, meaning that in the co-axial disks configuration the interaction between different angular modes is forbidden.

Calculation of Scattering and Absorption

B.1 Scattered Power

The scattered power from a single particle i can be obtained from the energy dissipation at the surface of the particle due to the scattered field [57]:

$$P_{scat} = -\frac{1}{2} Re \left[\int_{S_i} \mathbf{J}_i^* \cdot \mathbf{E}_{scat} dS_i \right] \tag{B.1}$$

where $\mathbf{E}_{scat}$ correspond to the scattered field acting on the particle i..

Considering every point at the surface as a small dielectric dipole we get:

$$\lim_{r \to r_0} \mathbf{E}_{scat} = \frac{k^3}{6\pi\varepsilon_0} \mathbf{p} \tag{B.2}$$

where $\mathbf{p}$ is the induced dipole at the surface of the particle.

By inserting Eqn. (B.2) into Eqn. (B.1), and after some algebraic manipulations we get:

$$P_{scat} = \frac{\omega k^3}{12\pi} Im \left[\int_{S_i} \rho_i^* \psi_i dS_i \right] \tag{B.3}$$

Considering a surface charge expansion of the form $\rho = \sum_k c_k \beta_k$, we get:

$$P_{scat} = \frac{\omega k^3 R^3}{12\pi\varepsilon_0} \mathbf{C}^* [\eta \mathbf{G}_i]_{AH} \mathbf{C} \tag{B.4}$$

where $\mathbf{G}_{AH} = \frac{1}{2}(\mathbf{G} - \mathbf{G}^*)$ is the anti-Hermitian part of $\mathbf{G}$.

B.2 Absorbed Power

The energy dissipation at the surface of the particle under the incidence of an external field, $\mathbf{E}_{ext}$, is [57]:

$$P_{scat} = -\frac{1}{2} Re \left[\int_{S_i} \mathbf{J}_i^* \cdot \mathbf{E}_{ext} dS_i \right] \tag{B.5}$$

After some manipulations we get:

$$P_{scat} = \frac{\omega}{2} Im \left[\int_{S_i} \rho_i^* \psi_i dS_i \right] \tag{B.6}$$

Using a surface charge expansion of the form $\rho = \sum_k c_k \beta_k$, we get:

$$P_{scat} = \frac{\omega R^3}{2\varepsilon_0} \mathbf{C}^* [\mathbf{G}_i]_{AH} \mathbf{C} \tag{B.7}$$

Theory of Radiative Heat Transfer for Graphene Disks

C.1 Radiation flux spectrum in the electrostatic limit

Consider two graphene disks, labeled 1 and 2. The electromagnetic energy dissipation in disk 2 due to the electrostatic fields from a random distribution of fluctuating charges in disk 1 is given by

$$P_{1\to 2} = \left\langle \frac{\omega}{2}\mathrm{Im}\langle \rho^2, \Psi^{12}_{out}\rangle \right\rangle,$$

where $\langle \cdots \rangle$ denotes the ensemble average. Since the electric potential at the surface of each disk is continuous (*i.e.*, $\Psi^{12}_{out} = \Psi^{22}_{in}$) we can rewrite the previous expression as

$$\begin{aligned} P_{1\to 2} &= \left\langle \frac{\omega}{2}\mathrm{Im}\langle \rho^2, \Psi^{22}_{in}\rangle \right\rangle = \left\langle \frac{\omega}{2}\mathrm{Im}\left\langle \rho^2, \frac{i\omega}{\sigma(\omega)}(g^2 * \rho^2)\right\rangle \right\rangle \\ &= \left\langle \frac{\omega}{2}\mathrm{Im}\left[\mathbf{c}^*\mathbf{G}^2\mathbf{c}\right] \right\rangle = \frac{\omega}{2}\langle \mathbf{c}^*\mathbf{G}^2_{AH}\mathbf{c}\rangle \\ &= -i\frac{\omega}{2}\mathrm{Tr}\left[\langle \mathbf{X}\mathbf{X}^*\rangle \mathbf{W}^*\mathbf{G}^2_{AH}\mathbf{W}\right]. \end{aligned} \tag{C.1}$$

The external source is driven by the fluctuating charges in disk 1, ρ^1_{fl}. Thus, $\langle \mathbf{X}\mathbf{X}^*\rangle = \langle \mathbf{x}^1\mathbf{x}^{1*}\rangle$, where $\mathbf{x}^1$ is an N_m column vector whose elements are given by $\mathbf{x}^1_i = \frac{i\omega}{\sigma(\omega)}\langle \beta^1_i, g^1 * \rho^1_{\mathrm{fl}}\rangle$.

The elements of the ensemble-average $\langle \mathbf{x}^1 \mathbf{x}^{1*} \rangle$ can be expressed as

$$\begin{aligned}
\langle \mathbf{x}^1 \mathbf{x}^{1*} \rangle_{ij} &= \left\langle \left\langle \beta_i^1, \frac{i\omega}{\sigma(\omega)} \left(g^1 * \rho_{\text{fl}}^1 \right) \right\rangle \left\langle \left(\rho_{\text{fl}}^{1*} * g^1 \right) \frac{-i\omega}{\bar{\sigma}(\omega)}, \beta_j^1 \right\rangle \right\rangle \\
&= \left\langle \beta_i^1, \left\langle \frac{i\omega}{\sigma(\omega)} g^1 * \langle \rho_{\text{fl}}^1(\boldsymbol{\gamma}_\parallel^1) \rho_{\text{fl}}^{1*}(\boldsymbol{\gamma}_\parallel^{1\prime}) \rangle * g^1 \frac{-i\omega}{\bar{\sigma}(\omega)}, \beta_j^1 \right\rangle \right\rangle \\
&= \left\langle \beta_i^1, \frac{i\omega}{\sigma(\omega)} \left\langle g^1 * \frac{1}{\pi\omega} \text{Im} \left[\chi \left(\omega, \boldsymbol{\gamma}_\parallel^1, \boldsymbol{\gamma}_\parallel^{1\prime} \right) \right] \theta(\omega, T_1) * g^1 \frac{-i\omega}{\bar{\sigma}(\omega)}, \beta_j^1 \right\rangle \right\rangle, \qquad \text{(C.2)}
\end{aligned}$$

where $\bar{\sigma}(\omega)$ represent the complex conjugate of the optical conductivity of graphene.

In the last step of Eqn. (C.2) we consider the fluctuation-dissipation theorem [73]

$$\langle \rho_{\text{fl}}^1(\boldsymbol{\gamma}_\parallel^1) \rho_{\text{fl}}^{1*}(\boldsymbol{\gamma}_\parallel^{1\prime}) \rangle = \frac{1}{\omega\pi} \text{Im} \left[\chi \left(\omega, \boldsymbol{\gamma}_\parallel^1, \boldsymbol{\gamma}_\parallel^{1\prime} \right) \right] \theta(\omega, T_1).$$

Here, χ is the linear susceptibility of the surface charge in response to an electric potential.

According to linear response theory, the relation between the linear susceptibility and the surface charge density is given by

$$\rho^1(\boldsymbol{\gamma}_\parallel^1) = \int_{S_1'} \chi \left(\omega, \boldsymbol{\gamma}_\parallel^1, \boldsymbol{\gamma}_\parallel^{1\prime} \right) \Psi^{ext}(\boldsymbol{\gamma}_\parallel^{1\prime}) d^2 \boldsymbol{\gamma}_\parallel^{1\prime}.$$

Thus, using Eqs. (12) and (14) of the main text gives the following representation of χ in terms of the mode expansion

$$\chi \left(\omega, \boldsymbol{\gamma}_\parallel^1, \boldsymbol{\gamma}_\parallel^{1\prime} \right) = \sum_{ij} \beta_i^1(\boldsymbol{\gamma}_\parallel^1) \left[\mathbf{G}_1^{-1} \right]_{ij} \beta_j^{1*}(\boldsymbol{\gamma}_\parallel^{1\prime}). \qquad \text{(C.3)}$$

Substituting Eqn. (C.3) into Eqn. (C.2) gives

$$\langle \mathbf{x}_1 \mathbf{x}_1 \rangle_{ij} = \frac{i}{\pi\omega} \mathbf{G}_{AH}^1 \theta(\omega, T_1). \qquad \text{(C.4)}$$

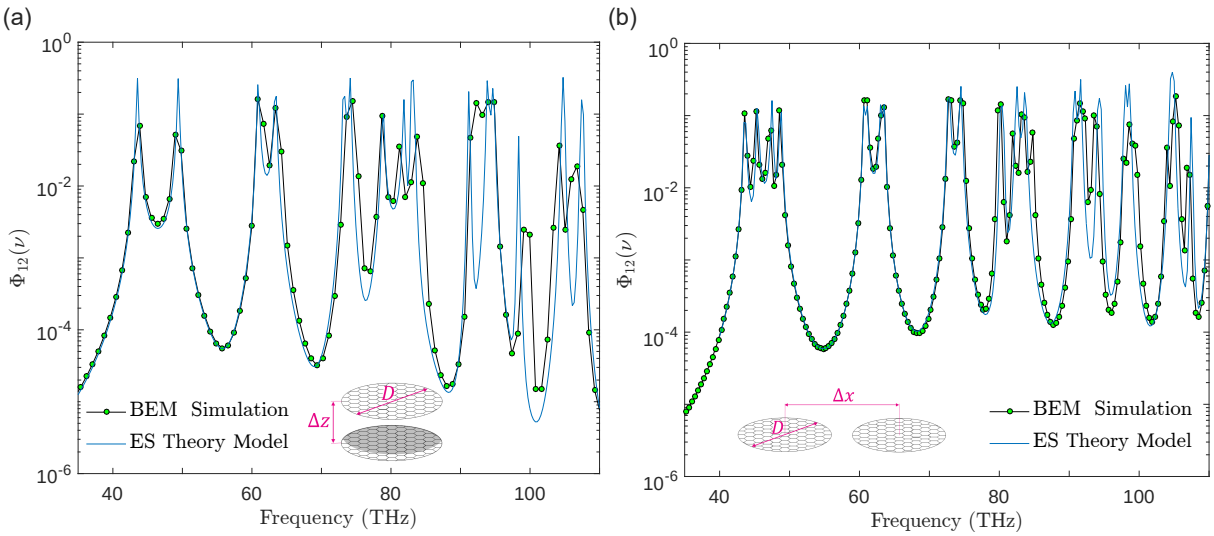

Figure C.1: Comparison of our electrostatic semi-analytical model and BEM simulations for the flux spectrum of two graphene disks ($D = 100$ nm, $E_f = 0.6$ eV) in (a) a co-axial configuration with $\Delta z = 50$ nm, and (b) a co-planar configuration with $\Delta x = 110$ nm.

Finally, by inserting Eqn. (C.4) into Eqn. (C.1) we obtain the following expression for the flux spectrum:

$$\Phi_{12}(\omega) = \frac{1}{2\pi}\mathrm{Tr}\left[\mathbf{G}^1_{AH}\mathbf{W}^*\mathbf{G}^2_{AH}\mathbf{W}\right]. \tag{C.5}$$

C.2 Validation of electrostatic model for near-field radiation

The flux spectrum between two co-axial disks ($\Delta z = 50$ nm) and two co-planar disks ($\Delta x = 110$ nm) obtained using our electrostatic semi-analytical model and from numerical simulations using the BEM-based software package SCUFF-EM [33] are plotted in Figs. C.1(a) and C.1(b). For the BEM simulations, we considered disks with a small thickness, $t = 1$ nm, and an effective dielectric constant for graphene, $\varepsilon_g = 1 - \frac{\sigma(\omega)}{i\omega\varepsilon_0 t}$ [39], where ε_0 is the permittivity of free space. Because of the finite thickness, the BEM predictions are redshifted by 13% from the curves obtained by the electrostatic model. These shits are

corrected in Figs. C.1(a) and C.1(b) in order to compare the two methods.

Good agreement is observed in both geometries for frequencies bellow 80 THz. At higher frequencies, the contribution of $\Phi(\omega)$ to the overall radiative heat conductance is less than 4% due to the form of the Bose-Einstein distribution. The results from our theory were obtained two orders of magnitude faster than those from the BEM simulations (10,800 seconds computation time for the BEM simulation versus 31 seconds for the semi-analytical model using one 6-core Intel Xeon X5690 processor at 3.47 GHz).

Plasmonic Bandstructure

D.1 Electrostatic model for plasmonic band structure

In the case of a periodic array of graphene nanostructures with characteristic dimension L and separated by a distance $\Delta\boldsymbol{\gamma}$ the surface charge of each disk in the array, ρ^n, is related to the surface charge of a single disk, ρ, by $\rho^n = \rho e^{ik_p n\Delta\boldsymbol{\gamma}}$. Thus, from Eqn. (2.46) we derive the following non-dimensional eigenavalue equation

$$\left[\tilde{\mathbf{g}} - \eta\left(\tilde{\omega}_p\right)\sum_{n=-\infty}^{+\infty}\tilde{\mathbf{K}}^n e^{ink_p\Delta\boldsymbol{\gamma}}\right]\mathbf{c} = 0, \tag{D.1}$$

where

$$\tilde{g}_{ij} = \frac{1}{L^4}\langle\beta_i, g * \beta_j\rangle$$
$$\tilde{K}^n_{ij} = \frac{1}{L^3}\langle\beta_i, K^n * \beta_j\rangle,$$

with $K^n = K(\boldsymbol{\gamma}^0_{\parallel} + n\Delta\boldsymbol{\gamma}, \boldsymbol{\gamma}^{0\prime}_{\parallel})$, where $\boldsymbol{\gamma}^0_{\parallel}$ is a coordinate vector on the first unit cell and η is a non-dimensional eigenvalue defined as

$$\eta\left(\tilde{\omega}_p\right) = \frac{1}{\Omega_p^2} = \frac{\sigma\left(\tilde{\omega}_p\right)}{i\tilde{\omega}_p\varepsilon_0\varepsilon_h L}.$$

The maximum number of periods considered, N, must be long enough to reach convergence. We observed a convergence in the dispersion bands within $\pm 0.1\%$ error for $N = 25$.

Solution of Eqn. (D.1) for a mode expansion of j_N terms gives a set of j_N complex eigenfrequencies $\tilde{\omega}_{p_j}$ and eigenvectors $|c_j\rangle$ for each value of k_p. To classify the eigenfre-

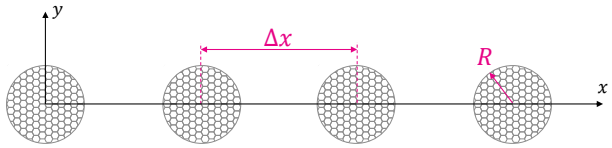

Figure D.1: Schematic diagram of an array of disks of radius R

quencies that correspond to a specific mode j, we determine the eigenvectors that satisfy the relation $\langle c_j^0 | c_i \rangle \neq 0$, where $|c_j^0\rangle$ are the eigenvectors of the eigenvalue equation for a single disk, *i.e.* $\left[\tilde{\mathbf{g}} - \eta(\tilde{\omega}_p^0)\tilde{\mathbf{K}}^0\right] \boldsymbol{c}^0 = 0$.

D.2 Modeling of radiation damping effects on the plasmonic band structure

We compare the dispersion relations obtained from the electrostatic model with those obtained from dipole-dipole interactions. The dipole-dipole model has proven to be accurate for predicting the dispersion bands of surface plasmons in metallic nanoparticle arrays[80, 90], provided that the distance between centers, Δx, and the characteristic dimension of the nanoparticle, D, satisfy the relation $\Delta x/D > 3/2$. Unlike the electrostatic approximation, the dipole-dipole model considers the effects of retardation and radiation reaction. As noted by Weber et al [90], these effects may play an important role in the shape of the dispersion bands.

In the dipole model, each disk is treated as a point dipole whose electric field, $\mathbf{E}_{\boldsymbol{p}}$, in vacuum is [24]:

$$\mathbf{E}_{\boldsymbol{p}} = \frac{1}{4\pi\varepsilon_0}\left[\left(1 + i\frac{\omega}{c_0}\gamma\right)\frac{3\left(\hat{\boldsymbol{\gamma}}\cdot\boldsymbol{p}\right)\hat{\boldsymbol{\gamma}} - \boldsymbol{p}}{\gamma^3} + \left(\frac{\omega}{c_0}\right)^2\frac{\boldsymbol{p} - \left(\hat{\boldsymbol{\gamma}}\cdot\boldsymbol{p}\right)\hat{\boldsymbol{\gamma}}}{\gamma}\right] e^{i\frac{\omega}{c_0}\gamma}, \tag{D.2}$$

where $\boldsymbol{p}$ is the electric dipole moment.

Considering the coordinate system in Fig. D.1, we conveniently separate the electric fields generated by transverse dipoles ($\hat{\boldsymbol{x}} \perp \boldsymbol{p}$) from those generated by longitudinal modes ($\hat{\boldsymbol{x}} \parallel \boldsymbol{p}$),

$$E_y^{\boldsymbol{p}}(\omega) = \frac{1}{\varepsilon_0} K_{\boldsymbol{p}_y}^{mn}(\omega)(\hat{\boldsymbol{y}} \cdot \boldsymbol{p}) \tag{D.3a}$$

$$E_x^{\boldsymbol{p}}(\omega) = \frac{1}{\varepsilon_0} \boldsymbol{p}_x{}^{mn}(\omega)(\hat{\boldsymbol{x}} \cdot \boldsymbol{p}), \tag{D.3b}$$

where

$$K_{\boldsymbol{p}_y}^{mn}(\omega) = 2\left(1 - ik_0 d_{mn}\right) \frac{e^{ik_0 d_{mn}}}{4\pi d_{mn}^3}$$

$$K_{\boldsymbol{p}_x}^{mn}(\omega) = \left[\left(k_0 d_{mn}\right)^2 + ik_0 d_{mn} - 1\right] \frac{e^{ik_0 d_{mn}}}{4\pi d_{mn}^3},$$

where $d_{mn} = |m-n|\Delta x$ and $k_0 = \omega/c_0$.

In order to consider periodic disk arrays with $\Delta x/D < 3/2$, we consider a combined model using Eqn. (A.13) for the disks with $d_{mn}/D < 3/2$, and Eqn. (D.2) for the rest of the disks in the array. As Eqn. (A.13) is given in the electrostatic limit, we need to extract the corresponding electric potential from Eqn. (D.2). Given that $k_0 R \ll 1$, we can consider the electric field emitted by a dipole as approximately uniform, therefore $E_{\boldsymbol{p}} = -\nabla\psi_{\boldsymbol{p}}$, and the electrostatic potential, $\psi^{\boldsymbol{p}}$, is then given by:

$$\psi_{\boldsymbol{p}} = -r\cos\phi E_x^{\boldsymbol{p}} - r\sin\phi E_y^{\boldsymbol{p}}.$$

Considering the orthonormal basis from Eqn. (A.4), the matrix elements of the dipole fields are given by

$$\langle \beta_{kl}, \psi_{\boldsymbol{p}} \rangle = -\frac{R^3}{4}\sqrt{2\pi}\ \delta_{k,0}\left[\left(\frac{\delta_{l,+1} + \delta_{l,-1}}{2}\right) E_x^{\boldsymbol{p}} + \left(\frac{\delta_{l,+1} - \delta_{l,-1}}{2i}\right) E_y^{\boldsymbol{p}}\right]. \tag{D.4}$$

Additionally, we express $\boldsymbol{p}$ in terms of the mode expansion as:

$$\begin{aligned}\boldsymbol{p} &= \hat{\boldsymbol{x}} \int_S d^2\boldsymbol{\gamma}_\parallel \; [x\rho(\boldsymbol{\gamma}_\parallel)] + \hat{\boldsymbol{y}} \int_S d^2\boldsymbol{\gamma}_\parallel \; [y\rho(\boldsymbol{\gamma}_\parallel)] \\ &= \sum_{k'l'} c_{k'l'} \frac{R^3}{4}\sqrt{2\pi}\; \delta_{k',0} \left[\left(\frac{\delta_{l',+1} + \delta_{l',-1}}{2} \right) \hat{\boldsymbol{x}} - \left(\frac{\delta_{l',+1} - \delta_{l',-1}}{2i} \right) \hat{\boldsymbol{y}} \right]. \end{aligned} \tag{D.5}$$

Combining Eqs. D.3, D.4 and D.5, we determine the dipole matrix elements, $\mathbf{X}_{\boldsymbol{p}}$, which can conveniently be expressed in a matrix form as $\mathbf{X}_{\boldsymbol{p}}^{mn}(\omega) = \frac{1}{\varepsilon_0}\tilde{\mathbf{K}}_{\boldsymbol{p}}^{mn}\boldsymbol{c}$, where

$$\tilde{\mathbf{K}}_{\boldsymbol{p}}^{mn}(\omega) = -\frac{R^6}{64}\left[\mathbf{I}^{\boldsymbol{p}_x} K_{\boldsymbol{p}_x}^{mn}(\omega) + \mathbf{I}^{\boldsymbol{p}_y} K_{\boldsymbol{p}_y}^{mn}(\omega) \right], \tag{D.6}$$

and

$$\mathbf{I}_{kl,k'l'}^{\boldsymbol{p}_x} = \begin{cases} 1 & \text{if } |l| = |l'| = 1 \text{ and } k = k' = 0 \\ 0 & \text{otherwise} \end{cases}$$

$$\mathbf{I}_{kl,k'l'}^{\boldsymbol{p}_y} = \begin{cases} l \cdot l' & \text{if } |l| = |l'| = 1 \text{ and } k = k' = 0 \\ 0 & \text{otherwise.} \end{cases}$$

Radiation reaction is included by considering the dipole radiation reaction field[54]

$$\mathbf{E}_{rad} = \frac{ik_0^3}{6\pi\varepsilon_0}\mathbf{p}, \tag{D.7}$$

Similarly to the derivation of Eqn. (D.6), we obtain the corresponding interaction matrix elements for the reaction field

$$\tilde{\mathbf{K}}_{rad}(\omega) = -\frac{R^6}{64}\left[\mathbf{I}^{\boldsymbol{p}_x} + \mathbf{I}^{\boldsymbol{p}_y}\right]\frac{ik_0^3}{6}, \tag{D.8}$$

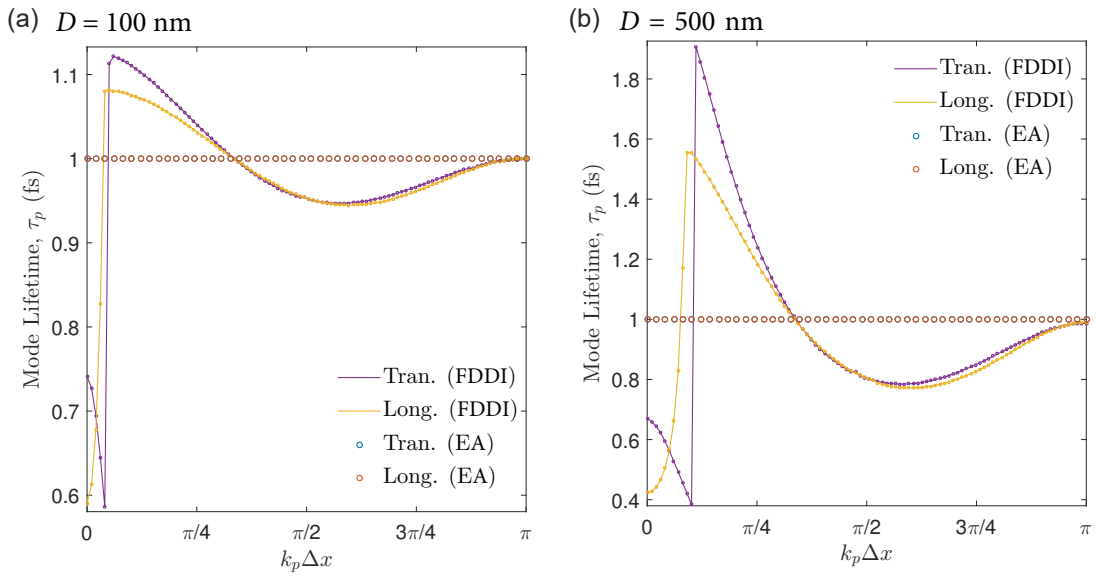

Figure D.2: Surface plasmons lifetime of the dipole modes, for an array of graphene nanodisks in vacumm with $\Delta x/D = 1.1$, $E_f = 1.0$ eV, and (a) $D = 100$ nm, (b) $D = 500$ nm. The results in continuous lines correspond to the calculations using the full dipole-dipole interaction model (FDDI) from Eqn. (D.9), and the open circles indicate the dispersion relation and decay length obtained by the electrostatic approximation model (EA) from Eqn. (D.1)

The dispersion bands are obtained from the complex eigenfrequencies $\tilde{\omega}_p$ that satisfy the equation:

$$\left| \tilde{\mathbf{g}} - \eta\left(\tilde{\omega}_p\right) \left[\frac{1}{R^3} \tilde{\mathbf{K}}_{rad}\left(\tilde{\omega}_p\right) + \sum_{\substack{n=-\infty \\ d_{0n}/D<3/2}}^{+\infty} \frac{1}{R^3} \tilde{\mathbf{K}}^n e^{ink_p\Delta x} + \sum_{\substack{n=-\infty \\ d_{0n}/D>3/2}}^{+\infty} \tilde{\mathbf{K}}_{\boldsymbol{p}}^{0n}\left(\tilde{\omega}_p\right) e^{ink_p\Delta x} \right] \right| = 0, \tag{D.9}$$

where the factor $1/R^3$ besides $\tilde{\mathbf{K}}_{rad}$ and $\tilde{\mathbf{K}}^n$ is added in order to maintain non-dimensionality.

Eqn. (D.9) is solved by the trust-region-dogleg algorithm using the eigenfrequencies obtained from the electrostatic eigenvalue problem (Eqn. (D.1)) as the initial iteration values.

Fig. D.2 shows the plasmonic lifetime of the lowest dipole mode for an array of graphene nanodisks in vacumm with $\Delta x/D = 1.1$, $E_f = 1.0$ eV, and disk diameters of 100 and

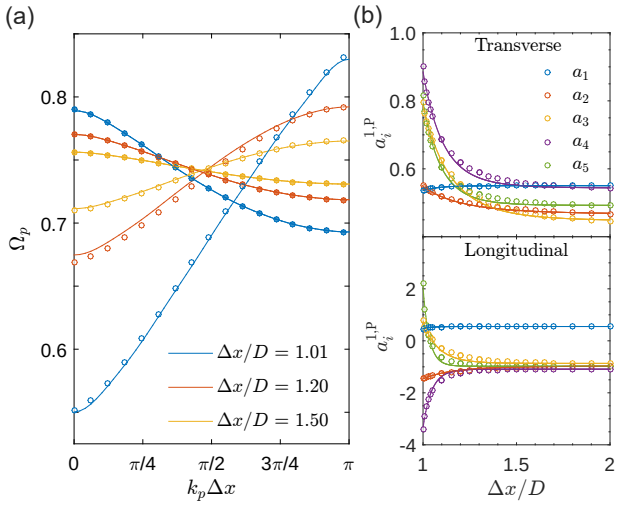

Figure D.3: (a) Non-dimensional dispersion relations of the fundamental dipole modes. The dispersion bands obtained from our electrostatic model are indicated by the circles, where open and filled correspond to longitudinal and transverse modes. The continuous lines are the bands obtained from fitting to Eqn. (D.10). (b) Fitting constants for the model of Eqn. (D.11).

500 nm. The results in continuous lines correspond to the calculations using the full dipole-dipole interaction model (FDDI) from Eqn. (D.9), and the open circles indicate the dispersion relation and decay length obtained by the electrostatic approximation model (EA) from Eqn. (D.1).

D.3 Fitting of non-dimensional dispersion

The dispersion bands of the non-dimensional model described in Section 5.3.3 can be fit to a model based on the electrostatic dipole-dipole interaction of the form [90]

$$\Omega_p^{l,P} = \left(\frac{D}{\Delta x}\right)^3 \sum_{i=0}^{\infty} a_i^{l,P} \frac{\cos(ik\Delta x)}{i^3}, \tag{D.10}$$

where $a_i^{l,P}$ are fitting parameters for the (l, P) band and P corresponds to the mode polarization (transverse or longitudinal). These fitting parameters depend on $\Delta x/D$.

We use Eqn. (D.10) to fit the non-dimensional dispersion of the fundamental dipole modes, given the importance of these modes for plasmonic applications. The fitted dispersion bands are plotted as lines in Fig. D.3(a) for $\Delta x/D = 1.01, 1.20$, and 1.50. A total of ten $a_i^{l,P}$ terms are considered, which gives an agreement of 1% with the exact results. The open (filled) circles correspond to the non-dimensional longitudinal (tranverse) dispersion obtained from the electrostatic model.

The $\Delta x/D$ dependence of the first five fitting parameters is plotted as circles in Fig. D.3(b). The fitting coefficients for both polarizations either increase or decrease monotonically until reaching a constant value at $\Delta x/D \approx 2$, which corresponds to the dipole-dipole interaction. We propose the following model for the $a_i^{1,P}$ parameters:

$$a_i^{1,P} = c_0 + c_1 \left(\frac{\Delta x}{D}\right)^{c_2}, \tag{D.11}$$

where c_0, c_1, and c_2 are fitting coefficients. Fitting of Eqn. (D.11) to the data show in Fig. D.3(b) gives the c_i paramters, which are provided in Table D.1. The fitted model from Eqn. (D.11) is plotted as continuous lines in Fig. D.3(b) and shows excellent agreement with the calculated data, with maximum errors of 0.1 and 1.5% for the transverse and longitudinal polarizations.

Table D.1: Fitting parameters for the a_i coefficients in Eqn. (D.11) for the $(k, l) = (0, \pm 1)$ modes

	Transverse			Longitudinal		
	c_0	c_1	c_2	c_0	c_1	c_2
a_0	0.5505	-12.0451	-0.0144	0.5506	-23.5592	-0.0850
a_1	0.4664	-4.8086	0.0814	-0.9702	-6.1394	-0.4907
a_2	0.4470	-6.8790	0.3379	-0.8697	-12.8291	1.6410
a_3	0.5438	-9.3168	0.3415	-1.0908	-21.9680	-2.2580
a_4	0.4924	-10.6530	0.3035	-0.9781	-30.7122	3.0451
a_5	0.6524	-11.1146	0.2509	-1.3185	-37.8654	-3.6455
a_6	0.5590	-10.7795	0.2330	-1.1120	-45.0985	4.2983
a_7	0.7767	-10.3024	0.2086	-1.5739	-48.8996	-4.7869
a_8	0.6367	-9.8255	0.2192	-1.2664	-53.9840	5.3225
a_9	0.9123	-9.4044	0.2105	-1.8515	-54.6836	-5.7031

Bibliography

[1] Harry A Atwater and Albert Polman. Plasmonics for improved photovoltaic devices. *Nat. Mater.*, 9(3):205–13, mar 2010. 1, 87

[2] Jon A Schuller, Edward S Barnard, Wenshan Cai, Young Chul Jun, Justin S White, and Mark L Brongersma. Plasmonics for extreme light concentration and manipulation. *Nat. Mater.*, 9(3):193–204, mar 2010. 1

[3] Mark L. Brongersma, Naomi J. Halas, and Peter Nordlander. Plasmon-induced hot carrier science and technology. *Nat. Nanotechnol.*, 10(1):25–34, jan 2015. xviii, 1, 2, 87, 88, 103

[4] Ekmel Ozbay. Plasmonics: merging photonics and electronics at nanoscale dimensions. *Science*, 311(5758):189–93, jan 2006. 1

[5] Dmitri K. Gramotnev and Sergey I. Bozhevolnyi. Plasmonics beyond the diffraction limit. *Nat. Photonics*, 4(2):83–91, jan 2010. 1

[6] L R Hirsch, R J Stafford, J A Bankson, S R Sershen, B Rivera, R E Price, J D Hazle, N J Halas, and J L West. Nanoshell-mediated near-infrared thermal therapy of tumors under magnetic resonance guidance. *Proc. Natl. Acad. Sci. U. S. A.*, 100(23):13549–54, nov 2003. 1

[7] Gururaj V Naik, Vladimir M Shalaev, and Alexandra Boltasseva. Alternative plasmonic materials: beyond gold and silver. *Adv. Mater.*, 25(24):3264–94, jun 2013. 2

[8] Zheyu Fang, Zheng Liu, Yumin Wang, Pulickel M. Ajayan, Peter Nordlander, and Naomi J. Halas. Graphene-antenna sandwich photodetector. *Nano Lett.*, 12(7):3808–

3813, 2012. 2, 5, 87, 102

[9] César Clavero. Plasmon-induced hot-electron generation at nanoparticle/metal-oxide interfaces for photovoltaic and photocatalytic devices. *Nat. Photonics*, 8(2):95–103, jan 2014. 2, 5, 87

[10] Stefan Alexander Maier. *Plasmonics: Fundamentals and Applications*. Springer, 2007. 2, 18, 19, 26, 27

[11] Boris Luk'yanchuk, Nikolay I Zheludev, Stefan A Maier, Naomi J Halas, Peter Nordlander, Harald Giessen, and Chong Tow Chong. The Fano resonance in plasmonic nanostructures and metamaterials. *Nat. Mater.*, 9(9):707–15, sep 2010. 2, 31

[12] T J Davis, D E Gómez, and K C Vernon. Simple model for the hybridization of surface plasmon resonances in metallic nanoparticles. *Nano Lett.*, 10(7):2618–25, jul 2010. 2, 31, 44

[13] David Solis, Britain Willingham, Scott L Nauert, Liane S Slaughter, Jana Olson, Pattanawit Swanglap, Aniruddha Paul, Wei-Shun Chang, and Stephan Link. Electromagnetic energy transport in nanoparticle chains via dark plasmon modes. *Nano Lett.*, 12(3):1349–53, mar 2012. 2, 31

[14] Frank H L Koppens, Darrick E Chang, and F Javier García de Abajo. Graphene Plasmonics: A Platform for Strong Light-Matter Interactions. *Nano Lett.*, 11(8):3370–7, aug 2011. xiv, 3, 29, 41, 64, 66, 69, 79

[15] F. Javier García de Abajo. Graphene Plasmonics: Challenges and Opportunities. *ACS Photonics*, 1(3):135–152, mar 2014. 3, 20, 21, 28, 37, 38, 58, 84, 102

[16] Jessica R. Piper and Shanhui Fan. Total Absorption in a Graphene Monolayer in the Optical Regime by Critical Coupling with a Photonic Crystal Guided Resonance. *ACS Photonics*, 1(4):347–353, apr 2014. 3, 41

[17] Hugen Yan, Xuesong Li, Bhupesh Chandra, George Tulevski, Yanqing Wu, Marcus Freitag, Wenjuan Zhu, Phaedon Avouris, and Fengnian Xia. Tunable infrared plasmonic devices using graphene/insulator stacks. *Nat. Nanotechnol.*, 7(5):330–4, may 2012. 3, 41, 42

[18] E. Hwang and S. Das Sarma. Plasmon modes of spatially separated double-layer graphene. *Phys. Rev. B*, 80(20):205405, nov 2009. 3, 42, 49

[19] Karl Joulain, Jean Philippe Mulet, François Marquier, Rémi Carminati, and Jean Jacques Greffet. Surface electromagnetic waves thermally excited: Radiative heat transfer, coherence properties and Casimir forces revisited in the near field. *Surf. Sci. Rep.*, 57(3-4):59–112, may 2005. 4, 16, 17, 57, 69, 103

[20] Ognjen Ilic, Marinko Jablan, John D. Joannopoulos, Ivan Celanovic, Hrvoje Buljan, and Marin Soljačić. Near-field thermal radiation transfer controlled by plasmons in graphene. *Phys. Rev. B*, 85(15):155422, apr 2012. 4, 57, 63, 64, 69

[21] Riccardo Messina and Philippe Ben-Abdallah. Graphene-based photovoltaic cells for near-field thermal energy conversion. *Sci. Rep.*, 3:1383, jan 2013. 4, 57, 69

[22] Philippe Ben-Abdallah and Svend-Age Biehs. Towards boolean operations with thermal photons. *Phys. Rev. A*, 241401(24):1–5, dec 2016. 4

[23] Shaunak Mukherjee, Florian Libisch, Nicolas Large, Oara Neumann, Lisa V Brown, Jin Cheng, J Britt Lassiter, Emily A Carter, Peter Nordlander, and Naomi J Halas. Hot electrons do the impossible: plasmon-induced dissociation of H2 on Au. *Nano Lett.*, 13(1):240–7, jan 2013. 5, 87

[24] John David Jackson. *Classical Electrodynamics*. John Wiley & Sons, New York, 3th edition, 1998. 6, 30, 39, 105, 107, 109, 118

[25] Lukas Novotny and Bert Hecht. *Principles of Nano-Optics*. Cambridge University

Press, 1st edition, 2006. xiii, 10, 11, 14, 15, 17

[26] John Joannopoulos, Steven Johnson, Joshua Winn, and Robert Meade. *Photonic Crystals: Molding the Flow of Light.* Princeton University Press, 2nd edition, 2008. 11

[27] Fluorescence Microscopy. Molecular Expressions Microscopy Primer : Specialized Microscopy Techniques, 2005. xiii, 12

[28] David J. Griffiths. *Introduction to Electrodynamics.* Addison Wesley, 3th edition, 1999. 13

[29] David Chandler. *Introduction to Modern Statistical Mechanics.* Oxford University Press, 1987. 16

[30] Jean-Philippe Mulet, Karl Joulain, Rémi Carminati, and Jean-Jacques Greffet. Enhanced Radiative Heat Transfer At Nanometric Distances. *Microscale Thermophys. Eng.*, 6(3):209–222, 2002. 17, 64

[31] Arvind Narayanaswamy and Gang Chen. Thermal near-field radiative transfer between two spheres. *Phys. Rev. B*, 77(7):075125, feb 2008. 17, 57, 63

[32] Alejandro W. Rodriguez, M. T. Homer Reid, and Steven G. Johnson. Fluctuating-surface-current formulation of radiative heat transfer for arbitrary geometries. *Phys. Rev. B*, 86(22):220302, dec 2012. 17

[33] M. T. Homer Reid. SCUFF-EM: Free, open-source software for boundary-element analysis of problems in computational physics and engineering, 2014. xv, 17, 46, 47, 49, 58, 115

[34] Marco Bernardi, Jamal Mustafa, Jeffrey B. Neaton, and Steven G. Louie. Theory and computation of hot carriers generated by surface plasmon polaritons in noble metals. *Nat. Commun.*, 6:7044, jun 2015. xiii, 18

[35] Edward D. Palik and G Ghosh. *Handbook of optical constants of solids*. Academic Press, 1st edition, 1998. 19

[36] A K Geim and K S Novoselov. The rise of graphene. *Nat. Mater.*, 6(3):183–191, 2007. xiv, 19, 21

[37] A. H. Castro Neto, N. M. R. Peres, K. S. Novoselov, and A. K. Geim. The electronic properties of graphene. *Rev. Mod. Phys.*, 81(1):109–162, jan 2009. xiv, 20

[38] F. Bonaccorso, Z. Sun, T. Hasan, and A. C. Ferrari. Graphene photonics and optoelectronics. *Nat. Photonics*, 4(9):611–622, aug 2010. 20

[39] L A Falkovsky. Optical properties of graphene. *J. Phys. Conf. Ser.*, 129(1):012004, oct 2008. 20, 115

[40] J. A. Dionne, L. A. Sweatlock, H. A. Atwater, and A. Polman. Planar metal plasmon waveguides: frequency-dependent dispersion, propagation, localization, and loss beyond the free electron model, aug 2005. xiv, 25

[41] Craig F. Bohren and Donald R. Huffman. *Absorption and Scattering of Light by Small Particles*. Wiley-VCH, 1998. 29, 43, 59, 70

[42] Feng Ouyang and Michael Isaacson. Surface plasmon excitation of objects with arbitrary shape and dielectric constant. *Philos. Mag. Part B*, 60(4):481–492, oct 1989. 31, 35

[43] F. García de Abajo and J. Aizpurua. Numerical simulation of electron energy loss near inhomogeneous dielectrics. *Phys. Rev. B*, 56(24):15873–15884, dec 1997. 31

[44] I. D. Mayergoyz. *Plasmon resonances in nanoparticles*. World Scientific, 2013. 34, 105

[45] Alexander Fetter. Magnetoplasmons in a two-dimensional electron fluid: Disk geometry. *Phys. Rev. B*, 33(8):5221–5227, apr 1986. 38, 42, 47, 58, 59, 106, 107

[46] Long Ju, Baisong Geng, Jason Horng, Caglar Girit, Michael Martin, Zhao Hao, Hans a Bechtel, Xiaogan Liang, Alex Zettl, Y Ron Shen, and Feng Wang. Graphene plasmonics for tunable terahertz metamaterials. *Nat. Nanotechnol.*, 6(10):630–4, oct 2011. 41, 42

[47] Richard Leavitt and J. Little. Absorption and emission of radiation by plasmons in two-dimensional electron-gas disks. *Phys. Rev. B*, 34(4):2450–2457, aug 1986. 41

[48] S. Allen, H. Störmer, and J. Hwang. Dimensional resonance of the two-dimensional electron gas in selectively doped GaAs/AlGaAs heterostructures. *Phys. Rev. B*, 28(8):4875–4877, oct 1983. 41

[49] Hugen Yan, Fengnian Xia, Zhiqiang Li, and Phaedon Avouris. Plasmonics of coupled graphene micro-structures. *New J. Phys.*, 14(12):125001, dec 2012. 42

[50] John Wang, Ping Liu, Jocelyn Hicks-Garner, Elena Sherman, Souren Soukiazian, Mark Verbrugge, Harshad Tataria, James Musser, and Peter Finamore. Cycle-life model for graphite-LiFePO4 cells. *J. Power Sources*, 196(8):3942–3948, apr 2011. 42, 58

[51] Anshuman Kumar, Kin Hung Fung, M T Homer Reid, and Nicholas X Fang. Photon emission rate engineering using graphene nanodisc cavities. *Opt. Express*, 22(6):6400–15, mar 2014. 42, 44, 58, 61

[52] Weihua Wang, S. Peter Apell, and Jari M. Kinaret. Edge magnetoplasmons and the optical excitations in graphene disks. *Phys. Rev. B*, 86(12):125450, sep 2012. 42, 58

[53] Weihua Wang. Plasmons and optical excitations in graphene rings. *J. Phys. Condens. Matter*, 24(40):402202, oct 2012. 42

[54] T. Davis, K. Vernon, and D. Gómez. Designing plasmonic systems using optical coupling between nanoparticles. *Phys. Rev. B*, 79(15):155423, apr 2009. 42, 47, 60,

74, 76, 120

[55] P. Nordlander, C. Oubre, E. Prodan, K. Li, and M. I. Stockman. Plasmon Hybridization in Nanoparticle Dimers. *Nano Lett.*, 4(5):899–903, may 2004. 44, 94

[56] E Prodan, C Radloff, N J Halas, and P Nordlander. A Hybridization Model for the Plasmon Response of Complex Nanostructures. *Science (80-.).*, 302(5644):419–22, oct 2003. 44

[57] M. T. Homer Reid and Steven G. Johnson. Efficient Computation of Power, Force, and Torque in BEM Scattering Calculations. jul 2013. 49, 111, 112

[58] Bai Song, Yashar Ganjeh, Seid Sadat, Dakotah Thompson, Anthony Fiorino, Víctor Fernández-Hurtado, Johannes Feist, Francisco J Garcia-Vidal, Juan Carlos Cuevas, Pramod Reddy, and Edgar Meyhofer. Enhancement of near-field radiative heat transfer using polar dielectric thin films. *Nat. Nanotechnol.*, 10(3):253–8, mar 2015. 57

[59] Sheng Shen, Arvind Narayanaswamy, and Gang Chen. Surface Phonon Polaritons Mediated Energy Transfer between Nanoscale Gaps. *Nano Lett.*, 9(8):2909–2913, 2009. 57

[60] A. Volokitin and B. Persson. Radiative heat transfer between nanostructures. *Phys. Rev. B*, 63(20):205404, apr 2001. 57, 62, 64

[61] Gilberto Domingues, Sebastian Volz, Karl Joulain, and Jean Jacques Greffet. Heat transfer between two nanoparticles through near field interaction. *Phys. Rev. Lett.*, 94(8):085901, mar 2005. 57, 62, 63

[62] Mathieu Francoeur, Soumyadipta Basu, and Spencer J Petersen. Electric and magnetic surface polariton mediated near-field radiative heat transfer between metamaterials made of silicon carbide particles. *Opt. Express*, 19(20):18774–88, sep 2011. 57

[63] Baoan Liu and Sheng Shen. Broadband near-field radiative thermal emitter/absorber based on hyperbolic metamaterials: Direct numerical simulation by the Wiener chaos expansion method. *Phys. Rev. B*, 87(11):115403, mar 2013. 57

[64] Owen D. Miller, Steven G. Johnson, and Alejandro W. Rodriguez. Effectiveness of Thin Films in Lieu of Hyperbolic Metamaterials in the Near Field. *Phys. Rev. Lett.*, 112(15):157402, apr 2014. 57

[65] Linxiao Zhu, Clayton R. Otey, and Shanhui Fan. Ultrahigh-contrast and large-bandwidth thermal rectification in near-field electromagnetic thermal transfer between nanoparticles. *Phys. Rev. B*, 88(18):184301, nov 2013. 57, 85

[66] A. I. Volokitin and B. N. J. Persson. Near-field radiative heat transfer between closely spaced graphene and amorphous SiO 2. *Phys. Rev. B*, 83(24):241407, jun 2011. 57, 69

[67] P. Ben-Abdallah, A. Belarouci, L. Frechette, and S.-A. Biehs. Heat flux splitter for near-field thermal radiation. *Appl. Phys. Lett.*, 107(5):053109, aug 2015. 57, 58, 70, 85

[68] Baoan Liu, Yongmin Liu, and Sheng Shen. Thermal plasmonic interconnects in graphene. *Phys. Rev. B*, 90(19):195411, nov 2014. 57

[69] Renwen Yu, Alejandro Manjavacas, and F. Javier García de Abajo. Ultrafast radiative heat transfer. *Nat. Commun.*, 8(1):2, 2017. 57, 69, 101

[70] Tony Low and Phaedon Avouris. Graphene plasmonics for terahertz to mid-infrared applications. *ACS Nano*, 8(2):1086–101, feb 2014. 57, 69

[71] A. N. Grigorenko, M. Polini, and K. S. Novoselov. Graphene plasmonics. *Nat. Photonics*, 6(11):749–758, nov 2012. 58, 69

[72] Saeedeh Barzegar-Parizi, Behzad Rejaei, and Amin Khavasi. Analytical Circuit

Model for Periodic Arrays of Graphene Disks. *IEEE J. Quantum Electron.*, 51(9):1–7, sep 2015. 58, 70

[73] G. Agarwal. Quantum electrodynamics in the presence of dielectrics and conductors. I. Electromagnetic-field response functions and black-body fluctuations in finite geometries. *Phys. Rev. A*, 11(1):230–242, jan 1975. 59, 114

[74] Francisco Ramirez, Baoan Liu, and Sheng Shen. Extreme blueshift of surface plasmon resonance frequency in graphene nanodisk stacks. *J. Quant. Spectrosc. Radiat. Transf.*, 158:27–35, jun 2015. 60, 61, 63

[75] Adriennne S Lavine, David P DeWitt, Theodore L Bergman, and Frank P Incropera. *Fundamentals of Heat and Mass Transfer*. John Wiley and Sons, 2011. 62, 65, 84, 85

[76] Johan Christensen, Alejandro Manjavacas, Sukosin Thongrattanasiri, Frank H L Koppens, and F Javier García de Abajo. Graphene plasmon waveguiding and hybridization in individual and paired nanoribbons. *ACS Nano*, 6(1):431–40, jan 2012. 66, 69, 70, 79

[77] Alexander a Balandin. Thermal properties of graphene and nanostructured carbon materials. *Nat. Mater.*, 10(8):569–81, aug 2011. 66, 79

[78] Simon Lu and Alan J. H. McGaughey. Thermal conductance of graphene/hexagonal boron nitride heterostructures. *J. Appl. Phys.*, 121(11):115103, mar 2017. 66, 79

[79] Philippe Ben-Abdallah, Karl Joulain, Jérémie Drevillon, and Clément Le Goff. Heat transport through plasmonic interactions in closely spaced metallic nanoparticle chains. *Phys. Rev. B*, 77(7):075417, feb 2008. 69, 80, 81

[80] Jose Ordonez-Miranda, Laurent Tranchant, Sergei Gluchko, and Sebastian Volz. Energy transport of surface phonon polaritons propagating along a chain of spheroidal

nanoparticles. *Phys. Rev. B*, 92(11):115409, sep 2015. 69, 81, 118

[81] Philippe Ben-Abdallah, Riccardo Messina, Svend Age Biehs, Maria Tschikin, Karl Joulain, and Carsten Henkel. Heat superdiffusion in plasmonic nanostructure networks. *Phys. Rev. Lett.*, 111(17):174301, oct 2013. 69

[82] E. J. Tervo, O. S. Adewuyi, J. S. Hammonds, and B. A. Cola. High thermal conductivity in polaritonic SiO 2 nanoparticle beds. *Mater. Horiz.*, 3(5):434–441, 2016. 69

[83] Francisco Ramirez, Sheng Shen, and Alan J. H. McGaughey. Near-Field Radiative Heat Transfer in Graphene Plasmonic Nanodisk Dimers. *Phys. Rev. B (to be Submitt.*, 2017. 69, 70, 71

[84] Karl Joulain, Rémi Carminati, Jean-Philippe Mulet, and Jean-Jacques Greffet. Definition and measurement of the local density of electromagnetic states close to an interface. *Phys. Rev. B*, 68(24):245405, dec 2003. 69

[85] A. Yu. Nikitin, F. Guinea, F. J. García-Vidal, and L. Martín-Moreno. Edge and waveguide terahertz surface plasmon modes in graphene microribbons. *Phys. Rev. B*, 84(16):161407, oct 2011. 69

[86] Daria A. Smirnova, Roman E. Noskov, Lev A. Smirnov, and Yuri S. Kivshar. Dissipative plasmon solitons in graphene nanodisk arrays. *Phys. Rev. B*, 91(7):075409, feb 2015. 70

[87] Mark Fox. *Optical Properties of Solids*. 2nd edition, 2010. 71

[88] Sukosin Thongrattanasiri, Frank H. L. Koppens, and F. Javier García de Abajo. Complete Optical Absorption in Periodically Patterned Graphene. *Phys. Rev. Lett.*, 108(4):047401, jan 2012. 73

[89] F. J. García de Abajo. Colloquium: Light scattering by particle and hole arrays.

Rev. Mod. Phys., 79(4):1267–1290, oct 2007. 73

[90] W. H. Weber and G. W. Ford. Propagation of optical excitations by dipolar interactions in metal nanoparticle chains. *Phys. Rev. B - Condens. Matter Mater. Phys.*, 70(12):125429, sep 2004. 74, 118, 122

[91] D. S. Citrin. Coherent excitation transport in metal-nanoparticle chains. *Nano Lett.*, 4(9):1561–1565, 2004. 74

[92] Charles. Kittel and Paul McEuen. *Introduction to solid state physics*, volume 8. John Wiley & Sons, New York, 8th edition, 2005. 79, 84

[93] Eric Pop, Vikas Varshney, and Ak Roy. Thermal properties of graphene: Fundamentals and applications. *Mrs Bull.*, 1273(December):1–28, dec 2012. 80

[94] Philippe Ben-Abdallah and Svend-Age Biehs. Thermotronics: Towards Nanocircuits to Manage Radiative Heat Flux. *Zeitschrift für Naturforsch. A*, 0(0), jan 2016. 84

[95] H. S. Carslaw and J. C. Jaeger. *Conduction of Heat in Solids*. Clarendon Press, 1959. 85

[96] Soumyadipta Basu and Mathieu Francoeur. Near-field radiative heat transfer between metamaterial thin films. *Opt. Lett.*, 39(5):1266–9, mar 2014. 85

[97] Philippe Ben-Abdallah and Svend-Age Biehs. Near-Field Thermal Transistor. *Phys. Rev. Lett.*, 112(4):044301, jan 2014. 85

[98] Jeffrey N. Anker, W. Paige Hall, Olga Lyandres, Nilam C. Shah, Jing Zhao, and Richard P. Van Duyne. Biosensing with plasmonic nanosensors. *Nat. Mater.*, 7(6):442–453, jun 2008. 87

[99] Guillaume Baffou and Romain Quidant. Thermo-plasmonics: using metallic nanostructures as nano-sources of heat. *Laser Photon. Rev.*, 7(2):171–187, mar 2013. 87

[100] Lisa V. Brown, Heidar Sobhani, J. Britt Lassiter, Peter Nordlander, and Naomi J.

Halas. Heterodimers: Plasmonic properties of mismatched nanoparticle pairs. In *ACS Nano*, volume 4, pages 819–832. American Chemical Society, feb 2010. 88

[101] Lucas V. Besteiro and Alexander O. Govorov. Amplified Generation of Hot Electrons and Quantum Surface Effects in Nanoparticle Dimers with Plasmonic Hot Spots. *J. Phys. Chem. C*, 120(34):19329–19339, sep 2016. 88, 92

[102] Alejandro Manjavacas, Jun G Liu, Vikram Kulkarni, and Peter Nordlander. Plasmon-induced hot carriers in metallic nanoparticles. *ACS Nano*, 8(8):7630–8, aug 2014. 89, 92, 93

[103] J. R. M. Saavedra, Ana Asenjo-Garcia, and F. Javier García de Abajo. Hot-Electron Dynamics and Thermalization in Small Metallic Nanoparticles. *ACS Photonics*, 3(9):1637 – 1646, sep 2016. 89

[104] Alexander O. Govorov, Hui Zhang, and Yurii K. Gun'ko. Theory of Photoinjection of Hot Plasmonic Carriers from Metal Nanostructures into Semiconductors and Surface Molecules. *J. Phys. Chem. C*, 117(32):16616–16631, aug 2013. 92

[105] K. T. Regner, S. Majumdar, and J. A. Malen. Instrumentation of broadband frequency domain thermoreflectance for measuring thermal conductivity accumulation functions. *Rev. Sci. Instrum.*, 84(6):064901, jun 2013. 101

[106] Jeremy A. Johnson, Alexei A. Maznev, Mayank T. Bulsara, Eugene A. Fitzgerald, T. C. Harman, S. Calawa, C. J. Vinels, G. Turner, and Keith A. Nelson. Phase-controlled, heterodyne laser-induced transient grating measurements of thermal transport properties in opaque material. *J. Appl. Phys.*, 111(2):023503, jan 2012. 101

[107] Andrea Lovera, Benjamin Gallinet, Peter Nordlander, and Olivier J F Martin. Mechanisms of Fano resonances in coupled plasmonic systems. *ACS Nano*, 7(5):4527–36,

may 2013. 102

[108] Nils-Peter Harder and Peter W rfel. Theoretical limits of thermophotovoltaic solar energy conversion. *Semicond. Sci. Technol.*, 18(5):S151–S157, may 2003. 103

[109] David M. Bierman, Andrej Lenert, Walker R. Chan, Bikram Bhatia, Ivan Celanović, Marin Soljačić, and Evelyn N. Wang. Enhanced photovoltaic energy conversion using thermally based spectral shaping. *Nat. Energy*, 1(6):16068, may 2016. 103

[110] Ognjen Ilic, Marinko Jablan, and JD Joannopoulos. Overcoming the black body limit in plasmonic and graphene near-field thermophotovoltaic systems. *Opt. Express*, 20(May):6621–6633, 2012. 103

[111] Raphael St-gelais, Gaurang Ravindra Bhatt, Linxiao Zhu, Shanhui Fan, and Michal Lipson. Hot Carrier- Based Near-Field Thermophotovoltaic Energy Conversion. *ACS Nano*, 11(3):Just Accepted, mar 2017. 103, 104

[112] I. S. Gradshteyn and I. M. Ryzhik. *Table of Integrals, Series, and Products*. Academic Press, New York, 7th edition, 2007. 106

[113] Leung Tsang, Jin Au Kong, Kung-Hau Ding, and Chi On Ao. *Scattering of Electromagnetic Waves: Theories and Applications*. Wiley-Interscience, 2000. 108